

AGARD-AG-288

AD-A153 233

AGARD

ADVISORY GROUP FOR AEROSPACE RESEARCH & DEVELOPMENT

7 RUE ANCELLE 92200 NEUILLY SUR SEINE FRANCE

AGARDograph No.288

Low Reynolds Number Vehicles

This document has been approved
for public release and sale; its
distribution is unlimited.

DTIC
ELECTE
MAY 6 1985
A X

NORTH ATLANTIC TREATY ORGANIZATION



DISTRIBUTION AND AVAILABILITY
ON BACK COVER

85 5 03 015

DTIC FILE COPY

NORTH ATLANTIC TREATY ORGANIZATION
ADVISORY GROUP FOR AEROSPACE RESEARCH AND DEVELOPMENT
(ORGANISATION DU TRAITE DE L'ATLANTIQUE NORD)

AGARDograph No.288
LOW REYNOLDS NUMBER VEHICLES

by

Thomas J. Mueller
University of Notre Dame
Notre Dame, Indiana 46556
USA

Edited by

Eli Reshotko
Case Western Reserve University
Cleveland, Ohio 44106
USA

THE MISSION OF AGARD

The mission of AGARD is to bring together the leading personalities of the NATO nations in the fields of science and technology relating to aerospace for the following purposes:

- Exchanging of scientific and technical information;
- Continuously stimulating advances in the aerospace sciences relevant to strengthening the common defence posture;
- Improving the co-operation among member nations in aerospace research and development;
- Providing scientific and technical advice and assistance to the North Atlantic Military Committee in the field of aerospace research and development;
- Rendering scientific and technical assistance, as requested, to other NATO bodies and to member nations in connection with research and development problems in the aerospace field;
- Providing assistance to member nations for the purpose of increasing their scientific and technical potential;
- Recommending effective ways for the member nations to use their research and development capabilities for the common benefit of the NATO community.

The highest authority within AGARD is the National Delegates Board consisting of officially appointed senior representatives from each member nation. The mission of AGARD is carried out through the Panels which are composed of experts appointed by the National Delegates, the Consultant and Exchange Programme and the Aerospace Applications Studies Programme. The results of AGARD work are reported to the member nations and the NATO Authorities through the AGARD series of publications of which this is one.

Participation in AGARD activities is by invitation only and is normally limited to citizens of the NATO nations.

The content of this publication has been reproduced
directly from material supplied by AGARD or the author.

Published February 1985

Copyright © AGARD 1985
All Rights Reserved

ISBN 92-835-1486-6



Printed by Specialised Printing Services Limited
40 Chigwell Lane, Loughton, Essex IG10 3JZ

ACKNOWLEDGEMENTS

It is a pleasure to thank D.M.Somers (NASA Langley Research Center), J.D.Anderson, Jr and A.P.Kothari (University of Maryland), J.H.McMasters (Boeing Commercial Aircraft Company), J.W.Youngblood (NASA Langley Research Center), D.W.Hall and R.W.Parks (Lockheed Missile and Space Company), R.Foch (Naval Research Laboratory) and R.C.Eklund (Locus, Inc.) for generously providing details of their research in this area. My sincere thanks go to my colleagues at the University of Notre Dame, R.C.Nelson and S.M.Batill, and my graduate students M.Brendel, G.S.Schmidt, A.F.Huber II, W.G.Bastedo and M.M.O'Meara for sharing their research in this field as well as for their helpful comments during the writing of this book. Finally I would like to thank the members of the Fluid Dynamics Panel, especially E.Reshotko, for suggesting this topic and for their patience in waiting for its completion.

CONTENTS

	Page
ACKNOWLEDGEMENTS	iii
SUMMARY	1
1. INTRODUCTION	1
1.1 Applications of Interest	1
1.2 Design Aims	2
1.3 Flow Problems	2
1.4 Scope of Review	3
2. BOUNDARY LAYER BEHAVIOR	3
2.1 Historical Background	4
2.2 Laminar Flow	4
2.3 Separation Bubble and Transition	5
2.4 Low Reynolds Number Turbulent Flow	6
3. DESIGN AND MODELING PROCEDURES	6
3.1 The Eppler Airfoil Design and Analysis Program	7
3.1.1 Theory	7
3.1.2 Examples Using Eppler's Method	8
3.1.3 Remarks	8
3.2 Viscous-Inviscid Interaction Methods	8
3.3 Numerical Modeling	10
3.3.1 Physical Problem and Governing Equations	10
3.3.2 Numerical Technique	11
3.3.3 Typical Results	12
4. EXPERIMENTAL EVALUATION OF DESIGN	12
4.1 Wind Tunnel Experiments	12
4.1.1 Influence of Experimental Technique and Procedure	12
4.1.1.1 Wind Tunnel and Force Balance	13
4.1.1.2 Pressure Measurement	14
4.1.1.3 Discussion of Results	14
4.1.2 Influence of Free Stream Disturbances	15
4.1.2.1 Experimental Apparatus and Procedure	15
4.1.2.2 Disturbance Environment — No Airfoil Present	16
4.1.2.3 Airfoil Performance	18
4.1.2.4 Remarks	20
4.1.3 The Influence of Surface Roughness	20
4.1.4 Finite Wing Experiments	21
4.2 Flight Research Experiments	22
5. PRACTICAL APPLICATIONS	22
5.1 Remotely Piloted Vehicles and Sailplanes	23
5.2 Wind Turbines	23
6. CONCLUDING REMARKS	24
7. RECOMMENDATIONS FOR FUTURE RESEARCH	24
REFERENCES	25
FIGURES	32

LOW REYNOLDS NUMBER VEHICLES

by

Thomas J. Mueller*

University of Notre Dame, Notre Dame, Indiana 46556, U.S.A.

SUMMARY

Recent interest in a wide variety of low Reynolds number configurations has focused attention on the design and evaluation of efficient airfoil sections at chord Reynolds numbers from about 100,000 to about 1,000,000. These configurations include remotely piloted vehicles (RPV's) at high altitudes, sailplanes, ultra-light man-carrying/man-powered aircraft, mini-RPV's at low altitudes and wind turbines/propellers. A study is presented of the present status and future possibility of airfoil design and evaluation at subcritical speeds to meet the needs for these applications.

Although the design and evaluation techniques for airfoil sections above chord Reynolds numbers of 500,000 is reasonably well developed, serious problems related to boundary layer separations and transition have been encountered below $Re_c = 500,000$. Presently available design and analysis methods need to improve their criteria for laminar separation, transition, and turbulent separation. Improved mathematical models of these complex phenomena require additional, very careful experimental studies. Because of the sensitivity of the low Reynolds number airfoil boundary layer to free stream and surface-generated disturbances, definitive experiments are very difficult. Also the physical quantities measured (i.e., pressure difference and drag forces etc.) are very small and the accuracy of such measurements depends on the method used. The results from numerous experimental studies are presented to illustrate the type of difficulties encountered.

1. INTRODUCTION

Recently attention has turned toward low Reynolds number aerodynamics at subcritical speeds in an effort to obtain better performance for both military and civilian applications. These applications include remotely piloted vehicles (RPVs) at high altitudes, sailplanes, ultra-light man-carrying/man-powered aircraft, mini-RPVs at low altitude, and wind turbines.

Since the airfoil section forms the basic element in the design of a wing, propeller or conventional wind turbine, it has been the focus of most of the attention in this area¹⁻³. The performance of an airfoil section is critically dependent upon the character of the viscous boundary layer (i.e., laminar, transitional or turbulent). The Reynolds number, which is the ratio of inertial to viscous forces or characteristic length times velocity divided by kinematic viscosity, is usually used to scale vehicles. The characteristic length in this case is the airfoil chord. Other things equal, the character of the boundary layer has been found to be dependent on the magnitude of the Reynolds number. A broad perspective on the range of chord Reynolds numbers versus flight velocity and Mach number for a variety of natural and man-made flying objects can be obtained from Figure 1.

Although the designer of a large transport aircraft might consider a chord Reynolds number of 10^6 to be low, the designer of a high altitude RPV or wind turbine would take the opposite point of view. Almost all natural flying-objects fall in the Reynolds number range below 10^6 . Furthermore it should be remembered that most large high speed vehicles or at least some components of these vehicles (i.e., control surfaces and lift or drag augmentation devices) operate at much lower Reynolds numbers during take-off and landing. It should also be mentioned that much of the wind tunnel testing by large aircraft manufacturers is done at relatively low Reynolds numbers. At high altitudes aircraft gas turbine engine fan, compressor, and turbine blades with their small chords encounter Reynolds numbers considerably below 10^6 . Even the Space Shuttle encounters Reynolds numbers as low as 10^4 at $M = 27$ during reentry. It is clear that some definition of what is meant by low Reynolds number aerodynamics is needed. In the present context, low Reynolds numbers are considered to be those below about 10^6 since the effects of laminar separation and transition to turbulence in the airfoil boundary layer have a great and sometimes unpredictable influence on overall vehicle performance. The applications included under the title low Reynolds Number Vehicles require efficient airfoil sections in the chord Reynolds number range from about 10^5 to 10^6 as indicated in Figure 1.

1.1 Applications of Interest

A large number of applications have been proposed for high altitude RPVs, often referred to as high altitude aircraft platforms (HAAPs)⁵⁻¹⁴. Graves¹¹ summarized these proposed HAAP applications as follows: 1) Military - Communications Relay, Ballistic Missile Early Warning, Aircraft Tracking, Weather Monitoring, Ocean Surveillance, Battlefield Tactical Intelligence, and Nuclear Explosion Cloud Sampling, 2) Scientific - Astronomical Observations, Atmospheric Research, and Oceanographic Research, 3) Civil - 200 Mile Fishery Enforcement, Border Patrol Surveillance, Water Pollution Monitoring, Resource Management, HIF TV Broadcasts, National TV Distribution, Ice Surveying/Mapping of Waterways, and Emergency Response Communications. Since most of these applications would require that the vehicle fly continuously without refueling, the feasibility of using solar-voltaic, microwave and nuclear propulsion systems have been explored⁵⁻¹⁷.

The modern sailplane represents man's greatest triumph in aerodynamic performance and efficiency. Although soaring began in the late 1800's, the vast majority of improvements in this technology have been made recently in Europe, especially in Germany¹⁸⁻¹⁹. Sailplane developments have provided the stimulus for the practical application of laminar flow aerodynamics.

* Department of Aerospace and Mechanical Engineering

The recent ultra-light man-carrying/man-powered aircraft, developed largely in the United States, owe their success mostly to lightweight materials and, to a lesser degree, to aerodynamics. The addition of a small gasoline engine to a hang glider to produce an ultra-light aircraft was accomplished as recently as the early 1970's²⁰. The first entry was the so-called "back pack" engine. A 10 hp. Go-Kart engine driving a caged propeller was simply strapped to the back of the flyer of the Rogallo "kite." Due to its weight, discomfort and poor performance, it was never really accepted. Soon after the "back pack" Rogallo concept, super-lightweight versions of more conventional airplane-like hang gliders with control systems were developed. In 1975 a go-kart engine was mounted to a biplane hang glider of this type by Moody²⁰ and the ultra-light airplane was born. In pursuit of the "Kremer Prize", MacCready and his associates designed and successfully flew one of the earliest man-powered (i.e., muscle-driven) airplane. On August 23, 1977, the Gossamer Condor flew the figure-eight Kremer course in 7 1/2 minutes. The bicycle-type propulsion mechanism driven by B. Allen produced about 0.4 hp at cruise. This historic man-powered flight was followed by the two hour and 49 minute flight of the Gossamer Albatross across the English Channel in 1979 and later by the flight of the solar-powered Solar Challenger²¹⁻²³.

Mini-RPVs flying at low altitudes may be used as target vehicles, decoys and for battlefield surveillance²⁴⁻²⁸. These vehicles are similar in size to highly efficient model airplanes usually with electronic payloads weighing less than 100 kg.

The growing interest in wind energy conversion using wind turbines provides still another important application. Although a wide variety of windwheel devices have been used for many years²⁹, recent interest has been concentrated on the vertical axis Darrieus rotor and on the horizontal propeller type rotor.

1.2 Design Aims

The design requirements cover a wide range when one considers the diversity of applications from RPVs to wind turbines. Almost all low Reynolds number vehicles share the ultimate goal of maximum aerodynamic efficiency. An aerodynamic efficiency map originally drawn by McMasters¹⁹ is shown in Figure 2. Areas assumed to cover the ranges of operation of high altitude aircraft platforms and low altitude mini-RPVs have been added to this figure. Since data of this type is generally unavailable for wind turbines, this item has not been included. A useful comparison of vehicle weight for a given wing/rotor area obtained from McMasters³⁰ is presented in Figure 3. In the region of interest in this study, vehicle mass greater than about 50 kg, the $Ma^{5/2}$ line captures the major trend. Two of the largest existing wind turbines, a recently proposed solar powered HAAP and an estimated region for mini-RPVs are also included on Figure 3.

Requirements for a typical low altitude mini-RPV, for example, include long flight duration (i.e., high value of $C_L^{3/2}/C_D$) at speeds between 10 and 25 meters/sec (i.e., chord Reynolds numbers from about 100,000 to 500,000) and altitudes from 30 to 300 meters, light weight, and all-weather capabilities³¹⁻³⁴ (i.e., precipitation, wind shears and unsteady wind). Minimum wing area for ease of packaging and pre-launch handling is also important. High altitude RPVs have somewhat higher speed, chord Reynolds number and endurance requirements; however, their cruise altitudes are usually free of the extremes of precipitation, wind shear and unsteady wind found near the earth's surface. They must, of course survive the initial journey from launch near sea level to their high altitude station. Wind turbine blades also require high aerodynamic efficiency and all-weather capabilities. The need for efficient low Reynolds number airfoils which are not overly sensitive to wind shear, gusts, and the roughness produced by precipitation is common to most mini-RPV vehicles. Furthermore, confidence that the operational vehicle will perform as designed is important in all applications.

1.3 Flow Problems

Although design methods developed over the past 20 years produce efficient airfoils for chord Reynolds numbers greater than about 500,000 these methods are generally inadequate for chord Reynolds numbers below 500,000. In relation to the airfoil boundary layer, important areas of concern are the separated regions which occur near the leading and/or trailing edges and transition from laminar to turbulent flow³⁵. It is well known that separation and transition are highly sensitive to Reynolds number, pressure gradient, and the disturbance environment³⁶. Transition and separation play a critical role in determining the development of the boundary layer which, in turn, affects the overall performance of the airfoil³⁵⁻³⁸. The aerodynamic characteristics of the wing and other components in turn affect the static, dynamic and aeroelastic stability of the entire vehicle. Therefore the successful management of the very sensitive boundary layer for a particular low Reynolds number vehicle design is critical.

At high Reynolds numbers, laminar flow rarely persists very far downstream of the leading edge as illustrated in Figure 4. In this flow regime, the wing is usually free of the relatively large laminar separation regions which occur at low Reynolds numbers as illustrated in Figures 5-7. Our incomplete physical understanding of the transition process, which controls the location of separation and reattachment, is the major shortcoming in designing this type of airfoil. At low Reynolds numbers the transition process is much more sensitive to free stream disturbances and aberrations of the airfoil geometry³⁷.

Laminar separation bubbles occur on the upper surface of most airfoils at low Reynolds numbers. These bubbles become larger as the Reynolds number decreases usually resulting in a rapid deterioration in performance, i.e., substantial decreases in (L/D) . In principle the laminar separation bubble and transition can be artificially controlled by adding the proper type of disturbance at the proper location on the airfoil. Wires, tape strips, grooves, steps, grit, or bleed-through holes in the airfoil surface have all been used to have a positive influence on the boundary layer in this critical Reynolds number region. The type and location of these so-called "turbulators" and their actual effect on the airfoil boundary layer has not been well documented. Furthermore, the addition of a turbulator does not always improve the airfoil performance³⁸. In fact, how the disturbances produced by a given type of turbulator influence transition is not well understood.

As a result of this critical boundary layer behavior, several important questions must be asked: 1) What is the free stream disturbance level and flight environment for a given low Reynolds number application? 2) If the flight conditions are known and a suitable design technique were available, could the resulting vehicle or component be adequately evaluated in a wind tunnel which, in general, has a different disturbance level and environment than the flight condition? 3) Is the hysteresis in aerodynamic forces observed in low turbulence wind tunnel experiments present in powered applications (i.e., do structural vibrations originating with the propulsion or drive system affect boundary layer transition)? 4) Because the critical quantities measured in wind tunnel experiments are very small what is the level of accuracy necessary to improve design and analysis methods?

1.4 Scope of Review

The purpose of the present review is to point out a number of design, analysis and experimental problems in low Reynolds number aerodynamics which are of major importance in the successful design and operation of vehicles in this regime. Although there are other important problems related to the vehicle structure, power system, control system, etc. this study will concentrate on the aerodynamic problems at subcritical speeds.

2. BOUNDARY LAYER BEHAVIOR

The magnitude and direction of the aerodynamic forces and moments acting on a moving vehicle (e.g., aircraft wing or wind turbine rotor) are determined to a large extent by the behavior of the boundary layer. These forces are related to how rapidly the viscous boundary layer grows and whether or not it separates from the vehicle's surface. The rate of growth of the boundary layer and whether separation occurs are strongly influenced by the character of this viscous layer (i.e., laminar, transitional and/or turbulent). This character of the boundary layer is a function of the vehicle shape, relative roughness of the surface, as well as the free stream disturbance level approaching the vehicle. The key to the boundary layer behavior for low Reynolds number vehicles is whether transition from laminar to turbulent flow takes place in the attached boundary layer before laminar separation occurs. Once laminar separation occurs, the subsequent laminar free shear layer is highly unstable and transition to turbulent flow takes place quite rapidly.

Several types of flow behavior result at low Reynolds numbers. First a laminar separation may occur near the leading edge at high angles of attack in which case the airfoil may be considered fully "stalled," or at small angles of attack the laminar boundary layer may remain attached through an extended favorable pressure gradient near the leading edge and then separate in an adverse pressure gradient after the maximum thickness of the airfoil. In either case an unsteady oscillating wake is formed which reduces airfoil performance.

A second type of boundary layer behavior may occur which is probably the most desirable at low Reynolds numbers. The best airfoil performance is achieved when the laminar boundary layer transitions to a turbulent one before reaching the large adverse pressure gradient. The turbulent boundary layer with the higher energy level is able to remain attached to the airfoil through the adverse pressure gradient. This "natural" transition (not caused by the separation bubble) is accompanied by higher lift coefficients and lower total drag coefficients. At high angles of attack, a trailing edge separation of the turbulent boundary layer provides gentle "stalling" characteristics.

A third type of boundary layer behavior occurs which may be considered an extension of the laminar separation case. Instead of remaining separated, the laminar free shear layer in some cases may reattach shortly after separation or the free shear layer more often may become turbulent, and the growing turbulent shear layer then interacts with the airfoil surface usually causing reattachment. After reattachment, the turbulent boundary layer behaves in a manner similar to the natural transition case although it thickens more rapidly. Theoretical prediction of the presence and location of the laminar separation bubble and experimental studies of the behavior of separation bubbles have been the focus of many previous investigations. Separation bubbles have been placed in two classifications: the short bubble and the long bubble. The short bubble typically occurs at high angles of attack and is usually less than a few percent of the chord in length at high Reynolds numbers. However at low chord Reynolds numbers Taniguchi³⁹ observed short separation bubbles that were approximately 28% of the chord in length. A short separation bubble at high Reynolds numbers has very little effect on the overall theoretical pressure distribution and usually decreases in size with increasing incidence. In comparison, the length of the long bubble is of more than a few percent of chord and will lengthen as angle of attack increases or Reynolds number decreases. The presence of a long bubble greatly alters the pressure distribution from its theoretical form. A separated laminar boundary layer is sometimes thought of as a long bubble extending into the wake of the airfoil. Figure 8 from References 40 and 41 illustrates the behavior of the pressure distribution with the formation of a long or short bubble.

As the chord Reynolds number decreases, the laminar portion of the free shear layer in a short bubble grows in length and the turbulent portion requires more entrainment to reattach at a pressure near the inviscid pressure value. Eventually the Reynolds number becomes so low and the laminar portion of the free shear layer so long that the turbulent entrainment process can no longer support reattachment near the inviscid pressure value. The velocity peak and circulation decrease reducing the pressure gradient over the bubble. This allows the turbulent free shear layer to reattach as a long bubble and the short bubble is said to have "burst" into a long bubble. This separation bubble decreases airfoil performance (i.e., increases pressure drag and results in a much thicker turbulent boundary layer downstream of the bubble) as compared to the natural transition case, but is a large improvement over the separated laminar boundary layer which does not reattach. The presence of a short laminar separation bubble can be utilized to improve airfoil performance at very low Reynolds numbers because it acts as a trip and reduces the possibility of massive separation further downstream.

Separation bubbles often have a dramatic effect on the stalling characteristics of airfoils. When a short bubble is present on an airfoil the lift increases linearly with angle of attack until stall occurs. A large discontinuous drop in lift usually accompanies the bubble burst at high Reynolds numbers as shown in Figure 9. If a long bubble forms on an airfoil, stall occurs when it has extended to the trailing edge. The resulting lift curve peak is fairly flat and has no discontinuities. At low Reynolds numbers these effects plus additional problems such as hysteresis are present.

Some airfoils exhibit a phenomenon near stall in which the aerodynamic forces developed depend on the direction the angle of attack was reached. As the angle of attack increases, the lift and drag forces increase. At stall, an abrupt decrease in lift and increase in drag occurs. A small reduction in the angle of attack, however, does not restore the forces to their former values. Instead, the angle may have to be reduced several degrees before the lift and drag suddenly revert to the values obtained under conditions of increasing angle of attack. This behavior shown in Figure 10 is described in Reference 42 as "high-lift" hysteresis and in Reference 43 as "high C_{Lmax} " or "clockwise" hysteresis and is attributed to the development and bursting of a short bubble.

The reverse situation may also occur in which an abrupt increase in lift and decrease in drag takes place at high angles of attack. The forces do not revert to the values obtained under conditions of increasing angle of attack until a sufficiently low angle is achieved as shown in Figure 11. Reference 42 calls this "moderate-lift" hysteresis and Reference 43 calls it "low C_{Lmax} " or "counterclockwise" hysteresis. This type of hysteresis appears to result from the growth of a long bubble and its sudden collapse into a short bubble.

2.1 Historical Background

The complex mechanisms of separation, transition and turbulence have been the focus of many investigations over the past half century. The phenomenon of separation bubbles was first studied by R.M. Jones in 1933⁴⁴. He noted the existence of a separation and reattachment of the flow over thin slightly cambered airfoils. In the early 1940's, F.W. Schmitz performed numerous experiments on model airplanes operating in the low Reynolds number regime⁴⁵. He was one of the first to recognize the advantage of the separation bubble in reducing drag by tripping the boundary layer and thus maintaining an attached flow over a larger portion of the airfoil. D.E. Gault, in a series of experiments conducted between 1949 and 1955^{46,47}, investigated the regions of separated laminar flow and categorized the types of boundary layer behavior. P.R. Owen and L. Klanfer⁴⁸ studied separation bubble bursting on a thin airfoil and made an attempt to develop a criterion for bursting. In 1956 W. Pfenninger studied the performance of gas turbine blades operating in the Reynolds number range of 30,000 to 100,000 and concluded that performance could be improved by shortening the separated laminar region artificially by means of disturbances introduced into the boundary layer⁴⁹.

Moore continuing the work of Owen and Klanfer in 1960, experimentally determined that when the Reynolds number based upon boundary layer displacement thickness was less than 500 at separation, that a long separation bubble was formed. When this parameter was greater than 500 a short bubble formed although it might burst as the airfoil angle of attack increased⁵⁰. Gaster performed an extensive study of the separation bubble in the 1960's^{41,51}. He established conditions under which short bubbles could burst to form long bubbles.

In an excellent review in the early 1960's, J.W. Ward combined experimental and theoretical results into a methodology for studying laminar separation and bubble formation⁵². It was generally accepted that to improve airfoil performance at low Reynolds numbers some type of mechanism was necessary to cause the laminar boundary layer to transition to a turbulent one. The formation of a separation bubble was one of several options. Other options included the use of boundary layer roughness or trips, increased free stream turbulence, transpiration (blowing of air into the boundary layer), or the use of the adverse pressure gradient itself. The formation of the laminar separation bubble and bubble bursting have been studied by Tani³⁹, Horton⁵³, Ntim⁵⁴, and Roberts⁵⁵.

In 1965, J.L. van Ingen conducted a theoretical and experimental study of the incompressible boundary layer and methods of influencing transition⁵⁶. More recently, D. Althaus has studied the influence of roughness introduced by insect remains on the performance of airfoils operating at low Reynolds numbers⁵⁷.

Up until the past few years, low Reynolds number studies of boundary layer performance (with the exception of Schmitz and Pfenninger) have concentrated on performance at Reynolds numbers above 500,000. Unfortunately, many low Reynolds number applications fall below this value. D.F. Volkers has studied the lift and drag performance of several airfoils between $Re_c = 60,000$ and 500,000⁵⁸. Arena and Mueller⁵⁹ and Mueller and Burns⁶⁰ made extensive use of flow visualization to study boundary layer performance below $Re_c = 500,000$. Most recently Conigliaro⁶¹ and Mueller, et al.³⁷ conducted studies of the airfoil section used on the first man-powered aircraft. Jansen⁶² completed a thorough study of the separation bubble on the NACA 663-018 airfoil. A detailed study of the boundary layer characteristics of the Miley airfoil between $Re_c = 70,000$ and 600,000 has been completed by Pohlen⁴⁰. Numerical studies of low Reynolds number airfoil flow problems have recently been performed for both steady and unsteady flows⁶³⁻⁶⁹. All of these previous studies have formed a basis for the study of airfoil performance at low Reynolds numbers which should help in the design of airfoils for this flight regime.

2.2 Laminar Flow

Laminar flows, whether steady or unsteady, two or three-dimensional, may be determined by a variety of analytical and numerical techniques. Entire laminar flows including regions of separation have been accurately determined using several different numerical methods of solution of the discretized Navier-Stokes equations with the appropriate boundary conditions. Using modern grid generation techniques⁷⁰ for arbitrary shapes, approximate solutions of this type are becoming commonplace. Attached laminar boundary layers may be calculated with a much smaller expenditure of programming and computer time by simply solving the laminar

boundary layer equations^{36,71}. Results of these methods have been found to be good although the prediction of laminar separation is not always as good as one would like. Once the laminar boundary layer separates, the calculations become difficult because the transition of this unstable shear layer to turbulent flow proceeds rapidly. The boundary layer equations can be used to calculate flows with thin separation regions. This procedure is usually referred to as the "viscid-inviscid" interaction⁷²⁻⁷⁶. All analytical and numerical techniques presently available suffer from our incomplete understanding of the transition process. Although transition in an attached boundary layer can occur in this Reynolds number range (i.e. at chord Reynolds number above about 300,000), transition after separation is more common.

2.3 Separation Bubble and Transition

The leading edge separation bubble as sketched in Figure 12 is formed when the laminar boundary layer separates from the surface as a result of the strong adverse pressure gradient downstream of the point of minimum pressure, shown in Figure 13. This separated shear layer is very unstable and transition usually begins (point T' on Figure 13) a short distance downstream of separation, as a result of the amplification of velocity disturbances present immediately after separation. After complete transition from laminar to turbulent flow (point T on Figure 13), the large turbulent shear stresses energize the shear layer by entraining fluid from the external stream so that it grows rapidly toward the airfoil surface, causing the pressure to rise. Reattachment occurs when the pressure is nearly equal to the value for the turbulent boundary layer over the airfoil with no separation bubble present, as shown in Figure 13. The inviscid flow solution value of pressure is also frequently used to determine reattachment location since it approximates the turbulent boundary layer case. The region between separation and reattachment is referred to as the separation bubble. The fluid in the laminar portion of the bubble moves very slowly, while the fluid in the turbulent portion moves vigorously in a recirculating pattern. Those factors which affect boundary layer separation also affect the separation bubble and transition in the separated shear layer, namely: thickness of the boundary layer at separation, angle of attack, free stream turbulence level and/or other free stream disturbances and surface roughness.

The transition process in the separated shear layer is the keystone which determines the size and shape of the bubble, as well as how rapidly the developing turbulent boundary layer grows over the remaining portion of the airfoil. Although the transition process in attached shear layers (especially on flat plates) has received a great deal of attention (e.g., References 36 and 77-81) transition in separated shear layers (especially in airfoil type pressure gradients) has received much less attention. Almost all of the previous research related to separated shear layer transition has been performed using either a two-dimensional backstep geometry⁸²⁻⁸⁵ or the exit of an axisymmetric free jet⁸⁶⁻⁸⁸. Both of these geometries produce a separated shear layer by an abrupt disappearance of the wall over which the shear layer is growing; that is, separation is forced by the abrupt change in geometry. In the case of the backstep, reattachment takes place downstream and a separation bubble is formed. For the axisymmetric jet experiments, no surface or wall is available for reattachment and no separation bubble is formed. The leading edge separation bubble on an airfoil is quite different from both of these since separation is caused by an adverse pressure gradient. This separation bubble and the separated shear layer transition appear to be more dependent on the interaction between the airfoil boundary layer and the external flow field around the entire airfoil. It is clear that while there must be some similarities in the transition process, no matter how it is caused, there must also be significant differences⁸¹.

It is generally agreed that transition from laminar to turbulent flow may be described as a series of events which take place more or less continuously, depending on the flow problem studied. Since turbulence is essentially a three-dimensional phenomenon, the breakdown of a two-dimensional laminar flow may be viewed as the process whereby finite amplitude velocity fluctuations, or traveling wave disturbances, acquire significant three-dimensionality⁸⁹⁻⁹¹. The velocity fluctuation or traveling wave front which is initially straight develops spanwise undulations that are enhanced by second order effects, as depicted in Figure 14. Transition has been very graphically described as the process by which the straight and parallel vortex lines of a two-dimensional laminar flow deform into a constantly changing and twisting three-dimensional mess called "turbulence"⁷⁸. This is best described by a quote from Reference 78:

"It is not the mere presence of vorticity that characterizes turbulence. It's the complexity of the vorticity field. In a laminar boundary layer, the vortex lines are parallel and stacked near the wall, like uncooked spaghetti. In the turbulent layer, the vortex lines are constantly changing and twisting. Near the wall, major entanglements appear, and the vortex lines may develop knots and crossover points. The spaghetti is cooked."

Still photographs and high speed movies of the smoke filaments (i.e., streaklines) produced by passing an electrical current through a 5 mil wire coated with oil (Reference 92), clearly delineate the fine details of the separated shear layer from the leading edge of the airfoil. Figure 15 was obtained using this technique known as the "smoke-wire" method. The transition process in the separated shear layer is seen in all of its complexity. A preliminary examination of these smoke photographs substantiates the notions of a highly unstable two-dimensional flow which breaks down in a very definite manner to a three-dimensional turbulent flow. These smoke photographs represent the most definitive visual description of separated shear layer transition available. Some structure is also visible in the developing turbulent flow. Although this visual technique is only suited for chord Reynolds numbers less than 100,000, the basic transition process should follow the same series of events at higher Reynolds numbers. For example, for the same airfoil, the beginning of the transition process moves towards the separation location as the free stream velocity is increased. The length of the transition region also decreased with higher free stream velocities.

2.4 Low Reynolds Number Turbulent Flow

Integral methods of solving the turbulent boundary layer equations have been in wide use following the development of Prandtl's mixing length hypothesis in 1925³⁶. Both the variety and complexity of the integral methods increased with time until the 1968 Stanford Conference which was designed to determine the accuracy of the available turbulent boundary-layer prediction methods⁹³. The results of this conference demonstrated that the partial differential equation methods provided more accurate predictions of turbulent boundary-layers than the best integral techniques. These more complex methods using large-fast digital computers were able to predict detailed features of turbulent flows. It became clear at this time that more physical experiments were needed in turbulent flows so that the numerical semi-empirical turbulence models could be improved. These physical experiments greatly increased our understanding of the basic structure of turbulence^{94,95,96} as well as the path from laminar to turbulent flow^{97,98}.

The development of numerical techniques used to solve the Navier-Stokes equations with turbulence modelling has been very rapid in the past few years⁹⁹⁻¹⁰¹. Approximate calculations of this type, should eventually be useful for engineering purposes.

At low chord Reynolds numbers on an airfoil, the turbulent boundary layers are usually in the stage of developing after attached transition or redeveloping after reattachment when a separation bubble is present. These boundary layers are in general far from the fully-developed concept. In these developing or redeveloping boundary layers it appears plausible that their structure is dependent upon the mechanism of transition as well as the pressure gradient, etc. Although low Reynolds number turbulent boundary layers on airfoils have only recently begun to receive a lot of attention, the smoke visualization photograph shown in Figure 16 presents a global view of this problem. Figure 16 shows a short leading edge separation bubble followed by a redeveloping turbulent boundary layer on a NACA 23012 airfoil at a chord Reynolds number of 123,800 and an angle of attack of 14° ¹⁰². The separation bubble (about 12% of the chord in length) and the vortex formation in the free shear layer, indicating the onset of transition, are clearly visible in Figure 16.

3. DESIGN AND MODELING PROCEDURES

It is not surprising that the early airplane designers looked to flying creatures in nature for help. With birds for inspiration and the empirical process of cut and try flight and/or wind tunnel experiments, airfoil/wing designers made slow but steady progress from the beginning of this century until the early 1920's. This procedure is referred to as "design by experiment" and is illustrated in the left side of Figure 17. The additional help obtained from potential flow theory in the 1920's led to more systematic experimental programs, mainly at NACA and Goettingen, which resulted in catalogs of airfoil sections. These catalogs of airfoil section characteristics were very useful to the designer¹⁰³⁻¹⁰⁵. This procedure is essentially the same "design by experiment" one except trial and error has been helped a great deal by the use of potential flow theory.

Although boundary-layer theory was born at Gottingen in 1904, it wasn't until the middle of the 1930's that it was developed enough to be incorporated into the design procedures of airfoil sections. The realization of the importance of viscous effects resulted in the well known NACA 6-series "laminar flow" airfoils. The airfoil design procedure, though guided by this type of analysis, was still mostly experimental as indicated on the left side of Figure 17. The 6-series of airfoils with minor modification dominated the aircraft design field until the late 1950's when the digital computer revolution began to be a factor. At this point in history, theoretical considerations could be used to do more than just guide the experimental program.

In the late 1950's, the power of large computers was applied to designing low speed airfoils by combining potential and viscous flow theories. In these so-called "inverse methods", the designer starts with the desired performance characteristics, etc. and ends with the airfoil shape which satisfies these characteristics. This was the beginning of tailoring airfoil sections for specific applications and the general procedure, referred to as "design by synthesis", is shown on the right side of Figure 17. The early application of inverse airfoil design techniques for low-speeds was accomplished primarily by Wortmann^{38,106,107} and Eppler^{108,109}. Additional contributions in this area have been provided by Miley¹¹⁰, Henderson^{111,112}, Liebeck¹¹³, van Ingen^{114,115}, Lissaman¹¹⁶, Eppler and Somers¹¹⁷⁻¹¹⁹, and many others.

Although the particular methods used to solve the complex governing equations for the inviscid and viscous flow over an airfoil in the inverse mode differ considerably, all successful inverse design methods must contain the following elements:

- Potential Flow Calculation Procedure
- Laminar Boundary Layer Calculation Procedure
- Laminar Separation Criterion
- Laminar Separation Bubble Prediction
- Transition Criterion
- Turbulent Boundary Layer Calculation Procedure
- Turbulent Separation Criterion

The "design by synthesis" approach begins with the boundary layer characteristics and their effect on the pressure distribution so that the airfoil shape which results meets the originally desired performance characteristics. Although several iterations in the procedure are usually made the airfoil shape appears as the final product. This is exactly the opposite of the "design by experiment" method where an airfoil shape is chosen at the beginning of the procedure.

3.1 The Eppler Airfoil Design and Analysis Program

The airfoil design program developed by Eppler over the past 25 years has been very useful in designing airfoils for incompressible flow and is a good example of the "design by synthesis" approach. This program combines a conformal-mapping method for the design of airfoils with prescribed velocity-distribution characteristics, a panel method for the analysis of the potential flow about a given airfoil, and a boundary layer method. It has been successfully applied at chord Reynolds numbers from 2×10^4 to 1×10^8 .

3.1.1 Theory

The airfoil design method is based on conformal mapping. This method differs from other inverse methods in that the velocity distribution is not specified for only one angle of attack. Instead, angles of attack which will result in constant velocity over specified segments of the airfoil are input. In other words, pairs of parameters are specified: the segment of the airfoil and the angle of attack relative to the zero-lift line which will result in constant velocity over that segment. Of course, some matching conditions must be met to guarantee a smooth velocity distribution for all angles of attack. Toward the trailing edge, on both surfaces, a main pressure recovery can be specified. Finally, a short closure contribution must be introduced to insure that the trailing edge will be closed.

In reality, the segments corresponding to the various input angles of attack are not specified in the airfoil plane but rather in the conformal-mapping plane in which the airfoil is represented by a circle. So far, no difficulties have arisen in correlating the arcs of the circle with the segments of the airfoil.

It should be remembered that for any given velocity distribution there does not necessarily exist a "normal" airfoil. For example, the closure contributions could be quite large which would result in a very large trailing-edge angle. The closure contributions could also give rise to a region of negative thickness near the trailing edge. Accordingly, several iteration options have been included which allow the trailing-edge angle to be specified while certain input angles of attack or the total amount of pressure recovery is iterated.

The potential flow airfoil analysis method employs panels in the conformal-mapping plane with distributed surface singularities. The geometry of the panels is determined by a spline fit of the airfoil coordinates, with the end points of the panels being the input airfoil coordinates themselves. The singularities used are vorticities whose strength are distributed parabolically along each panel. The flow condition, which requires the inner tangential velocity to be zero, is satisfied at each airfoil coordinate (i.e., at the end points of the panels, not the midpoints). Two angles of attack, 0° and 90° , are analyzed. The flow for an arbitrary angle of attack can be derived from these two solutions by superposition. The entire procedure does not require any restrictions on the input point distribution, smoothing, or rearranging of the coordinates; only the original airfoil coordinates are used. An option is included by which additional points can be splined in between the original coordinates. This option allows more precise results to be obtained should a portion of the airfoil have a sparse distribution of points.

A flap deflection can be introduced by geometrically rotating part of the airfoil about a flap hinge point. The connection between the forward portion of the airfoil and the flap is defined by an arc consisting of additional points which are generated automatically according to an input arc length. In addition, an option is included which allows the analysis of chord-increasing flaps. It should be noted that, while the airfoil shape which results form the exercise of this option does have an increased chord, it does not contain a slot, and thus, is still a single-element as opposed to a multi-element airfoil.

The laminar and turbulent boundary-layer development is computed using integral momentum and energy equations. The approximate solutions obtained from the laminar boundary-layer method agree very well with exact solutions. The turbulent boundary-layer method is based on the best available empirical skin-friction, dissipation, and shape-factor laws. No further errors are introduced by mathematical simplifications like integrating the ordinary differential equations from the momentum and energy laws by averaging the right sides of the equation.

Of special interest are the predictions of separation and transition. The prediction of separation is determined solely by the shape factor based on energy and momentum thicknesses. (Note that this shape factor has the opposite tendency of the shape factor based on displacement and momentum thicknesses.) For a laminar boundary layer, there exists a constant and reliable lower limit of this shape factor, which equals 1.515 and corresponds to laminar separation. For turbulent boundary layers, no such unique and reliable limit has been determined. It can be stated, however, that the turbulent boundary layer will separate if the shape factor goes below 1.45 and will not separate if the shape factor remains above 1.58. It has also been determined that thicker boundary layers tend to separate at lower shape factors. Because the present method yields lower shape factors for adverse pressure gradients than other methods, turbulent separation is assumed when the shape factor equals 1.46. The uncertainty is not as bad as it first appears because the shape factor changes rapidly near separation. Nevertheless, results must be checked carefully with respect to turbulent separation.

The prediction of transition in the Eppler method is based on an empirical criterion which contains the Reynolds number, based on local conditions and momentum thickness, and the shape factor. This criterion predicts that transition occurs later if the shape factor is higher (i.e., the pressure gradient is more favorable). The criterion also contains a "roughness factor" which allows various degrees of surface roughness and/or free-stream turbulence to be simulated. The prediction of transition results in a switch from the laminar skin-friction, dissipation, and shape-factor laws to the turbulent ones, without changing the shape factor of the momentum thickness. The program contains two options for fixing transition as well as an option which allows the analysis of the effect of single roughness elements on a turbulent boundary layer.

The boundary-layer characteristics at the trailing edge are used for the calculation of the profile-drag coefficient by a Squire-Young type formula. The program generally predicts slightly higher drag coefficients than those measured experimentally. However, the differences between the predictions and experimental measurements depend on the wind tunnel in which the experiments were performed and, therefore, neither the skin-friction laws nor any other part of the program has been changed in order to "tune" the predictions to a particular wind tunnel or set of experimental data.

The lift and pitching-moment coefficients are determined from the potential flow. Viscous corrections are then applied to these coefficients. The lift-curve slope where no separation is present is reduced to 2π from its theoretical value. In other words, the potential-flow thickness effects are assumed to be offset by the boundary-layer displacement effects. A lift coefficient correction due to separation is also included. As an option, the displacement effect on the velocity distributions and the lift and pitching-moment coefficients can be computed.

3.1.2 Examples Using Eppler's Method

The first example is a low-Reynolds number airfoil (Eppler 387) designed for model airplanes. The comparison of the predictions and the experimental results of Reference 120 is shown in Figure 18. For a Reynolds number of 200,000 (Figure 18a), the agreement between theoretical and experimental section characteristics is good. No pitching-moment coefficients were measured. For a Reynolds number of 100,000 (Figure 18b), the agreement between theoretical and experimental lift curves is good. The predicted maximum lift coefficient is conservative (low). The agreement between theoretical and experimental drag coefficients is reasonably good at the limits of the low-drag range but rather poor in between these limits. This poor agreement is due to the effect of laminar separation bubbles on the measured drag coefficients. While the program predicts the existence of significant laminar separation bubbles at these lift coefficients, it does not account for the influence of the bubbles on the drag. For a Reynolds number of 60,000 (Figure 18c), the agreement between theoretical and experimental lift curves is not as good as at the higher Reynolds numbers. The predicted maximum lift coefficient is again conservative. The program predicts laminar "stall" at moderate lift coefficients (~ 0.6) and the turbulent reattachment which results in a relatively high maximum lift coefficient. While the occurrence of the various boundary-layer phenomena is predicted well, the influence on the drag coefficients is not.

The second example is a natural-laminar-flow airfoil (NASA NLF(1)0416) designed for general aviation applications. The comparison of the predictions and the experimental results of Reference 121 for a Reynolds number of 2×10^6 is shown in Figure 19. The agreement between theory and experiment is considered excellent. The magnitudes of both the angle of attack for zero lift coefficient and the pitching-moment coefficients are overpredicted because the displacement-iteration option was not exercised.

The third example is a flapped natural-laminar-flow airfoil (NASA NLF(1)-0215F) designed for high-performance general aviation applications. The comparison of the predictions and the experimental results of Reference 122 for a Reynolds number of 9×10^6 and a simple flap deflection of -10° is shown in Figure 20. The agreement between theoretical and experimental lift curves is good. The pitching-moment coefficients are only slightly overpredicted, even though the displacement-iteration option was not exercised, because the displacement effect for this configuration and Reynolds number is small. The predicted drag coefficients are conservative (high) with the exception of those at the lower limit of the low-drag range. It is felt that the disagreement is the result of the increased turbulence level in the wind tunnel at this high unit Reynolds number ($4.5 \times 10^6/\text{ft}$) which causes premature transition.

3.1.3 Remarks

This program represents a mathematical model of the two-dimensional viscous flow around airfoils and has produced very good results. The major shortcoming of this program is the lack of a separation bubble model. Since it appears that at chord Reynolds numbers below 500,000 a laminar separation bubble is always present and may vary in size from about 2% to 20% of chord, the inclusion of the bubble in the analysis program would improve the determination of lift and drag for some cases.

3.2 Viscous-Inviscid Interaction Methods

In the interest of predicting laminar separation and the development of separation bubbles on airfoils, another approach has been followed by several researchers⁷²⁻⁷⁵. These methods are based on the assumption that the boundary layer equations are applicable in the thin regions of separated flow and follow one of two approaches.

The first approach involves numerically integrating the differential form of the boundary layer equations. In the attached regions of the boundary layer, this can be accomplished in a straight forward manner using the external velocity as a boundary condition. When separation occurs, however, the equations become singular. It then becomes necessary to use an inverse boundary layer solution. This usually entails specifying the boundary layer displacement thickness and solving for the external velocity. Numerical instabilities still arise in the separated region when the solution marching direction is opposite to the flow direction. This difficulty is usually handled by making the so-called FLARE approximation, i.e., by assuming the streamwise convection terms are zero. Davis and Carter⁷⁴, however, describe how, in their method, the usual backward difference operator was switched to a forward difference operator in regions of reversed flow.

The resulting solution to the boundary layer equations must be verified since the input displacement thickness is only a guess. Using the methods of inviscid flow theory, a velocity perturbation due to the displacement thickness of the separated flow region is computed. This perturbation is then added to the external velocity which occurs when separation is not present on the airfoil. The result is compared to the external velocity which was obtained from the boundary layer solution. If necessary, the trial displacement thickness is modified and the process is repeated. This is the iteration interaction step for the

"viscous-inviscid" procedure. References 72 to 74 use this general approach for obtaining flow solutions when separation bubbles are present on an airfoil. The individual methods primarily differ in the way the velocity perturbation is computed and in the handling of the transitioning and turbulent boundary layer.

The method of Cebeci and Clark⁷² computes the velocity perturbation using a surface singularity distribution to simulate the displacement effects of the boundary layer. It apparently can account for the change in circulation due to viscous effects. The transition location is determined using an empirical relationship which is based on the flow conditions at the separation point. The effects of freestream turbulence do not seem to be accounted for. The turbulent stress in the momentum equation is determined using a two layer turbulence model. In the transition region, the stress is modified by an intermittency factor.

The technique of Kwon and Pletcher⁷³ uses a source distribution to account for the displacement thickness. The change in circulation due to flow separation is not determined. The point where transition begins in the free shear layer is assumed to coincide with the end of the separation bubble's constant pressure region. This location is obtained using an empirically derived relation based on the separation Reynolds number. Freestream turbulence effects are not considered. A method similar to that of Cebeci and Clark⁷² is used to obtain the turbulent stress.

The computer code of Davis and Carter⁷⁴ also uses a source distribution to compute the velocity distribution. Viscous effects on the airfoil's circulation are not determined. The Reynolds stress is calculated in the transition and turbulent regions using a methodology which accounts for the magnitude of the freestream turbulence. This method, however, was unable to predict transition early enough at conditions of low freestream turbulence for separation bubbles to form, a contradiction to experimental observations.

The output of these calculations is usually presented in the form of wall shear distributions, velocity profiles, pressure distributions, and displacement thickness plots. The results are encouraging, however, their present application to the case of low Reynolds number flows is somewhat doubtful. One reason for this is that no reliable sensitivity to the magnitude of freestream turbulence has been built into the methods. Furthermore, the programs (except that of Reference 72, perhaps) cannot handle the fairly large separation regions that occur near the trailing edge of airfoils operating at low Reynolds numbers. Finally, it was noticed in Reference 74 that between 50 and 100 iterations were required to solve the case of a small (about 3 percent of the chord in length) separation bubble. At low Reynolds numbers, the length of a bubble may be 10 times greater. Thus, computational time might be prohibitive for such cases.

The second numerical approach, which is described by Gleyzes et al.⁷⁵, involves solving the integral form of the boundary layer equations in an inverse mode. Again, viscous-inviscid interaction is required. In the laminar and turbulent regions of the boundary layer, closure is obtained using relationships derived from the self-similarity class of solutions. In the transition region, the characteristics of two fictitious boundary layers one laminar, the other turbulent are combined using an intermittency weighting function. The onset of transition is predicted using a relation between an amplification parameter derived from the neutral stability curves of separated flows and the local turbulence level. The predictions of this method have been compared with experimental data⁷⁵ in which the chord Reynolds numbers ranged from 2 to 8 million. Turbulence levels were generally low (less than 0.5 percent), however, a case in which the turbulence level was 2.5 percent was also examined. The predictions were good with regard to the bubble's effect on the downstream momentum thickness. The bubble's influence on the velocity distribution was not estimated as reliably. Because the program cannot account for trailing edge separation effects, its utility for low Reynolds number cases is doubtful.

Little work appears to have been done concerning long separation bubbles. This is probably due to two reasons. First, their negative effect on performance causes the airfoil designer to avoid developing sections on which long bubbles can form. Thus, it is of primary concern that one be able to anticipate the conditions under which long bubbles form. Knowledge of their characteristics, however, is not important provided that their formation can be eliminated.

The second reason is that the characteristics of long bubbles may be more difficult to predict than those of short bubbles. Their presence on an airfoil significantly alters its pressure distribution which invalidates the use of a small velocity perturbation to account for the effect of a bubble. In addition, McCullough and Gault⁴⁶ reported the presence of a pressure gradient normal to the airfoil surface in the vicinity of a long bubble. Thus, one of the assumptions of the boundary layer concept is violated. For these reasons, the numerical methods described may not be usable for estimating the properties of long bubbles.

The recent work of Cheng⁷⁶ in this area of viscous-inviscid interaction methods warrants special mention. Cheng uses the triple-deck/Kirchoff-wake model of Sychev, Messiter and Smith and its extension to represent the steady-state Navier-Stokes solutions in the limit as $Re \rightarrow \infty$. Although the triple deck methods have been successful in solving a variety of laminar flow problems, they have experienced difficulties in handling transitional and turbulent problems because of our incomplete understanding and modelling of these phenomena. This recent work treats symmetrical and asymmetrical cases with lift and addresses the global problems of wake closure, including laminar reattachment upstream of the trailing edge. The objective of this work was to explore the manner of switching from a grossly separated flow to a fully attached flow as the profile thickness varied. The results of this steady-state approach produced multiple solutions representing flow structures with open and closed wakes. The investigation of flow asymmetry has added to the multiplicity of the bifurcating solutions. The availability of two solutions for an airfoil at incidence may explain the existence of the upper and lower boundaries for lift hysteresis. Furthermore, the corresponding result for a symmetric airfoil at zero incidence provides an explanation for asymmetric flow over geometrically symmetrical flow structures that have been well documented in low Reynolds number airfoil experiments. Although transition to turbulent flow is an important factor in the wind tunnel experiments, the work of Cheng indicates a completely laminar mechanism for airfoils in the "subcritical range". This

10 theoretical approach (limited though it may be) appears to be the only one which predicts the existence of hysteresis on an airfoil at incidence and the possibility of flow asymmetries for a symmetrical airfoil at zero incidence. Although they are not design methods, the viscous-inviscid interaction methods are helpful in analyzing specific airfoil problems and have added to our understanding the role of separated regions in airfoil flow fields.

3.3 Numerical Modeling

As has been emphasized, the low Reynolds number flow field over an airfoil is frequently dominated by a large laminar separation bubble and subsequent transition from laminar to turbulent, or nearly turbulent conditions. The extent and nature of separated flow over the airfoil is governed by the aerodynamic characteristics of this separation bubble and transitional flow. Hence, any computational effort to model this flow should take into account the realistic fluid physics, both in regard to the separation and transitional effects. Boundary layer solutions, no matter how high the order, may overlook some of the important physics of the separated flow. Therefore, efforts have been underway to approximately solve the complete two-dimensional Navier-Stokes equations for low Reynolds number flow over airfoils. In this approach, no modeling is required for the separated flow regions. Of course, with regard to the transitional nature of the flow, any calculation, Reynolds averaged Navier-Stokes or otherwise, is going to be dependent on the particular turbulence model employed. Although these approximate numerical procedures are not suitable at the present time for design purposes, they are becoming increasingly useful for analysis. As the turbulence modeling improves and computational time decreases, these methods will be more and more helpful to the designer. An example of this approach is the work of Kothari, Anderson and Raghaven⁶⁹. Their current calculations treat compressible flow to allow application from low to transonic flight conditions.

3.3.1 Physical Problem and Governing Equations

Consider a two-dimensional, compressible viscous flow. The Reynolds-averaged, time-dependent Navier-Stokes equations³⁶ in cartesian coordinates can be written in non-dimensional form²³ as

$$\frac{\partial \bar{U}}{\partial t} + \frac{\partial \bar{F}}{\partial x} + \frac{\partial \bar{G}}{\partial y} = 0$$

where

$$\bar{U} = \begin{cases} \rho \\ \rho u \\ \rho v \\ \rho E \end{cases}$$

$$\bar{F} = \begin{cases} \rho u^2 + p + \frac{2}{3} \mu \left(\frac{\partial u}{\partial x} + \frac{\partial v}{\partial y} \right) / Re - 2 \mu \left(\frac{\partial u}{\partial x} \right) / Re \\ \rho uv - \left(\frac{\partial u}{\partial y} + \frac{\partial v}{\partial x} \right) / Re \\ \rho uH - P_{rmg} k \frac{\partial T}{\partial y} + \frac{u}{Re} \left[\frac{2}{3} \mu \left(\frac{\partial u}{\partial x} + \frac{\partial v}{\partial y} \right) - 2 \mu \frac{\partial u}{\partial x} \right] + \frac{v}{Re} \left[-\mu \left(\frac{\partial u}{\partial x} + \frac{\partial v}{\partial y} \right) \right] \end{cases}$$

$$\bar{G} = \begin{cases} \rho v \\ \rho uv - \mu \left(\frac{\partial v}{\partial x} + \frac{\partial u}{\partial y} \right) / Re \\ \rho v^2 + p + \frac{2}{3} \mu \left(\frac{\partial u}{\partial x} + \frac{\partial v}{\partial y} \right) / Re - 2 \mu \left(\frac{\partial v}{\partial y} \right) / Re \\ \rho vH - P_{rmg} k \frac{\partial T}{\partial y} + \frac{v}{Re} \left[-\mu \left(\frac{\partial u}{\partial x} + \frac{\partial v}{\partial y} \right) \right] + \frac{u}{Re} \left[\frac{2}{3} \mu \left(\frac{\partial u}{\partial x} + \frac{\partial v}{\partial y} \right) - 2 \mu \left(\frac{\partial v}{\partial y} \right) \right] \end{cases}$$

In the above, all quantities are nondimensionalized by reference quantities (subscript r) and are related to the dimensional quantities (primed variables) as

$$\begin{aligned} x &= x'/L, & y &= y'/L, & t &= t'/(L/V_r), & u &= u'/V_r, \\ v &= v'/V_r, & \rho &= \rho'/\rho_r, & T &= T'/T, & p &= p'/\rho_r V_r^2 \\ \mu &= \mu'/\mu_r, & k &= k'/k_r, & H &= H'/V_r^2, & E &= E'/V_r^2 \end{aligned}$$

where

E' = total internal energy per unit mass and

H' = total enthalpy per unit mass = $E' + RT'$.

Also,

$$R_e = \frac{\rho_r V_r L}{\mu_r}$$

$$P_{rmg} = \frac{1}{P_r R_e (M_r)^2 (\gamma_r - 1)}$$

$$M_r = \frac{V_r}{\sqrt{\gamma_r R T_r}}$$

$$\gamma_r = C_{p_r} / C_{v_r}$$

$$P_r = \mu_r C_{p_r} / k_r$$

These equations are transformed into curvilinear coordinates (ξ, η) which are related to (x, y) through

$$\xi = \xi(x, y) \text{ and } \eta = \eta(x, y).$$

The transformed equations are

$$\frac{\partial \bar{U}'}{\partial \bar{t}} + \frac{\partial \bar{F}'}{\partial \xi} + \frac{\partial \bar{G}'}{\partial \eta} = 0$$

where now,

$$\bar{U}' = J' \bar{U}$$

$$\bar{F}' = \bar{F} \frac{\partial y}{\partial \eta} - \bar{G} \frac{\partial x}{\partial \eta}$$

$$\bar{G}' = -\bar{F} \frac{\partial y}{\partial \xi} + \bar{G} \frac{\partial x}{\partial \xi}$$

$$\text{and Jacobian } J' = \left(\frac{\partial x}{\partial \xi} \right) \left(\frac{\partial y}{\partial \eta} \right) - \left(\frac{\partial x}{\partial \eta} \right) \left(\frac{\partial y}{\partial \xi} \right)$$

The curvilinear coordinates allow a boundary-fitted coordinate system to be wrapped around the airfoil. The details of the transformation and the resulting equations are given in References 69 and 123.

The molecular viscous coefficient is given by Sutherland's law

$$\frac{\mu'}{\mu_r} = \left(\frac{T'}{T_r} \right)^{\frac{3}{2}} \left(\frac{T_r + 110}{T' + 110} \right)$$

and the thermal conductivity is obtained from $k' = \mu' C_p' / P_r$ assuming a constant Prandtl number of 1.0. These molecular values are added to the turbulent transport properties obtained with the Baldwin-Lomax turbulence model¹²⁴ which only includes the Reynolds stress.

The grid utilized for the calculations presented here is generated by the elliptic grid technique of Thompson¹²⁵. For subsonic applications, this grid is extended a large distance away from the body, as shown in Figure 21. Here, the airfoil is discernible as a small speck in the middle of the grid. A detail of the grid in the near vicinity of the airfoil is shown in Figure 22. The airfoil shown in Figures 21 and 22 is the Miley airfoil investigated in Reference 40.

3.3.2 Numerical Technique

The discretized Navier-Stokes equations are solved by means of an implicit time-dependent finite-difference technique patterned after MacCormack¹²⁶. Reference 126 treats the case of rectangular coordinates. The modifications necessary for a curvilinear coordinate system are detailed in Reference 69. The time-dependent technique starts with assumed initial conditions throughout the flowfield (at time = 0), and calculates the flow in steps of time. At large times, the steady-state flow is approached. It is this steady flow that is of interest; the time-dependent technique is simply a means to that end.

3.3.3 Typical Results

Consider the laminar flow over a Miley airfoil at $M = 0.5$ and $R_c = 100,000$ (based on chord). The calculated streamlines for this flow are shown in Figure 23 for zero degrees angle-of-attack. This streamline pattern agrees in general with smoke flow photographs at the University of Notre Dame⁴³. Note the massive separation downstream of the maximum thickness of the airfoil. The calculated variation of pressure coefficient over the airfoil is given in Figure 24, and is compared with experimental values from Pohlen and Mueller⁴⁰. Reasonable agreement is obtained. Finally, the calculated variation of lift and drag coefficients with angle of attack is shown in Figure 25, along with the experimental values given in Reference 40. Again, reasonable agreement is obtained for $\alpha < 10^\circ$. This agreement is particularly important in light of the tenuous nature of low Reynolds number data for airfoils. Indeed, Figure 25 demonstrates the value of such Navier-Stokes calculations for Reynolds numbers low enough where experimental data is questionable or non-existent. The lack of agreement at large α is due to this particular set of calculations being completely laminar, whereas transition is occurring in the actual experiments.

In addition to the Miley airfoil, another airfoil of interest viz. a Wortmann FX 63-137 airfoil was also included in the computational simulation experiment. The streamline pattern for zero degrees angle of attack is shown in Figure 26 for $R_c = 100,000$. The flow separates on both upper and lower sides of the airfoil, with upper surface separation being more massive. It should again be noted that the solution here is completely laminar and in the case of the actual experiments at $R_c = 100,000$ transition could occur causing the flow on the lower and upper surfaces to reattach.

Although approximate numerical solutions of this type are not suitable for design purposes they make an important contribution to our understanding of the complex unsteady separated flow problems encountered with low Reynolds number airfoils. As our ability to model transition and turbulence improves, this approach will become more helpful to the designer.

4. EXPERIMENTAL EVALUATION OF DESIGN

Although new airfoil sections may now be obtained using the "design by synthesis" methods, the final proof of any design is its performance under actual operating conditions. The most economical method of verifying a given airfoil design is to simulate actual operating conditions (i.e., flight conditions) in a wind tunnel. Wind tunnel experiments, if carefully performed and documented, usually provide a reasonable evaluation of how an airfoil section will perform in flight.

Since the overall performance of airfoils at low Reynolds numbers is very sensitive to the location of transition, care must be exercised to understand the peculiar wind tunnel disturbance environment and its effect on transition. Because each wind tunnel facility is different in its disturbance environment, it may be desirable to use a sailplane or an appropriately designed RPV as a test bed to verify airfoil designs under realistic flight conditions.

4.1 Wind Tunnel Experiments

To evaluate and improve existing airfoil design procedures, accurate wind tunnel data are needed. These data include lift, drag and moment measurements, as well as the determination of the location of transition and separation on two-dimensional airfoil sections and finite wings. The experimental studies discussed below will emphasize the research performed at the University of Notre Dame. The data presented are representative of the work initiated in the early 1970's and indicative of the ongoing nature of the types of investigations being carried out at Notre Dame. As is typical for any research laboratory, these facilities have grown and progressed in accordance with time, resources, and experience.

4.1.1 Influence of Experimental Technique and Procedure

The lift force can be determined with acceptable accuracy using a strain gauge balance. If small pressure differences can be measured accurately, then a reasonably accurate lift force can also be obtained by integrating the static pressure distribution around the airfoil. In an atmospheric wind tunnel at low Reynolds numbers this requires accurate pressure difference measurements below 1 mm of water.

Since airfoil drag forces are at least an order of magnitude smaller than the lift forces, they are much more difficult to measure accurately when tests are conducted at low R_c . To measure these very small drag forces (e.g., 0.015 N for a 250 mm chord, 403 mm span NACA 663-018 airfoil section at $R_c = 40,000$ or 0.01N for a 152 mm chord, 412 mm span FX 63-137 airfoil section at $R_c = 80,000$), a very sensitive, specially designed strain gauge balance arrangement with high signal to noise ratio and low drift electronics is needed. A balance system of this type is within the state-of-the-art and has been under development at the University of Notre Dame. The major difficulty with this technique is the determination of interference effects between airfoil and side plates¹²⁷. A sketch of some of the possible three-dimensional flow phenomena which may occur in the vicinity of the airfoil/side plate region is shown in Figure 27. These phenomena are dominated by flow separation and the formation of a corner vortex. It is clear that the force contribution of the end of a finite span airfoil is different from the infinite span airfoil it attempts to represent. At low chord Reynolds numbers (i.e., $R_c < 100,000$), the region affected by side plate interference may be as large as 5% of the span (10% of the span if side plates are at both ends of the airfoil). As Reynolds number increases, this region of three-dimensional flow decreases in size and effect. As a result of this three-dimensional corner flow region near the ends of the airfoil, the measured drag forces are expected to be higher than for the infinite span airfoil.

Another, often used, method of determining drag is the wake traverse method. This method has been used successfully at high Reynolds numbers for several decades. At first glance there appears to be no reason why the wake traverse should not produce good results at low Reynolds numbers if the static and total pressures can be measured accurately. However, for $R_c < 100,000$, most airfoil wakes are composed of large-scale vortices which produce an unsteady or oscillating wake somewhat similar to the one behind a circular cylinder (see Figure 28).

A fixed static and total pressure rake, as indicated in Figure 28, is subject to errors related to the changing flow direction. The velocity distribution obtained from the wake traverse is used in the momentum equation written in the direction parallel to the test section centerline. The airfoil drag is then assumed to be equal to the decrease in momentum in this direction. Since these low Reynolds number airfoil flows are dominated by large-scale vortices, accurate measurement of the velocity component parallel to the test section centerline is very difficult, if possible at all, with a rake wake. The following quote from Pope and Harper¹²⁸ supports this argument: "The wake survey cannot be used to measure the drag of stalled airfoils or of airfoils with flaps down." The drag determined by this method appears to be lower than the actual drag. Furthermore, at these low Reynolds numbers, laminar separation and transition, usually on the airfoil upper surface, very often produce a large-scale spanwise flow structure⁹² (see Figure 29). The measurement of static and total pressures with a rake in such an oscillating wake can be subject to considerable error, even if the small pressure differences can be accurately resolved. This problem is compounded when a significant spanwise flow structure is present. To adequately account for the spanwise variations, the rake must be traversed in the spanwise direction.

A recent study of the variation of the measured drag in the spanwise direction using a wake rake was performed by Althaus¹²⁹. Using an integrating rake, an analog-digital converter and a digital computer system, drag data for $1,000,000 < R_c < 3,000,000$ was obtained. The airfoil which spanned the tunnel had a span of 73 cm and a chord of 50 cm. The results of this experiment are shown in Figure 30. Drag data were obtained over the center 30 cm of the airfoil span. Although the lowest chord Reynolds number studied was 1,000,000, the spanwise drag variation using this technique is significant. The spanwise flow structure increases in scale as the Reynolds number decreases and, thus, the maximum deviation from the mean in the measured drag increases.

In view of the large-scale vortices produced in the wake and the spanwise flow structure, the strain gauge balance method appears to be attractive if the side plate interference effect could be determined or eliminated.

4.1.1.1 Wind Tunnel and Force Balance

A large number of experiments have been performed in the non-return, low speed wind tunnels in the Aerospace Laboratory of the University of Notre Dame. These tunnels are capable of producing low turbulence intensities over the normal range of tunnel velocities, 9 to 28 m/sec (see Figure 31). The turbulence intensity which varies only slightly over this range has been found to be equal to or less than about 0.1%. Twelve anti-turbulence screens precede the contraction cone which has a square cross-section and a contraction ratio of 24:1. The test section, which is 610 mm square (24 in x 24 in) and 1828 mm (72 in) long, and diffuser are separated by a 101 mm wide section of foam rubber, used to minimize vibrations from the fan motor. The eight-bladed fan is driven by a 15 hp AC motor with a variable speed drive. The motor and fan assembly is mounted outside the laboratory in a protected structure isolated from the diffuser. The lower limit of the tunnel's velocity, normally 9 m/sec, can be extended to as low as 2.1 m/sec by the addition of one or two flow restrictors between the vibration insulation and the test section. The flow restrictors are made from ordinary plastic drinking straws 5 mm I.D. by 200 mm long, and also serve to damp out slight surges in tunnel velocity caused by outside wind gusts.

The test section used to obtain lift and drag force data had an externally mounted, two-component strain gauge balance with a dual flexure system for lift and drag. For low loads as small as 0.01 N (0.04 oz), a very sensitive flexure was engaged; a stiffer flexure was engaged at around 12.74 N (46 oz.). The model was mounted with the span vertical between the two square, smooth plates, 9.5 x 610 x 610 mm (3/8 x 24 x 24 in.), bolted to the inside of the test section so that the model and the sting "floated" between the plates as shown in Figure 32. The gaps between the model and the endplates were held as close to 0.51 mm (0.020 in.) as possible to minimize leakage of flow through them without risking contact between model and plate. The configuration thus approximated an airfoil aspect ratio of infinity. The model sting was shielded from the air flow by a streamlined covering. The angle of attack of the airfoil was changed with the tunnel running by means of an electric motor/gear arrangement. Changes in the angle of attack could be made to within ± 0.05 degrees.

To investigate the interaction between the boundary layer on the plastic plates and the ends of the airfoil model, the arrangement shown in Figure 33 was used. For this configuration, the airfoil model is made in three pieces with the top and bottom sections attached to the plates and the center section free to float. The center section is attached to the external balance with a sting which passes through a hole in the top piece of the model. The gaps between the center section of the model and the end sections were 0.51 mm (0.020 in.). To change angle of attack, the center section was rotated with the motor drive to the desired angle, after which the top and bottom sections were rotated manually and secured to the plates.

The signals from the strain gauge balance were sent directly into the strain gauge amplifier. The lift and drag amplifier gains were designed to be different due to the larger forces resulting from lift; thus, the drag gain was about five times greater than the lift gain. The signals were subsequently recorded on a strip chart recorder.

The NACA 663-018 and 5.64% thick EPPLER 61 airfoil geometries were used in these experiments, as shown in Figure 34. The airfoil models were made in the Aerospace Laboratory at the University of Notre Dame by machining the models out of aluminum and then making epoxy molds. Any number of identical models with a smooth, plastic-like finish can be cast using each mold. Three NACA 663-018 models were used, each having a chord of 250 mm and a span of 403 mm. One model was used as a full span force model (Figure 32), one was cut into three pieces with only the center 254 mm span attached to the force balance to check the side plate/airfoil interaction (Figure 33) and the third was instrumented with 98 static pressure taps.

*A discussion of the free stream disturbance level in the wind tunnel will be given in section 4.1.2.

Two smooth EPPLER 61 airfoil models were also used, each having a chord of 125 mm and a span of 380 mm. One of these models was milled from the aluminum model and was cut into three pieces to check the side plate/airfoil interaction. Only the center 274 mm section of the airfoil was attached to the force balance. Data from an earlier study⁶⁰ using a reinforced balsa wood EPPLER 61 model with a 250 mm chord and a 424 mm span was used for comparison purposes.

4.1.1.2 Pressure Measurement

An automated pressure measuring system was developed to improve the speed and accuracy of measuring pressures around an airfoil section. The system components included an Apple II plus mini-computer with four floppy disk drives, a printer, and a video monitor. Installed in the Apple II Plus were an Interactive Structures A113-12-bit analog to digital converter data acquisition system and a Mountain Computer I/D + O/A 8-bit input plus output system. Each of these A/D devices could accommodate 16 channels of input and the Mountain D/A could accommodate 16 channels of output. Two Setra Systems electronic manometers with analog output were used (Models 339R, calibrated from 0 to 14 mm water [0 to 0.55 in. water], and 339H, calibrated from 0 to 140 mm water [0 to 5.5 in. water]) to measure tunnel dynamic pressure from a pitot static tube, and to measure the pressure differences at each airfoil pressure port. Both electronic manometers used differential pressure transducers and had digital read-out to four significant figures. These devices had a listed accuracy of $\pm 0.14\%$ of full scale.

The pressure ports in the model surface were connected with tubing to junction switch wafers in three groups of 33 ports. The output of the wafers was connected to a Scanivalve body. A dummy transducer was installed in the body and the output connected to one of the electronic manometers. The standard solenoid controller was used for the Scanivalve, but the Mountain D/A output was used in conjunction with a transistor trigger circuit to switch and home the Scanivalve. The analog outputs of the electronic manometers were connected to two channels of the Interactive Structures A113 unit to measure the $(P_i - P_\infty)$ at each port on the model minus the free stream static pressure and, simultaneously, the free-stream dynamic pressure (Q_∞) .

The pressure tap model had ports situated on the leading edge and near the trailing edge, with 46 ports on both surfaces along the chord. Four extra ports were placed spanwise on the model at one chordwise location, giving a total of five ports spaced across the span for two-dimensional flow checks. The port tubing was first connected to the wafers which reduced the number of tubes so that the Scanivalve could be used. The Scanivalve was then connected to the electronic manometer so that all the airfoil ports could be easily accessible. The pitot static tube, mounted ahead of the upper side plate, was connected across the second manometer; the static pressure line was also connected to the manometer for port pressure to provide ΔP .

A computer program was written in the Apple Basic language. This program homes the Scanivalve to its first port and then waits until the operator sets the angle of attack, tunnel dynamic pressure Q , and the wafers to the correct position. When ready, the computer takes 200 samples of each manometer voltage over a period of about 10 seconds, averages them to get a mean, converts the voltages to inches of water using the manometer calibration constant, and computes the pressure coefficient $C_p = (P_i - P_\infty)/Q$ at each port. After sampling through the first 33 ports, the program enters a wait until the operator switches the wafers to the next set of ports. This procedure continues similarly for the last 32 ports which completes the run. The computed C_p values and other pertinent test information such as the date of test, average Q , angle of attack, atmospheric pressure, and temperature are then sent to the printer for a hard copy.

4.1.1.3 Discussion of Results

Force data obtained from the strain gauge balance are presented for the NACA 663-018 and the EPPLER 61 airfoils. Drag force data obtained by integrating the static pressure distributions for the NACA 663-018 airfoil are also presented. All force data are corrected for solid body blocking, wake blocking, streamline curvature, and longitudinal buoyancy according to the methods described by Rogers¹³⁰. The applicability of these standard corrections was demonstrated in Reference 60 where two different sized airfoils produced almost identical corrected values of the c_L and c_D at $Re = 87,000$.

Lift and drag data for the NACA 663-018 airfoil were obtained from the strain gauge balance for $61,000 < Re < 300,000$. The results for $Re = 61,000$ and $300,000$ are shown in Figures 35 and 36 respectively. Data are shown on each of these figures for the one piece airfoil model and for the three piece airfoil model. The difference in the drag coefficient obtained from the two models is attributed to the elimination of most of the airfoil/end plate interaction for the three piece model. A smaller and less consistent difference is noticeable for the lift coefficient over this Reynolds number range. A comparison of the minimum drag coefficient for this airfoil with the one piece and three piece models is shown in Figure 37. The uncertainty in these data as obtained by the method of Kline and McClintock¹³¹ is also shown. The determination of the uncertainty of single-sample measurements is particularly important in this problem because of the difficulties in the measurement and because the true drag force is not known. The difference between the c_{dmin} measured for the two models below about $Re = 80,000$ is overshadowed by the uncertainty* in the measurements. As Re increases to about $80,000$ the trend becomes clear. The difference in c_{dmin} at $Re = 60,000$ is about 15% and decreases to about 10% at $Re = 300,000$. Studies using a circular cylinder and this same balance⁶⁰ produced drag coefficients which were 10% higher than other published data. Figure 37 also contains four data points which were obtained by integrating static pressure distributions. A typical static pressure distribution is shown in Figure 38. At this Reynolds number (90,000) the minimum drag occurred at an angle of attack of 7° . Since the pressure distributions do not contain end plate effects and since pressure drag is the predominate source of drag it is not surprising that these points fall close to and slightly lower than the three piece model data.

*Uncertainty in force balance data has subsequently been reduced by a factor of two by using the Apple II data acquisition system.

The EPPLER 61 airfoil has been studied extensively at low Reynolds numbers. Lift and drag data from the strain gauge balance and smoke visualization data have been presented in Reference 60. The use of the standard tunnel corrections was verified using 25 cm and a 12.5 cm chord models. The reproducibility of this type of data was verified for the one piece model⁶⁰. Experiments were performed to evaluate the airfoil/endplate interaction using one piece and three piece airfoil models in the chord Reynolds number range from 36,000 to 60,000. The results of these experiments, including the uncertainties, were similar to the results for the NACA 663-018 airfoils. The minimum drag coefficient was found to be about 16% lower for the three piece model as compared to the one piece model.

The EPPLER 61 data obtained at the Delft¹³² and Stuttgart¹³³ Universities are compared with data obtained at Notre Dame in figure 39 for $R_c = 80,000$. The Delft and Stuttgart data show slightly higher C_{gmax} values and what appear to be an earlier stall as angle of attack increases. The greatest difference in these data sets is in the C_{dmax} coefficient where the Delft and Stuttgart results are as much as 50% lower than those obtained at Notre Dame. The one piece airfoil model used in the Notre Dame force balance was affected by the endplate boundary layer interaction. Eliminating this airfoil/endplate effect, as shown above, only reduces the minimum drag coefficient about 16%. Why are the Delft and Stuttgart drag data which were obtained with a wake traverse, still about 41% lower? The difficulties in making wake pressure measurements in an unsteady flow with constantly changing flow direction probably accounts for some of this difference since the experiments of Delft and Stuttgart use the wake rake to determine drag. In addition, the spanwise position of the wake traverse may account for another part of this difference. Since the true value of the drag is not known, further studies will be necessary to completely resolve this problem. It is clear that all measurements at low Reynolds numbers should be approached with these problems in mind.

4.1.2 Influence of Free Stream Disturbances

The disturbance environment present in the test section of a low speed wind tunnel is usually determined by free stream turbulence (velocity fluctuations), acoustic phenomena (pressure fluctuations) and mechanical vibrations. The free stream turbulence level depends on the history of the flow in the settling chamber, flow straighteners or screens and the inlet leading to the test section. Acoustic phenomena are related to the noise emitted from turbulent boundary layers on the side walls, unsteady separated flow regions, and the fan and its associated drive system. Mechanical vibrations may be caused by rigid coupling of the fan and drive system to the wind tunnel as well as by the unsteady wakes of probe and model supports. Although these factors which determine the disturbance environment may be reduced and controlled, they cannot be completely eliminated. It is apparent that, in general, each wind tunnel has a different disturbance environment which is a function of its design and method of fabrication. Because airfoil boundary layers are sensitive to small disturbances, accurate wind tunnel models are very important in the evaluation of a given design. Furthermore, because the forces, pressure differences and velocities are small, a great deal of care must be exercised to obtain accurate and meaningful data. It is not surprising, therefore, that similar experiments on the same geometry model at low Reynolds numbers often produce results which differ from one wind tunnel to the next.

4.1.2.1 Experimental Apparatus and Procedure

This research was conducted in the Aerospace Laboratory of the University of Notre Dame. The equipment used consisted of a wind tunnel and a strain gauge balance with its associated electronics for lift and drag measurements, electronic manometers, and a micro-computer system as described earlier. The uncertainty of the earlier lift/drag measurements was reduced by half by using the Apple II data acquisition system instead of the strip chart recorder. A hot-wire anemometer and sound pressure level analyzer were used to analyze the test section environment. The flow visualization studies utilized the smoke tube method, strobe lights, and photographic equipment described by Mueller¹³⁴. The airfoil sections used for these studies were the Lissaman 7769 profile described by Lissaman¹³⁵ and Burke²¹ and the Miley M06-13-128 profile¹³⁶. Both of these airfoil sections were designed for a chord Reynolds number of approximately 600,000, the Lissaman for the Gossamer, Condor and Albatross man-powered aircraft and the Miley for the inboard portion of a helicopter rotor. These two airfoils performed according to their designs near $R_c = 600,000$. The geometries of these airfoil sections are shown in Figure 40.

The Lissaman 7769 airfoil model used in the experiments was constructed of wood using two steel end plates machined to the profile of the airfoil. The wood was coated with an epoxy and finished to give a smooth surface. The airfoil model had a 437 mm span and a 249 mm chord. Experiments were also performed using two Miley airfoil models cast from the same mold. These smooth epoxy models each had a chord of 250 mm and a span of 421 mm. One model was used as a force model as well as for flow visualization and hot-wire experiments. The other model, cast with 90 static pressure taps, was used for pressure measurements.

A hot-wire anemometer system was used to determine mean tunnel velocities and turbulence intensities in the test section under varying test conditions. All hot wire measurements were made with a DISA Type 55P11 hot-wire probe, having a sensing element 5 microns in diameter and 1.5 mm long. The hot-wire anemometer system consisted of the DISA 55M10 constant-temperature anemometer which could be tuned to respond to frequencies up to 50,000 Hz with a hot-wire temperature between 250°C and 300°C. A DISA 55D10 linearizer was used and adjusted so that the voltage output of the anemometer corresponded directly to the tunnel speed. Previous studies conducted at the Notre Dame Aerospace Laboratory by Kegelman¹³⁷ showed that the linearizer produced a small amount of electronic noise which became a significant part of the total turbulent signal at turbulence intensities below 0.1%. The output of the linearizer was monitored on a Data Precision Corporation V-45 Digital voltmeter to obtain tunnel velocities. Simultaneously, the output signal was filtered using a 1 Hz high pass filter and the remaining AC component was amplified to produce a useful voltage on a T.S.I. Model 1076 true RMS meter, which (knowing the amplification) yielded the root-mean-square turbulence intensity, $u_{rms} \times 100/U$. When taking data for frequency analysis, the DISA linearizer was bypassed in order to eliminate any 60 cycle noise from the frequency spectrum. All analog voltage outputs were sampled using the A/D capabilities of the Apple II micro-computer and associated software developed specifically for these experiments.

Sound pressure level measurements were accomplished through the use of a Bruel and Kjaer Frequency Analyzer, type 2107. The type 2107 is an AC operated audio frequency analyzer of the constant percentage bandwidth type. Although designed as a narrow band sound and vibration analyzer, it may be used for any kind of frequency analysis within the range of 20-20,000 Hz. The frequency analyzer was combined with a Bruel and Kjaer Level Recorder Type 2305, allowing frequency amplitude diagrams to be recorded automatically on pre-printed frequency-calibrated paper. The Selective Amplifier Section of the sound pressure level equipment was used as a narrow-band analyzer which could be continuously varied from 20 to 20,000 Hz. The octave selectivity was set at 45 decibels to produce the narrowest possible bandwidth of approximately 1/3 octave. Two different condenser microphones were used in the analysis. All of the testing was accomplished with the use of a Bruel & Kjaer Nose Cone UA0386 designed to reduce the aerodynamically induced noise present when the microphones are exposed to high wind speeds. The nose cones were designed to replace the normal protection grid of the microphone cartridge and were of a highly streamlined shape with a highly polished surface. A fine wire mesh around the circumference of the cone allowed sound waves to penetrate to the microphone diaphragm. As most of the tunnel noise was propagated upstream from the fan blade the directional characteristics of the microphone were an important consideration. Bruel and Kjaer¹³⁸ describe the omnidirectional characteristics of the microphone when the nose cone is used. Any body regardless of how streamlined produces some aerodynamically induced noise. For the purposes of this study it was assumed that the aerodynamic noise produced by the microphone with its nose cone would not exceed the aerodynamic noise produced by any similarly streamlined body and the results should thus give a reasonable indication of the acoustic environment.

All measurements were made in the South Tunnel at the University of Notre Dame Aerospace Laboratory. The force balance was used to collect lift and drag data on the Lissaman airfoil over an angle of attack range from -21° to 25° . The tunnel was always started with the airfoil at 0° angle of attack. All data were corrected utilizing the AGARD methods described earlier¹³⁰. Once the tunnel was on, the angle of attack was changed to -20° and the experiment was conducted increasing the angle of attack to $+25^{\circ}$ then decreasing it back to 0° . During the entire test the tunnel was left running. At each angle of attack the microcomputer sampled the lift, drag, and the dynamic pressure simultaneously over a 5 second period taking 100 samples to be averaged. Zero lift and drag voltages were measured just prior and immediately after the experiment to account for any amplifier drift. The data was corrected for this drift based on an assumed linear drift during the period of the experiment. Calibration of the force balance was checked every fourth test. The force/voltage calibration remained constant over long periods of time.

Both the hot-wire and sound level measurements (68 cm downstream from the entrance to the test section) were taken at a location 8 cm ahead of the leading edge of the airfoil. For convenience the model was removed when free-stream measurements were made. Figure 41 shows the experimental set-up, including the location of the flow-restrictor and the turbulence screen.

Previous studies by Jansen⁶² and Kegelman¹³⁷ have shown that free-stream turbulence and sound levels at a given streamwise location are invariant across the test section except at locations near the wall. In this study the probes were centered in the test section between the side-plates at a height comparable with the location of the leading edge of the airfoil model.

Measurements were made over a velocity range of 2.5 to 31 m/s with different combinations of the turbulence screen and flow restrictors. The hot-wire anemometer was used to monitor free-stream velocity, measure free-stream turbulence intensities, and determine frequency content of the turbulent velocity fluctuations. Frequency spectra were obtained by sampling the hot-wire anemometer signal, acquiring 1024 samples at a specified sampling rate. The sampling rate could be selected to increase the frequency resolution at low frequencies or to increase the overall frequency range capability. Two frequency spectra were taken at each testing point, one over a range of 0 to 500 Hz with a resolution of 0.98 Hz and the other over a range of 0 to 5000 Hz with a resolution of 9.8 Hz.

The Bruel and Kjaer frequency analyzer was used to determine total sound pressure levels in the test section. Calibration of the frequency analyzer was accomplished with a 124 decibel B&K pistonphone prior to testing. The pistonphone produced a constant 124 decibel sound level with a primary frequency of 250 Hz. Microphone calibration was checked periodically and no drift was observed. The frequency content of the sound field was documented by making filtered measurements of the sound level from 20 to 20,000 Hz using the selective amplifier as a narrow-band analyzer. Frequency content of the sound field was also obtained by sampling the microphone output directly and performing the same analysis as described for the hot-wire signal. A comparison of the two methods shows an excellent correlation.

Finally, to analyze the data it was necessary to know the frequency of the fan blade passage. This was obtained for each velocity and test condition by marking a single fan blade with a piece of tape and using a hand-held strobe to determine the fan blade rpm.

4.1.2.2 Disturbance Environment - no Airfoil Present

Results of the acoustic and turbulence measurements showed that the experimental environment was a complex function of many variables. Measurements were made to take into account as many of these variables as was possible³⁷. Figures 42 and 43 present the freestream turbulence intensities and sound pressure levels over the entire range of velocities. In the velocity range from 9 to 31 m/s no flow restrictors were used. The turbulence intensity varies from 0.07% to 0.15% in this range. Turbulence intensities as low as 0.05% were calculated using analytical techniques to reduce the hot-wire data. In using the linearizer to measure turbulence intensities electronic noise was introduced which increased the measurements slightly. Therefore actual turbulence intensities may be slightly lower than those presented here. Turbulence intensities determined analytically compared favorably with those from the linearizer for values greater than 0.15% since the electronic noise was no longer a significant addition to the turbulent signal.

There was a noticeable increase in turbulence intensity at a velocity of 12 m/s. This corresponds to a fan rpm of approximately 460. At this fan rpm there was a marked pulsating of the fan blades as the belt-drive from the motor appeared to slip at this setting. The pulsating of the fan was accompanied by a slight squeaking of the belts. When a flow restrictor was introduced the turbulence intensities in the section were increased significantly. The turbulence intensity at idle speed (i.e., 298 rpm) increased from 0.07% to 0.16% when one or two flow restrictors were used (Figure 42). With one flow restrictor a large increase in turbulence was observed at 5.5 m/s while an even larger increase was observed at 3.8 m/s when two flow restrictors were in place. Both of these velocities corresponded to a fan rpm of about 460. It may be the increased work load in conjunction with the pulsating tendency of the fan at this rpm which causes the fan to induce these high turbulence intensities in the test section. The u_{rms} remains essentially the same and the decrease in U causes the ratio of u_{rms}/U to increase. Once the 460 rpm region is passed the turbulence intensities gradually decreased but always remain higher than the no flow restrictor case. An important comparison can be made at 9 m/s (a chord Reynolds number of approximately 150,000 for the Lissaman Airfoil) where the tunnel may be operated with no flow restrictor or with one flow restrictor in place. The turbulence intensity increases from 0.07% to 0.16% when one flow restrictor was added after the test section as shown in Figure 42.

Analysis of the sound pressure levels in the test section indicated a different behavior. Sound levels at idle remained constant at approximately 93 dB (referred to 2×10^{-5} N/m²) regardless of the experimental set-up (Figure 43). Introduction of flow restrictors or a turbulence screen did not appear to change the total sound pressure level in the test section for a given fan rpm. However, to achieve the same test section velocity with one flow restrictor in place the fan had to be operated at a higher rpm. When operating at a chord Reynolds number of 150,000 with one flow restrictor in place, a total sound level of 104 dB was measured in the section compared to a much quieter 93 dB at the same velocity with no flow restrictor in use. Special care was taken to visually observe the probes for mechanical vibrations which may have been produced by tunnel vibrations or the flow over the probe holders. The foam insulation between the test section and tunnel diffuser successfully damps any mechanical vibrations from the fan motor since no significant vibration of either the hot-wire or microphone probes was observed.

Introduction of a turbulence screen between the test section and tunnel inlet increases the turbulence intensity in the test section. Figure 42 shows the turbulence intensities produced by a single turbulence screen with 7.09 meshes/cm both with and without one flow restrictor in place. The lowest set of points represent the case with no turbulence screens (i.e., the standard wind tunnel configuration). At very low speeds with both the screen and one flow restrictor in place, the screen did not induce turbulence intensities much higher than those present due to the flow restrictor alone. As the speed increased, the turbulence intensity increased significantly. Turbulence intensities produced by the turbulence screen with the flow restrictor in place were larger than turbulence intensities produced with the turbulence screen alone over the same velocity range. This suggests that the total turbulence intensity may be due to a coupling of the velocity and acoustic fields.

Total turbulence intensity and sound pressure levels reveal many important facts about the test section environment. In order to determine the source of the acoustic and turbulent phenomena in the test section, an analysis of their frequency spectra is required. In addition, it is well known that the presence of characteristic frequencies in the freestream can affect the transition of a laminar boundary layer and thereby radically change the results of the experiment.

The frequency spectra presented here correspond to a chord Reynolds number of 150,000 for the Lissaman Airfoil (approximately 9 m/s). Frequency analysis was conducted with both the sound pressure level equipment and the hot-wire anemometer. Figures 44 and 45 present frequency spectra at $R_c = 150,000$ for the standard wind tunnel configuration from the sound and hot-wire analyses respectively. In these figures, as well as Figures 46 through 47, the frequency spectra presented were normalized with respect to the maximum value for the case considered. Both the sound and hot-wire equipment picked up the fan blade passage frequency of 42 Hz. This frequency was a major part of the acoustic signal. While still significant in the turbulent signal, it can be seen that lower frequencies add a substantial amount of turbulence in addition to the fan blade passage. These lower frequencies may include a slight pulsating of the fan. Some harmonics of the primary frequency can be seen in both the hot-wire and acoustic signals. Figures 46 and 47 are frequency spectra taken at the same tunnel velocity with one flow restrictor in place. The fan blade passage frequency has increased to about 100 Hz as the fan operates at a higher speed to compensate for the pressure loss through the flow restrictor. A lower frequency of 25 Hz has also appeared. This frequency is twice the fan rpm and becomes prevalent due to the slight pulsating of the fan under the increased work load. Under these test conditions the acoustic phenomena have become a larger part of the turbulent signal. The frequencies associated with the fan blade passage become the primary frequencies of the turbulent signal as seen in Figure 47. The lower frequencies are still present but are of the same or lower magnitude as the fan blade frequencies.

Thus, part of the increase in turbulence intensity resulting from the introduction of a flow restrictor is apparently due to an increase in sound pressure level. Characteristic frequencies in the freestream at a given velocity (i.e. Reynolds number) will also vary depending on whether a flow restrictor is used.

Finally, with the introduction of a turbulence screen with 7.09 meshes/cm in the flow, the frequency spectrum becomes broadband with no characteristic frequencies for both the flow restrictor and no flow restrictor cases (Figures 48 and 49). The turbulence levels introduced by the screens are much higher than the free-stream disturbances caused by the fan blade passage or any pulsating of the fan. For the $R_c = 150,000$ case the turbulence resulting from the introduction of the screen dominated the test section environment. This does not mean the acoustic effects are absent but only that the order of this disturbance is much lower than that produced by the turbulence screen.

A better understanding of the conditions present in the test section when flow restrictors were introduced to reduce the test velocity has been obtained. The purpose of introducing the flow restrictor into the test section was to reduce the Reynolds number of the test. It was found that some of the earlier results attributed to lower Reynolds numbers may instead be due to the higher turbulence intensities in the test section. An understanding of the small changes in a test environment is critical at these low Reynolds numbers. With the introduction of flow restrictors in the test section turbulence intensities increased significantly. A part of this increase could be caused by the sound pressure waves transmitted upstream from the fan blade passage. The increase in turbulence intensity at a fan rpm of 160 was much larger than at any other speed. A combination of increased work load due to the pressure drop through the flow restrictor along with a slight misadjustment of the drive belts caused pulsating of the fan blade and subsequent increase in turbulence. The increase in turbulence produced by the flow restrictors had very characteristic frequencies. These frequencies varied depending on test conditions. The fan rpm required to achieve a certain test section velocity was dependent on the atmospheric conditions. The fan rpm also varied with the outdoor wind velocity which impinged on the fan. Another factor which was found to effect fan rpm was small changes in lab pressure caused by long periods of testing at high speeds. As the Notre Dame tunnels are of the indraft, nonreturn type, the aerospace laboratory cannot be air tight. However, high speed testing lowered the lab pressure enough to require increased fan rpm to maintain a constant velocity. This effect was especially noticeable with flow restrictors in place.

In contrast to the increase in turbulence intensity produced by the flow restrictors, turbulence increases due to the introduction of a turbulence screen had no characteristic frequencies in the range studied and the intensities were relatively constant over the complete range of velocities. Turbulence produced by the turbulence screen dominated over that produced by the flow restrictor when they were used in combination with the latter except in the case of very low velocities. With the knowledge of these experimental conditions a better understanding of data taken at low Reynolds numbers can be obtained. Further research into the freestream turbulence phenomenon has provided additional insights into the character and source of the "turbulence" as measured in the above studies. The installation of improved facilities, most significantly, a DEC PDP-11/23 computer based data acquisition system, has enabled the refinement of measurements and data reduction schemes of similar experiments conducted in the University of Notre Dame low speed wind tunnels.

As stated earlier, hot-wire experiments have been conducted to determine the level of freestream turbulence in the testing environment. Test runs in which 1024 samples were obtained were reduced to determine turbulence levels and frequency spectra. It was observed that a significant portion of the energy is tied up in the lower frequencies as indicated by the hot-wire data. Expansion of the sample lengths to 2048 points and the introduction of ensemble averaging has permitted more representative results to be produced. Specifically, there are strong indications that for the in-draft, non-return wind-tunnels, an atmospheric/tunnel drive chain couple exists which tends to bias the calculated turbulence intensities in a random fashion. However, through the use of appropriate filtering techniques, this bias can be significantly reduced and repeatable results obtained. It appears that for the low-speed Notre Dame wind tunnels, turbulence intensities equal to or below 0.1% are consistently obtained when a high-pass filter of 10 Hz is utilized. Energy in the frequencies below this value are most likely due to atmospheric fluctuations and fan motor loading response to those changes rather than to tunnel construction or design. Further, this energy is several orders of magnitude larger than that associated with frequencies of greater than 10 Hz. Thus, it is apparent that these low frequency phenomena do not contribute to freestream turbulence as it is known in the general sense and so should not be allowed to influence evaluations of the wind tunnel turbulence level. However, it is entirely appropriate that when quoting the freestream turbulence level for a specific wind tunnel, the investigators should indicate the frequency cutoff used in its determination. Accordingly, efforts can then concentrate on isolating the effects of the predominate frequencies in the resulting range on more general experimental studies.

4.1.2.3 Airfoil Performance

The lift and drag performance of the smooth Lissaman airfoil in the standard wind tunnel configuration (i.e., no screen or flow restrictors, see Figure 31) is shown in Figure 50. As the angle of attack was increased, smoke visualization indicated that at 6° the laminar boundary layer separated on the upper surface at about 25% chord while at 8° the boundary layer appeared to be undergoing transition and separated from the upper surface at about 35% chord. At an angle of attack of 10° transition appeared to be complete and the boundary layer remained attached until about the 70% chord location. There is a noticeable change in the lift curve slope associated with the extension of attached turbulent flow. A smoke photograph at $\alpha = 12^\circ$ is shown in Figure 51a. The lift coefficient continues to increase in this region, Figure 50, until it reaches a maximum value of 1.3 at 16° . Further increases in angle of attack cause the location of turbulent separation near the trailing edge to move upstream (and c_L to decrease slightly) until it reaches about 35% chord where a jump takes place to a laminar separation at the leading edge at about 19° . At this point there is an abrupt decrease in c_L from 1.25 to about 0.9. As the angle of attack is decreased from 25° , the boundary layer separates in the laminar state and the c_L remains about 0.9 until an angle of 11° is reached. With little or no free stream turbulence present the flow transitions shortly after separation. A comparison of the airfoil flow field at $\alpha = 12^\circ$ for both increasing and decreasing angle of attack is shown in Figure 51. The lift jumps up at $\alpha = 10^\circ$ as a result of the fact that transition in the separated shear layer allows the flow to reattach. The accompanying variations in the profile drag coefficient is shown in Figure 50. The abrupt decrease in c_L is accompanied by an abrupt increase in c_D . Therefore in the lowest turbulence, quietest wind tunnel configuration, a significant clockwise or high $c_{D,max}$ hysteresis region in the lift and drag forces was found. The presence and extent of this hysteresis was determined by the location of separation and/or transition in the boundary layer. The location of transition from laminar to turbulent flow in the boundary layer has been known for a long time³⁶ to be affected by the level and type of free stream disturbances.

In earlier experiments by Conigliaro¹³⁹ using this airfoil, hysteresis was not found. This data was taken by increasing the angle of attack from -10° to $+20^\circ$ and then turning the tunnel off for the balance calibration. The airfoil was then returned to -10° angle of attack for the next experiment. In the present investigation no attempt was made to determine whether or not hysteresis occurred at negative angles of attack.

The result of changing the acoustical environment by adding one flow restrictor at the end of the test section is shown in Figure 52. As discussed earlier, the addition of one restrictor increases both the free stream turbulence level and the sound pressure level for a fixed value of tunnel velocity. This test section environment reduced the size of the hysteresis region and produced a slightly higher c_{max} of almost 1.4. A slightly lower minimum drag coefficient was also obtained. The use of two flow restrictors produced similar results with the hysteresis being almost completely eliminated. The increase in free stream turbulence and acoustic excitation caused the laminar shear layer to transition much earlier, thus allowing the flow to reattach sooner.

Increasing the free stream turbulence level to about 0.3%, by adding one 7.09 meshes/cm screen at the upstream end of the test section with no flow restrictor, produced the lift and drag coefficients presented in Figure 53. This test section environment completely eliminated the hysteresis region and yielded values of c_{max} and c_{min} between those of Figures 50 and 52. With a larger turbulence intensity in the test section, the airfoil boundary layer transitions very close to the leading edge, eliminating hysteresis by enabling the flow to reattach at higher angles of attack. The abrupt decrease in c_l occurred at approximately the same angle of attack in each case. The very large adverse pressure gradient at this angle of attack (i.e. 19°) caused the boundary layer to separate whether it was laminar or turbulent. Hysteresis occurred because the laminar separated shear layer did not reattach. An increase in turbulence did not prevent the abrupt loss of lift, but the separated flow was turbulent allowing more rapid reattachment.

When the chord Reynolds number was increased to 200,000 the hysteresis region was reduced when using the standard wind tunnel configuration. At this condition the abrupt decrease in lift occurred at about 19° for increasing angle of attack and the lift jumped up when the angle of attack was decreased to 16° . At a chord Reynolds number of 300,000 the lift decreased abruptly at about 21° and jumped back up at about 20° .

Free-stream disturbances are a major source of disparity in experimental data. However, there are other sources of disparity which produce results similar to those produced by free-stream turbulence. Figures 54 shows the lift and drag curves produced in the standard wind tunnel environment with a strip of tape 2.5 mm wide and 0.15 mm thick placed near the leading edge (i.e. across the span at 1.1% chord) of the airfoil. This small boundary layer roughness or trip reduced the hysteresis in a similar manner to the introduction of a flow restrictor. The tape produces similar results by tripping the boundary layer and causing early transition. A model with a small amount of surface roughness or irregularities in the surface caused by fabrication defects could produce the same results. The effect of surface roughness warrants further study and will be addressed later.

The section lift coefficient and section drag coefficient versus angle of attack for the Miley airfoil¹⁴⁰ for $R_c = 150,000$ and $R_c = 200,000$ are shown in Figures 55 and 56 respectively. The lift coefficient is zero at an angle of attack of about -3° for all of the Reynolds numbers studied. At a chord Reynolds number of 150,000 there is significant hysteresis in the lift and drag forces. The smoke visualization photographs shown in Figure 57 for $R_c = 150,000$ are helpful in understanding how the hysteresis is produced in these experiments. At an angle of attack of zero degrees, Figure 57a, the boundary layer separates near the maximum thickness location on the upper surface while a separation bubble near the leading edge on the lower surface appears to trip the flow on this side. There is no radical change in the observed behavior of the upper and lower surface boundary layers as the angle of attack increases to about 9° . There is, however, some upstream movement of the separation point and the pressure distribution is altered to produce greater lift, etc. The hysteresis region occurs between angles of attack of about 10° and 17° . Increasing the angle of attack to 13° (Figure 57c), and then to 15° (Figure 57d) moves the laminar separation point toward the leading edge with very little change in lift and a continuous increase in drag. At about 17° , the lift increases dramatically while the drag decreases. After this jump the lift drops off gradually while the drag increases. Decreasing the angle of attack from about 20° produces a much larger lift and lower drag from 17° to 10° . The reason for this is evident in the smoke visualization photographs taken at 15° and 13° when the angle of attack was decreased (e.g., see Figure 57f). For these cases transition appears to take place downstream of the maximum thickness, allowing the upper surface boundary layer to remain attached almost to the trailing edge. Thus the airfoil boundary layer has an entirely different character when the angle of attack is increasing toward about 20° than when it is decreasing from about 20° .

For chord Reynolds numbers of 200,000 and higher (i.e., Figure 56) no hysteresis is present and this smooth airfoil performs as expected. It is clear from these figures that operating the Miley airfoil, which was designed for $R_c = 600,000$ at lower Reynolds numbers severely degrades its performance and produces a hysteresis loop which acts in the opposite sense as the loop produced by the Lissaman airfoil.

Although the hysteresis loop for $R_c = 100,000$ and lower was documented and verified with static pressure measurements¹⁴⁰, the surface roughness due to the very small static pressure taps in the pressure model was enough to eliminate hysteresis at $R_c = 150,000$. For this reason the influence of disturbance environment was also studied for the Miley airfoil. The addition of one flow restrictor increased the free stream turbulence level from 0.07% to 0.16% while the introduction of one 7.09 meshes/cm screen upstream of the model raised the free stream turbulence from 0.07% to about 0.30%. A strip of tape 0.127 mm thick and 2.21 mm wide was placed on the airfoil with the leading edge of the tape at 0.013c. The results indicate that the hysteresis loop is not observed. The C_{max} remained the same for all configurations at $R_c = 150,000$. It was found that any increase in the disturbance environment eliminated the hysteresis loop at $R_c = 150,000$.

The importance of this hysteresis phenomena cannot be overemphasized. Low Reynolds number airfoil data obtained in noisy and/or high turbulence wind tunnels may not exhibit significant hysteresis. Therefore, aircraft designed using such wind tunnel data may not perform as expected in flight where the free stream disturbance level is often very low.

4.1.2.4 Remarks

The problems associated with obtaining accurate wind tunnel data for airfoil sections at low Reynolds numbers are compounded by the extreme sensitivity of the boundary layers to the free stream disturbance environment. The effect of free stream disturbances varies with magnitude, frequency content, and source of the disturbance. The sensitivity and accuracy of the measurement and data acquisition systems as well as the experimental procedure used can have a substantial effect on the results obtained.

Although free-stream disturbances produced the largest disparity between different tests for the Lissaman and Miley airfoils, not all of the differences can be attributed to free-stream disturbances. Model imperfections or surface roughness can produce results identical to those achieved with free stream disturbances. Reynolds number effects are critical at low speeds. An increase in Reynolds number from 150,000 to 200,000 for the Lissaman airfoil will eliminate a major portion of the hysteresis, and the hysteresis is insignificant at 300,000. For the Miley airfoil an increase in chord Reynolds number from 150,000 to 200,000 completely eliminates hysteresis. It is important that the free-stream disturbances be well documented for each test condition in order to correctly attribute differences in test results to these free stream disturbances. In accordance with new techniques and equipment, such disturbances in the Notre Dame tunnels continue to be investigated and recorded. A clear distinction between the effects of free-stream disturbances, model irregularities, and Reynolds number must be made before the performance of airfoils at low Reynolds numbers can be clearly understood.

4.1.3 The Influence of Surface Roughness

As mentioned earlier the effects of roughness on the performance of airfoils operating in the low Reynolds number regime can be quite significant. However, to date there has been no systematic study dealing with this problem and most data that does exist has only been gathered as part of general evaluations of the performance of particular airfoils^{1,35,37,43,59}. That no emphasis has been placed on investigating the effects of roughness in this area is not surprising when one considers that a basic understanding of the influence of roughness on boundary layer development, stability, and transition is as yet undeveloped.

References 141 thru 146 present a small overview of some of the more fundamental investigations into roughness effects on boundary-layer behavior. Unfortunately, most work has dealt with flat plates or pipe flow with little attention given to pressure gradients over a curved surface. Tanj^{141,145} has done much to illuminate the complexities of experimental studies into roughness and in identifying the important parameters. Klebanoff and Tidstrom¹⁴⁶ have also contributed much in this area including demonstrating the usefulness of applying stability theory to problems in this field.

Experimental data concerning the effect of roughness on airfoil performance has been gathered at the University of Notre Dame and elsewhere¹⁴⁷⁻¹⁵³. Unlike the situation at higher Reynolds numbers, surface roughness can have quite beneficial effects on the performance of airfoils at lower Reynolds numbers, although this is by no means always the case. Typically, roughness is used to overcome the adverse effects of laminar separation by inducing transition to a turbulent flow which remains attached to the airfoil surface. Pohlen and Mueller observed elimination of the hysteresis region for the Miley M06-13-128 airfoil at $R_c = 150,000$, through the use of a tape strip⁴⁰. In contrast, Payne and Nelson recorded severe losses in the performance of the NACA 0018 when at the same Reynolds number and roughened with grit¹⁴⁷. Carmichael discusses data gathered at Stuttgart which shows the effect of two-dimensional tripping strips on performance parameters for a variety of airfoils. While some of the airfoils studied showed performance degradation, others demonstrated remarkable improvements.

Recent studies at the University of Notre Dame on the Wortmann FX 63-137 airfoil have underscored some of the complexities of roughness studies in the low Reynolds number regime¹⁵⁴. The models used had chord lengths of 152.4 mm (6 in) and spans of 412.75 mm (16.25 in). Tests conducted at a Reynolds number of 100,000 have shown that roughness type, size, and location can each have a significant effect on airfoil behavior. However, as is the case with many other facets of low Reynolds number testing, problems exist with the investigative techniques themselves which must be considered. As an example, Figures 58 and 59 are presented which show wide differences in pressure distribution measurements for two models of the same airfoil at the same test conditions. One model was constructed with pressure taps staggered so as to place each succeeding one outside any turbulent wedge that might exist behind any previous tap. The other model has taps placed one behind the other in the chordwise direction. As seen in Figure 59, the "in-line" tap model fails to indicate the separation bubble which exists on the FX 63-137 at 16° angle of attack and a R_c of 200,000. Evidently, the taps of this model act in a similar fashion to surface roughness by causing transition at a more forward location than would have been the case had a bubble formed and tripped the flow further aft.

Additional pressure plots shown in Figures 60 and 61 demonstrate the effect of surface grit on the pressure distribution of the FX 63-137 at 16° and $R_c = 100,000$ (k is the height of the grit and w is the width of the grit band). As seen here, grit of sufficient height can cause stall at this angle in contrast to the clean airfoil which exhibits stall at 19° . Furthermore, even for the smallest grit size shown, transition is moved forward from the 0.18c location seen on the smooth airfoil to approximately 0.09c on the roughened model.

In the course of these studies, the Notre Dame force balance was improved by the addition of a moment-measuring capability which utilized strain gages. Figures 62 and 63 provide force balance data for the FX 63-137 in the clean and roughened configurations. In the latter case, a strip of tape composed of several layers of tape was notched to produce a zig-zag pattern and was placed across the upper airfoil surface at $x/c = 0.01$. In this comparison, C_{Lmax} is significantly decreased and C_{Dmin} slightly increased. However $(x/d)_{max}$ is increased by over 7% although it occurs at 6° instead of the 8° observed for the case of the smooth airfoil. Differences in the variation of quarter chord moment coefficient with angle of attack can also be seen. The angle of attack region of hysteresis is reduced to just two degrees whereas for the smooth airfoil it occurred across four degrees.

Given the complexity of the low Reynolds number problem, it does not appear that general solutions for the prediction of airfoil performance under roughened conditions will be available for some time. Instead, a more basic understanding of the influence of roughness on boundary-layer behavior will have to be developed. Until such an understanding is obtained, the design engineer working in the field of low Reynolds number airfoils will have to depend on wind tunnel results of the type discussed above.

4.1.4 Finite Wing Experiments

In order to design a practical low Reynolds number vehicle, it is necessary to evaluate the importance of three-dimensional boundary layer effects on a finite wing. Many of these vehicles require large aspect ratio wings; however, the largest aspect ratio allowable in most wind tunnels, using a reasonable chord dimension, is usually much smaller than the actual vehicle. These small aspect ratio wing experiments can, nevertheless, illuminate the major problems with the finite wing.

Studies have been in progress at the University of Notre Dame related to the performance of finite, rectangular wings¹⁵⁵, involving the Wortmann FX 63-137 airfoil section at chord Reynolds numbers less than 200,000. Attempts have been made to determine the effect of varying wing aspect ratio (based on semi-span) and chord Reynolds number on the performance of the wing as well as the effect on the separation bubble that forms under these conditions. It was first necessary to determine the two-dimensional characteristics of the profile to make adequate assessments of finite wing performance.

Force balance data was obtained for chord Reynolds numbers between 80,000 and 200,000 for three wings with different aspect ratios, as well as for the two-dimensional case. No wind tunnel corrections were applied to the force data for the finite wing cases. Figures 64-66 show the two-dimensional lift, drag and quarter-chord moment coefficients versus angle of attack as well as the drag polar for chord Reynolds numbers of 80,000, 100,000 and 200,000. Figure 67 presents some of these characteristics at $R_c = 100,000$ for a finite wing with semi-span aspect ratio of 2.7. From data of this type, it was possible to identify the effect of Reynolds number and aspect ratio upon various performance parameters.

Figure 68 shows the lift and drag curves for the infinite (i.e., two-dimensional case) and three finite wing cases at $R_c = 200,000$. It is evident that, as aspect ratio decreases, the slope of the lift curve decreases, the maximum lift decreases, minimum drag increases, while the stall angle of attack increases and the range of the hysteresis loop increases.

It was noticed that the performance of the lower aspect ratio wings was a function of chord Reynolds number. Figure 69 shows the lift and drag curves for a finite wing of semi-span aspect ratio of two, at chord Reynolds numbers of 80,000, 100,000, 150,000 and 200,000. The effect of increasing Reynolds number for a given wing was similar to the effect of increasing aspect ratio for a given Reynolds number; maximum lift increases, minimum drag decreases while the angle of attack of stall increases and the range of the hysteresis loop increases.

The effect of aspect ratio and Reynolds number upon the maximum lift coefficient is shown in Figure 70. Also plotted is the two-dimensional data from Reference¹³³, which compares reasonably well. Increases in Reynolds number and aspect ratio causes a rise in C_{Lmax} , particularly at the lower aspect ratios and Reynolds numbers. Figure 71 is a similar plot for the minimum drag coefficient. As was expected, increases in Reynolds number and aspect ratio decrease this parameter. A much lower minimum drag coefficient is found in the Stuttgart experiments using the wake rake technique¹³³. This data is also shown in Figure 71. In both cases the greatest loss in performance came between the largest aspect ratio finite wing and the infinite wing case.

Preliminary data indicated that the quarter-chord moment coefficient was not drastically affected by the downwash field generated on finite wings. Comparison of Figures 65 and 67 show that the quarter-chord moment coefficient versus angle of attack curve became "smoother" for the finite wing, but was not altered significantly in magnitude.

Further studies of this problem indicated that performance of the airfoil and the wings was linked to the development of a separation bubble on the upper surface. Since force balance data yielded very little information on this phenomenon, other experiments were necessary. Using a specially designed and constructed pressure tap model, described in detail in Appendix A of Reference 155, chordwise pressure distributions were obtained at seven spanwise stations for a finite wing ($AR=2.0$), as well as for the two-dimensional airfoil, at two Reynolds numbers. Figures 72 and 73 show the pressure distributions along the wing span on a finite wing ($AR=2.0$), as well as the two-dimensional distributions, at Reynolds numbers of 80,000 and 200,000. It should be pointed out that the static pressure taps of this model were aligned parallel to the chordline, hence an effective roughness was introduced into the problem. However, since all pressure distributions in Figures 72 and 73 were taken with the same model, comparisons of this data should yield valid information concerning separation bubble trends. Laminar separation, free shear layer transition, turbulent reattachment and turbulent separation, if they existed, are marked on the pressure distributions with "S", "T", "R" and "TS" respectively.

Figure 72 shows the effect of the downwash field upon the sectional wing characteristics for $R_c = 80,000$ and an angle of attack of 18° . One would expect the induction of air by the tip vortex to reduce the effective angle of attack, with the greatest reduction occurring near the tip. Associated with this occurrence, one would expect a reduction in the suction peak as well as laminar separation, transition and reattachment occurring farther downstream on the model, as one progresses along the span, from the root to the tip. The lower left plot is the farthest outboard station, the span station moving inboard toward the root as one progresses up and to the right on the figure, until reaching the two-dimensional distributions in the upper right. The effect on the pressure distribution is small from root to midspan. All characteristics expected are visible in Figure 72. A similar plot is presented in Figure 73, for $R_c = 200,000$ and an angle of attack of 18° . Again, reduction of the effective angle of attack was apparent in the pressure distributions as the tip was approached. In this case however, the indications of the separation bubble in the pressure distributions were masked due to the pressure tap locations and peculiarities of bubble formation at this condition. These distributions were integrated to yield the sectional lift coefficients at those stations. A summary of all angles of attack tested for $R_c = 200,000$ is presented in Figure 74. One can see very little load variation until the 60% spanwise position.

In order to verify the flow pattern variations along the span of the finite wings, surface oil visualization was performed. Loving and Katzoff¹⁵⁶, recommended that kerosene be used for flow speeds less than 35 m/s, but preliminary studies indicated that this method was not practical for the low flow speeds employed in this study (9 and 19 m/s). Winkelmann^{157,158} indicated that visualization with other thin oils was possible at low speeds. A mixture of propylene glycol and water was used. A fluorescent dye, Uranine, was added as a marker, as was a small quantity of a wetting agent to reduce surface tension in the fluid. This method worked reasonably well, except at the higher angles of attack and lower speeds. Spanwise variations of flow patterns were quite evident with this method and general trends were identified. Data obtained with this method yielded similar separation bubble fluid patterns to that of References 157 and 158, although at much lower speeds. It was concluded that this method could be a valuable tool, provided that it was used with care.

4.2 Flight Research Experiments

Because of the extreme sensitivity of low Reynolds number airfoil boundary layers to the disturbance environment in wind tunnels, evaluation of such airfoils in the atmosphere is appealing. Attaching the test airfoil section and the necessary instrumentation to a land vehicle (i.e., automobile or truck) or an airborne vehicle (i.e., sailplane or special RPV) are the obvious choices. Land vehicle testing raises the question of the possible vibrational inputs to the model being tested. Sailplanes, on the other hand, have been used successfully for many years as a test bed for low speed aerodynamics research^{136,159,160,161}. Powered (i.e., human²² or internal combustion engine⁵) aircraft have been used to determine the aerodynamic as well as stability and control characteristics of low speed vehicles. Recently, a small light-weight powered RPV has been proposed as a test-bed for obtaining low Reynolds number airfoil data¹².

In order to evaluate a new airfoil design rather than an entire vehicle, it is necessary to isolate the airfoil model from the test-bed vehicle and to "fly" the airfoil model at the desired incidence and chord Reynolds number. Successful flight tests of this type were performed by Miley¹³⁶ to evaluate his M06-13-128 airfoil design. The vehicle used was a Schweizer TG-3A sailplane. This glider has an operating equivalent airspeed range from 72.4 to 144.8 km/h (45 to 90 mph) and could be controlled to within 0.40 km/hr (0.25 mph) by an experienced pilot. After considering the best location of the test airfoil together with the effect of this configuration on the flight characteristics of the glider, Miley located the 406 mm chord 1270 mm span airfoil model upstream and above one of the sailplane's main wings at a sufficient distance from the fuselage to eliminate interference effects. The test airfoil had 609.6 mm square side plates on each end to help simulate the infinite airfoil case. Static pressure data were obtained from the 40 static pressure taps in the model and transition locations were obtained using a moveable hot-wire anemometer probe. All of the necessary instrumentation was carried on-board the sailplane.

Flight data were obtained for a chord Reynolds number of 600,000 (the design value for the M06-13-128 airfoil) at six different angles of attack. A comparison of one of the pressure distributions obtained in these sailplane tests and data obtained in a wind tunnel at the University of Notre Dame with the theoretical values is shown in Figure 75¹⁴⁰. Because this case represents a speed slightly beyond the normal upper limit of the Notre Dame low speed wind tunnel, the wind tunnel pressure coefficients are included only to indicate the similar trend with the flight data.

To obtain airfoil data on reasonably sized models (i.e., a minimum of about 152 mm chord) and Reynolds numbers below 500,000, piloted sailplanes with good low speed stability and control characteristics must be used. Also, remotely piloted, considerably smaller sailplanes may be used. As the size of the sailplane decreases, the ability to carry pressure measuring instrumentation, etc. for airfoil measurements is decreased. For small sailplane or powered RPV test-bed configurations, the desired airfoil characteristics must then be backed-out of the entire vehicle characteristics from (for example) power-off sink rate experiments. Although this has been accomplished with some success at chord Reynolds numbers above 500,000, further studies are necessary to demonstrate the validity of this approach at lower Reynolds numbers. The question of accuracy of data obtained and possible interference from other components of the vehicle must also be considered.

5. PRACTICAL APPLICATIONS

A wide variety of practical applications, where low Reynolds number effects are present for all or part of the operating period, have been studied. The success of many of these configurations is strongly dependent upon achieving the highest aerodynamic efficiency of the lifting surfaces i.e., the wings or rotors. A few examples of specific types of configurations and their missions will be presented to illustrate this point.

5.1 Remotely Piloted Vehicles and Sailplanes

An extremely large number of RPV's have been designed and flown over the past 35 years. Many of these vehicles are little more than small scale airplanes and are often used to study the flight performance and stability characteristics of the full size airplane. Tethered RPV's in large wind tunnels and untethered RPV's in vertical spin tunnels and in atmospheric flight have been operated successfully for many years. Recent advances in reducing the size and weight of electronic payloads while increasing their sensing capability, the use of light-weight and composite structures, and in development of non-conventional propulsion systems (e.g., solar/electric, fuel cell, and microwave/electric) have greatly enlarged the possible applications of RPV's.

Preliminary design studies of high altitude aircraft platforms (HAAPs) have recently been completed^{10,14,162-164}. One possible mission for such a solar powered vehicle is agricultural surveillance. For this type of mission a high altitude long endurance platform capable of carrying a 112.5 kg (250 lbm) payload with a daytime power requirement of 300 watts has been studied¹⁶² and an early design resulting from this continuing effort is shown in Figure 76. This platform would be capable of maintaining 20 km (65,600 ft) altitude over, for example, California's San Joaquin Valley (32° -38°N latitude) for up to 12 months. During this period the payload would monitor crop conditions on an hourly basis. Design studies indicate that such a vehicle might have a wing span on the order of 100 m (328 ft) and a mean aerodynamic chord on the order of 3 m (9.84 ft). At speeds of 10 m/s (32.8 fps) and at 20 km, (65,600 ft) the chord Reynolds numbers are less than 500,000. For lack of suitable low Reynolds number airfoil designs, these studies have used published airfoils designed for other purposes, e.g. the Liebeck L 1003M¹⁶², the Wortmann FX74-CL5-40¹⁶² and the Wortmann FX 63-137¹⁶⁴. Not only have these airfoils not been designed for this type of vehicle, but sufficient wind tunnel and flight test data are not available to guarantee the actual performance of these designs. Even with future improvements in regenerative solar propulsion systems, it appears that more efficient airfoil and wing designs are necessary. HAAP lift to drag ratios on the order of 50-60 appear to be necessary. The highest aerodynamic efficiency of any man-made vehicle is the modern sailplane where lift to drag ratios of near 50 have already been attained. In order to obtain further improvements in L/D, it appears that active boundary layer control (e.g., blowing or suction) and the use of multi-element airfoil geometries may be necessary. Furthermore, the propeller used in such HAAPs have a mean aerodynamic chord which is at least an order of magnitude smaller than the wing (i.e., about 0.3m). Rotating at between 100 and 200 rpm, most of the propeller designs operate continuously in the low Reynolds number regime. Although there has been some recent attention to the design of propellers of this type¹⁶⁵, the airfoil sections are also chosen from published data and not designed specifically for the new application. The design of this type of propeller is similar to the design of low solidity wind turbine blades and will be discussed in the next section.

The Mini-Sniffer⁵ shown in Figure 77 is an example of an operationally successful mini-RPV. The original mission called for a vehicle to carry a 26.8 kg (59 lbm) air sampler to 21,336 m (70,000 ft) and cruise there for an hour within a range of 311.8 km (200 miles) or glide back after a 27.4 km (90,000 ft) climb. Using a hydrazine monopropellant engine, a 76 kg (167 lbm) vehicle was developed using the Miley M06-13-128 airfoil section¹³⁶ for the main wing [mean aerodynamic chord = 0.661 m (2.17 ft), span = 5.48 m (18 ft)] and the Clark-Y airfoil section for the 2 bladed propeller. The chord Reynolds numbers for such a mission could get as low as about 60,000. In the test program, however, [in which altitudes of about 6.09 km (20,000 ft) were attained] the minimum chord Reynolds number was about 250,000. The maximum L/D of this vehicle was determined from power-off sink rate tests from 6.09 km (20,000 ft) to be about 15. (L/D)_{max} with the landing gear off was estimated to be slightly over 20. Current mini-RPV requirements indicate that improvements in aerodynamic efficiency in the vicinity of $C^{3/2}/C_D = 20$ are necessary to increase on-station endurance of reciprocating engine/propeller vehicles to about 10 hours. Furthermore these vehicles must be capable of flying in all kinds of weather without significant reductions in performance.

5.2 Wind Turbines

Over the past ten years, development of wind energy systems has been increasing. This growth is, in part, due to the the Federal Wind Energy Program in the United States and an interest in renewable energy sources caused by the rising cost of fossil fuels worldwide. The focus of this work has been on high efficiency, lift-type wind turbines such as the HAWT (horizontal axis wind turbine) and the VAWT (vertical axis wind turbine) shown in Figure 78. Both types are designed to extract energy through an efficient aerodynamic interaction between the wind and blade elements. This optimization has led to a class of turbines characterized by high efficiency, high speed (i.e., tip to wind speed ratios of about 6, shown in Figure 79), and low solidity (ratio of blade area to swept area). These characteristics of the modern wind turbine lead to several consequences.

Until now, the structural integrity of these wind machines has been the primary focus of research due to the high blade loadings. Here the aerodynamics were considered only as input to aeroelastic problems. Choice of airfoil section was generally based upon structural considerations and the availability of airfoil section data. This data was used not only in structural analysis, but also in predicting turbine performance. Unfortunately, most available section data was for Reynolds numbers of several million. In both the HAWT and VAWT, chord Reynolds numbers of less than 500,000 do occur in sections of the rotor near the rotating axis. Modern turbines with power output less than about 15 kW may experience Reynolds numbers less than 500,000 at all times due to their low solidity. The choice of a low Reynolds number airfoil for a wind turbine involves several considerations which are unique to this application.

The problems associated with the design of a low Reynolds number HAWT are the same as those encountered in designing a low Reynolds number propeller. Essentially, the design of the airfoil section must take into account the operating character of the rotor. Lift and drag produced by a HAWT rotor blade element may be resolved into an equivalent normal and thrust force as shown in Figure 80. The magnitude of the driving force is a function of the relative velocity and angle of attack. Additionally, one must consider the geometric twist and relative velocity as functions of the blade element radius. Airfoil design is

complicated in two ways. First, the Reynolds number is a function of radius. This is equivalent to a finite wing experiencing spanwise wind shear. Second, the direction and speed of the wind are not constant, causing an unsteady loading of the turbine. Also, consideration must be given to three dimensional effects due to the finite aspect ratio and the geometric twist of the blade.

The Darrieus VAWT has more complex aerodynamics. This type of wind turbine produces power as a result of the tangential thrust as shown in Figure 81. Operation is complicated by the fluctuating angle of attack experienced by a blade element. The designer must not only account for the design state of the wind turbine, but also an unsteady pitching. In order for power to be produced at all azimuthal blade angles, the thrust force must be positive for both positive and negative angles of attack, hence, one would expect a symmetrical airfoil to be practical. Again, for structural considerations and data availability, NACA symmetrical sections are currently used. Some testing has been done on these airfoils at low Reynolds numbers¹⁶⁶, but little has been done to address the unsteady behavior of these airfoils at low Reynolds numbers. In addition to the unsteady angle of attack phenomenon, the range of angle of attack may approach 180° in portions of the rotor near the axis. Section data for full-range (-180° to 180°) is very limited even for high Reynolds numbers. Example of thrust coefficient data versus angle of attack for a symmetrical NACA 0015 airfoil at $R_c = 350,000$ ¹⁶⁷ and for a highly cambered Wortmann FX 63-137 airfoil at $R_c = 125,000$ ¹⁶⁸ are shown in Figure 82. The FX 63-137 data was obtained by changing the angle of attack only in one direction, therefore, no hysteresis could be observed.

The design and testing of low Reynolds number sections for use in wind turbines requires careful study of the rotor aerodynamic characteristics. In general, the designer must consider unsteady, three-dimensional performance over a wide range of Reynolds numbers and angles of attack. There is a definite need for full-range low Reynolds number airfoil section data for use in wind turbine design codes. Data is also needed for full-range unsteady airfoil section characteristics. To this end, a study is currently in progress at the University of Notre Dame addressing the characteristics of airfoils at low Reynolds numbers in unsteady flows.

6. CONCLUDING REMARKS

In order to achieve the aerodynamic efficiency levels necessary for successful operation of low Reynolds number vehicles at subcritical speeds, improved airfoil sections and wing designs are necessary. Present design techniques produce airfoil sections which perform as they are designed for chord Reynolds numbers above about 500,000. For chord Reynolds numbers below about 500,000, airfoil sections are much more difficult to design with confidence because the effects of laminar separation bubbles and/or transition have not been adequately modelled in the design and analysis methods. The fact that more than one airfoil flowfield is possible at a given angle of attack (i.e., hysteresis) indicates that further research is necessary in this area.

To improve the design and analysis methods in this flight regime, experimental determination of the influence of free disturbance environment, surface roughness, and unsteady flow effects is necessary. Our understanding of these complex flow phenomena can be enhanced with definitive wind tunnel experiments. In wind tunnel experiments, care must be exercised to determine the influence of the test section disturbance environment, the experimental technique, instrumentation, data processing and procedure used, on the results. The airfoil boundary layer may also be sensitive to small imperfections in the wind tunnel model profile. Flight experiments, though usually more time consuming and expensive than wind tunnel experiments, may also be necessary to insure that a given airfoil design receives a fair evaluation under actual operating conditions.

7. RECOMMENDATIONS FOR FUTURE RESEARCH

Given the wide variety of low Reynolds number applications of current interest and the present small aerodynamic data base, the following recommendations are presented for future research. Both single- and multi-element airfoil sections need to be considered as well as the benefits of active boundary layer control concepts.

- 1) The question of when and where transition from laminar to turbulent flow takes place in the attached or separated airfoil boundary layer is of primary importance. Improvements in both design and analysis methods require a more complete understanding of the stability and transition of viscous shear layers. Definitive experiments into these phenomena in airfoil type pressure gradients as affected by the free stream disturbance environment and airfoil surface roughness characteristics are necessary. All wind tunnel experiments in this area must be preceded by an extensive study of the unique disturbance environment of the experimental facility used and how this may affect the results.
- 2) In order to include a separation bubble model in both design and analysis methods, more detailed experimental studies are needed of the structure of the rather extensive separation bubbles which occur.
- 3) A systematic study, both experimental and analytical, of the unsteady flow effects on laminar separation and transition is also necessary.

- 4) To improve the experimental evaluation of new airfoil and vehicle designs, the experimental measurement techniques should continue to be improved and evaluated so that more accurate wind tunnel and flight data may be obtained.
- 5) Analytical methods should continue to be extended and improved in conjunction with experimental findings. The analytical and experimental approaches should proceed so as to compliment each other. In this way a more rapid solution to the design problems will be achieved.
- 6) The analytical and experimental techniques should be extended to include the fully integrated practical configurations of interest.

REFERENCES

1. Carmichael, B.H., "Low Reynolds Number Airfoil Survey Volume I," NASA CR 165803, November 1981.
2. Miley, S.J., "A Catalog of Low Reynolds Number Airfoil Data for Wind Turbine Applications," Aerospace Engineering Department, Texas A&M University, February 1982.
3. Lissaman, P.B.S., "Low Reynolds Number Airfoils," Annual Review of Fluid Mechanics, Vol. 15, pp. 223-239, 1983.
4. McMasters, J.H. and Henderson, M.L., "Low-Speed Single-Element Airfoil Synthesis," NASA CP 2085, Part I, pp. 1-31, March 1979.
5. Reed, D.R., "High-Flying Mini-Sniffer RPV: Mars Bound?" Astronautics and Aeronautics, pp. 26-39, June 1978.
6. Heyson, H.H., "Initial Feasibility Study of a Microwave-Power Sailplane as a High-Altitude Observation Platform," NASA TM 78809, December 1978.
7. Turriziani, R.V., "Sensitivity Study for a Remotely Piloted Microwave-Powered Sailplane Used as a High-Altitude Observation Platform," NASA CR 159089, June 1979.
8. Youngblood, J.W., Darnell, W.L., Johnson, R.W., and Harriss, R.C., "Airborne Spacecraft -A Remotely Powered, High-Altitude, RPV for Environmental Applications," presented at the Electronics and Aerospace Systems Conference, Arlington, Virginia, October 9-11, 1979.
9. Zehentner, R., "Cost Sensitivity Analysis and Aerodynamic Performance Improvements for a High Altitude Aerodynamic Platform Preliminary Design Concept," JSC Report 17268, March 1981.
10. Youngblood, J.W. and Talay, T.A., "Solar-Powered Airplane Design for Long-Endurance, High-Altitude Flight," AIAA Paper No. 82-0811, presented at the AIAA 2nd International Very Large Vehicles Conference, Washington, D.C., May 17-19, 1982.
11. Graves, E.B., "The Feasibility of a High-Altitude Aircraft Platform with Consideration of Technological and Societal Constraints," NASA TM 84508, June 1982.
12. DaCosta, R.A., Lovell, W.A., Martin, G.L., Price, J.E. and Turriziani, R.V., "Design and Analysis of a Small, Light-Weight RPV Test-Bed for Obtaining Airfoil Data at Low Reynolds Numbers," NACA CR 165978, September 1982.
13. Morris, C.E.K. Jr., "Design Study for Remotely Piloted High-Altitude Airplanes Powered by Microwave Energy," AIAA Paper No. 83-1825, presented at the AIAA Applied Aerodynamics Conference, Danvers, Massachusetts, July 13-15, 1983.
14. Youngblood, J.W., "Airborne Reconnaissance in the Civilian Sector: Agricultural Monitoring From High-Altitude Powered Platforms," SPIE Paper No. 424-24, presented at the Society of Photo-Optical Instrumentation Engineers 27th Annual International Technical Symposium and Instrument Display, San Diego, California, August 21-26, 1983.
15. Akkerman, J.W., "Hot-Gas Engine with Piston-Actuated Valve," SAE Paper No. 780763, presented at the Off-Highway Vehicle Meeting and Exposition, MECCA, Milwaukee, Wisconsin, September 11-14, 1978.
16. Akkerman, J.W., "Hydrazine Monopropellant Reciprocating Engine Development," ASME Journal of Engineering for Industry, Vol. 101, No. 4, pp. 456-462, November 1979.
17. Liu, G.C., Morris, C.E.K. Jr., and Koenig, R.W., "Performance of High-Altitude, Long-Endurance Turboprop Airplanes Using Conventional or Cryogenic Fuels," NASA TM 84534, January 1983.
18. Chen, M.K. and McMasters, J.H., "From Paleoaeronautics to Allostratus -A Technical History of Soaring," AIAA Paper No. 81-1611, presented at the AIAA Aircraft Systems and Technology Conference, Dayton, Ohio, August 11-13, 1981.
19. McMasters, J.H., "The Ultralight Sailplane," NASA CP 2085, Part II, pp. 485-504, March 1979.

20. Markowski, M.A., "Ultralight Flight," Ultralight Aviation Series No. 3, Ultralight Publications, P.O. Box 234, Hummelstown, PA 17036, 1982.
21. Burke, J.D., "The Gossamer Condor and Albatross: A Case Study in Aircraft Design," AeroVironment Inc. Report AV-R-80/540, June 1980.
22. Jex, H.R. and Mitchell, D.G., "Stability and Control of the Gossamer Human-Powered Aircraft by Analysis and Flight Test," NASA CR 3627, October 1982.
23. MacCready, P.B., Lissaman, P.B.S., Morgan, W.R., and Burke, J.D., "Sun-Powered Aircraft Design," AIAA Paper 81-0916, May 1981.
24. Hill, M.L., "Design and Performance of Electrostatically Stabilized Delta Planform Mini Remotely Piloted Vehicles," Conference Proceedings, Military Electronic Defense Exposition, Wiesbaden, West Germany, October 1977, Interavia SA, Geneva, Switzerland, pp. 847-861.
25. Hill, M.L., Whyte, T.R., Weiss, R.O., Rubio, R. and Isquierdo, M., "Use of Atmospheric Electric Fields for Vertical Stabilization and Terrain Avoidance," AIAA 81-1848-CP, presented at the AIAA Guidance and Control, Albuquerque, New Mexico, August 19-21, 1981.
26. Hill, M.L., "Designing a Mini-RPV for a World Endurance Record," Astronautics and Aeronautics, pp. 47-54, November 1982.
27. "Remotely Piloted Vehicles -Aerodynamics and Related Topics," Lecture Series 101, Volumes 1 and 2, vonKarman Institute for Fluid Dynamics, May 23-27, 1977.
28. "Remotely Piloted Vehicles," Proceedings of Third International Conference, Bristol, United Kingdom, September 13-15, 1982.
29. Hunt, V.D., "Wind Power," Van Nostrand Reinhold Company, New York, 1981.
30. McMasters, J.H., "An Analytical Survey of Low-Speed Flying Devices -Natural and Man-Made," AIAA Paper No. 74-1019, September 1974.
31. Dwiggin, D., "Dangerous When Wet?," Homebuilt Aircraft, April 1983.
32. Luers, J.K., "Wing Contamination: Threat to Safe Flight," Astronautics and Aeronautics, pp. 54-59, November 1983.
33. Yip, L.P. and Coy, P.F., "Wind-Tunnel Investigation of a Full-Scale Canard-Configured General Aviation Aircraft," ICAS Paper 82-6.8.2, presented at the 13th ICAS Congress/AIAA Aircraft Systems Technology Conference, Seattle, Washington, August 22-27, 1983.
34. Nelson, R.C., Curtin, M.M., and Payne, F.M., "A Combined Experimental and Analytical Investigation of the Influence of Low Level Wind Shear on the Handling Characteristics of Aircraft," U.S. Department of Transportation Report, DOT/RSPA/DMA -50/83/29, October 1979.
35. Mueller, T.J., and Batill, S.M., "Experimental Studies of Separation on a Two-Dimensional Airfoil at Low Reynolds Numbers," AIAA Journal, Vol.20, No. 4, pp. 457-463, April 1982.
36. Schlichting, H., Boundary Layer Theory, Seventh Edition, McGraw-Hill Book Company, 1979.
37. Mueller, T.J., Pohlen, L.J., Conigliaro, P.E., and Jansen, R.J., Jr., "The Influence of Free-Stream Disturbances on Low Reynolds Number Airfoil Experiments," Experiments in Fluids, Vol. 1, pp. 3-14, Springer-Verlag, 1983.
38. Wortmann, F.X., "Progress in the Design of Low Drag Airfoils," in Boundary Layer and Flow Control, Vol. 2, Pergamon Press Ltd., 1961.
39. Tani, I., "Low-Speed Flows Involving Bubble Separation," Progress in Aeronautical Sciences, Vol. 5, MacMillan Co., 1974.
40. Pohlen, L.J., and Mueller, T.J., "Experimental Studies of the Effect of Boundary Layer Transition on the Performance of the Miley (M06-13-128) Airfoil at Low Reynolds Numbers," AIAA Paper 83-1795. Presented at the AIAA Applied Aerodynamics Conference, Danvers, Massachusetts, July 13-15, 1983.
41. Gaster, M., "The Structure and Behavior of Laminar Separation Bubbles," NPL Aero Report 1181, ARC 28,226, 1966.
42. Selig, M.S., "The Design of Airfoils at Low Reynolds Numbers," University of Illinois at Urbana-Champaign, 1984, also AIAA Paper No. 85-0074.
43. Mueller, T.J., "The Influence of Laminar Separation and Transition on Low Reynolds Number Airfoil Hysteresis," AIAA 84-1617, presented at the AIAA 17th Fluid Dynamics, Plasmadynamics and Lasers Conference, Snowmass, Colorado, June 25-27, 1984.
44. Jones, B.M., "An Experimental Study of the Stalling of Wings," NACA Reports and Memoranda No. 1588, December 1933.

45. Schmitz, F.W., "Aerodynamics of the Model Airplane. Part I, Airfoil Measurements," Keystone Scientific Information Center, 1941.
46. McCullough, G.R. and Gault, D.E., "Examples of Three Representative Types of Airfoil-Section Stall at Low Speed," NACA TN 2502, 1951.
47. Gault, D.E., "An Experimental Investigation of Regions of Separated Laminar Flow," NACA TN 3505, 1955.
48. Owen, P.R. and Klanfer, L., "On the Laminar Boundary Layer Separation from the Leading Edge of a Thin Airfoil," ARC, CP 220, 1953.
49. Pfenniger, W., "Experimental Investigation of an Airfoil with High Lift to Drag Ratios at Low Reynolds Numbers," Report No. BLC-84 Northrop Aircraft Inc., February 1956.
50. Moore, T.W.F., "Some Experiments on the Reattachment of a Laminar Boundary Layer Separating From a Rearward Facing Step on a Flat Plate Airfoil," Journal of the Royal Aero Soc., November 1960.
51. Gaster, M., "On the Stability of Parallel Flows and the Behavior of Laminar Separation Bubbles," Ph.D. Thesis, University of London, also see British ARC R&M 3595, 1969.
52. Ward, J.W., "The Behavior and Effects of Laminar Separation Bubbles on Aerofoils in Incompressible Flow," Journal of the Royal Aeronautical Society, Volume 67, December 1963.
53. Horton, H.P., "A Semi-Empirical Theory for the Growth and Bursting of Laminar Separation Bubbles," Aeronautical Research Council Current Papers, University of London, England, 1969.
54. Ntim, B.A., "A Theoretical and Experimental Investigation of Separation Bubbles," Ph.D. Thesis, University of London (Queen Mary College), 1969.
55. Roberts, W.B., "Calculation of Laminar Separation Bubbles and Their Effect on Airfoil Performance," AIAA Journal, Vol. 18, No. 1, pp. 25-30, January 1980.
56. van Ingen, J.L., "Theoretical and Experimental Investigations of Incompressible Laminar Boundary Layers with and without Suction," Technological University, Delft, Netherlands, October 1965.
57. Althaus, D., "Influencing Transition on Airfoils," presented at the XVII OSTIV Congress, Paderborn, W. Germany, 1981.
58. Volkers, D.F., "Preliminary Results of Windtunnel Measurements on some Airfoil Sections at Reynolds Numbers Between 0.6×10^5 and 5.0×10^5 ," Delft University of Technology, Memorandum M-276, Netherlands, June 1977.
59. Arena, A.V. and Mueller, T.J., "On the Laminar Separation, Transition, and Turbulent Reattachment of Low Reynolds Number Flows Near the Leading Edge of Airfoils," AIAA Paper 79-0004, 1979.
60. Mueller, T.J., and Burns, T.F., "Experimental Studies of the Fopler 61 Airfoil at Low Reynolds Numbers," AIAA Paper 82-0345, 1982.
61. Conigliaro, P.E., "An Experimental Investigation of the Low Reynolds Number Performance of the Lissaman 7769 Airfoil," AIAA Paper 83-0647, 1982.
62. Jansen, B.J. Jr., "Experimental Studies of the Effect of the Laminar Separation Bubble on the Performance of a NACA 663-018 Airfoil at Low Reynolds Numbers," Masters Thesis, University of Notre Dame, 1982.
63. Mehta, V.B., "Dynamic Stall of an Oscillating Airfoil," Paper No. 23, presented by AGARD Fluid Dynamics Panel Symposium on Unsteady Aerodynamics, Ottawa, Canada, September 1972.
64. Hodge, J.K., Stone, A.L., and Miller, T.E., "Numerical Solution for Airfoils near Stall in Optimized Boundary-Fitted Curvilinear Coordinates," AIAA Journal, Vol. 17, No. 5, pp. 458-464, May 1979.
65. Hegna, H.A., "The Numerical Solution of Incompressible Turbulent Flow Over Airfoils," AIAA Paper No. 81-0047, presented at the AIAA 19th Aerospace Sciences Meeting, St. Louis, Missouri, January 12-15, 1981.
66. Mueller, T.J., Jansen, B.J., Jr., Bernard, R.S., and Thompson, J.F., "Experimental and Numerical Studies of the Incompressible Viscous Flow over a Two-Dimensional Airfoil," Proceedings of ASME Symposium on Computers in Flow Prediction and Fluid Dynamics Experiments, pp. 157-162, Washington, D.C., November 15-20, 1981.
67. Hegna, H.A., "Numerical Prediction of Dynamic Forces on Arbitrarily Pitched Airfoils in Turbulent Flow," AIAA Paper No. 82-0092, presented at the AIAA 20th Aerospace Sciences Meeting, Orlando, Florida, January 11-14, 1982.
68. Wright, A.F., "A Numerical Investigation of Low Reynolds Number Flow Over an Airfoil," MS Thesis, Department of Aerospace Engineering, University of Maryland, July 1982.
69. Kothari, A.P., Anderson, J.D., Jr., and Raghaven, V.R., "The Aerodynamics of Airfoils at Low Reynolds Number (Computational Aspects)," Technical Report AE-84-1, Department of Aerospace Engineering, University of Maryland, January 1984.

70. Thompson, J.F. (Editor), Numerical Grid Generation, Elsevier Science Publishing Company, Inc., 1982.
71. Thwaites, B. (Editor), Incompressible Aerodynamics, Oxford at the Clarendon Press, 1960.
72. Cebeci, T., and Clark, R.W., "An Iterative Approach to Subsonic Flows with Separation," Second Symposium on Numerical and Physical Aspects of Aerodynamic Flows, California State University, January 17-20, 1983.
73. Kwon, O.K., and Pletcher, R.H., "Prediction of Subsonic Separation Bubbles on Airfoils by Viscous-Inviscid Interaction," Second Symposium on Numerical and Physical Aspects of Aerodynamic Flows, California State University, January 17-20, 1983.
74. Davis, R.L., and Carter, J.E., "Analysis of Airfoil Transitional Separation Bubbles," NASA CR-165935, 1983.
75. Gleyzes, C., Cousteix, J., and Bonnet, J.L., "A Calculation Method of Leading Edge Separation Bubbles," Second Symposium on Numerical and Physical Aspects of Aerodynamic Flows, California State University, January 17-20, 1983.
76. Cheng, H.K., "Laminar Separation from Airfoils Beyond Trailing-Edge Stall," AIAA Paper No. 84-1612, presented at the AIAA 17th Fluid Dynamics, Plasma Dynamics and Lasers Conference, Snowmass, Colorado, June 25-27, 1984.
77. Landahl, M.T., "Wave Breakdown and Turbulence," Proceedings of the International Symposium on Modern Developments in Fluid Dynamics, SIAM, pp. 215-236, 1977.
78. Betchov, R., Transition: Handbook of Turbulence, Vol. 1, edited by W. Frost and T.H. Moulden, Plenum Publishing Company, pp. 147-164, 1977.
79. AGARD-CP-224: "Laminar-Turbulent Transition," Proceedings of the AGARD Fluid Dynamics Panel Symposium, Copenhagen, Denmark, 1977.
80. Morkovin, M.V., "Technical Evaluation Report of the Fluid Dynamics Panel Symposium on Laminar-Turbulent Transition," AGARD-AR-122, June 1978.
81. Swinney, H.L., and Gollub, J.P., "The Transition to Turbulence," Physics Today, pp. 41-49, August 1978.
82. Lochtenberg, B.H., "Transition in a Separated Laminar Boundary Layer," Journal of the Aero-Space Sciences, pp. 92-96, February 1960.
83. Browand, F.K., "An Experimental Investigation of the Instability of an Incompressible Separated Shear Layer," M.I.T. Department of Aeronautics and Astronautics, Report ASRL-TR-92-4, January 1965; also Journal of Fluid Mechanics, Vol. 26, Part 2, pp. 281-307, 1966.
84. Roshko, A., "Transition in Incompressible Near Wakes," The Physics of Fluids Supplement, Boundary Layers and Turbulence, pp. S181-S182, 1967.
85. Goldstein, R.J., Ericksen, V.L., Olsen, R.M., and Eckert, E.R.G., "Laminar Separation, Reattachment and Transition of the Flow over a Downstream-Facing Step," ASME Paper 69-WA/FE-5, 1969.
86. Freymuth, P., "On Transition in a Separated Laminar Boundary Layer," Journal of Fluid Mechanics, Vol. 25, Part 4, pp. 683-704, 1966.
87. Moore, C.J., "The Effect of Shear Layer Instability on Jet Exhaust Noise," Lecture Notes in Physics, No. 76, Vol. II, Springer-Verlag, pp. 254-264, 1978.
88. Davies, P.O.A.L., and Baxter, D.R.J., "Transition in Free Shear Layers," Lecture Notes in Physics, No. 76, Vol. I, Springer-Verlag, pp. 124-135, 1978.
89. Cebeci, T., and Bradshaw, P., Momentum Transfer in Boundary Layers, Hemisphere Publishing Corporation, 1977.
90. "Laminar Turbulent Transition," IUTAM Symposium, Stuttgart, Germany, 1979. Published by Springer-Verlag, Editors R. Eppler and H. Fasel, 1980.
91. "Transition and Turbulence," Mathematics Research Center Symposium, The University of Wisconsin, 1980. Published by Academic Press, Editor R.E. Meyer, 1980.
92. Batill, S.M., and Mueller, T.J., "Visualization of Transition in the Flow Over an Airfoil Using the Smoke-Wire Technique," AIAA Journal, Vol. 19, No. 3, pp. 340-345, March 1981.
93. "Proceedings of the Computation of Turbulent Boundary Layers," 1968 AFOSR-IFP-Stanford Conference, edited by Kline, S.J., Morkovin, M.V., Sovran, G., and Cockrell, D.J., Volumes I and II, August 18-25, 1968.
94. Hussain, A.K.M.F., "Coherent Structures-Reality and Myth," The Physics of Fluids, Vol. 26, No. 10, pp. 2816-2850, October 1983.

95. Doligalski, T.L., Smith, C.R., and Walker, J.D.A., "Production Mechanism for Turbulent Boundary-Layer Flows," in Viscous Flow Drag Reduction, edited by G.R. Hough, Vol. 72, Progress in Astronautics and Aeronautics, published by AIAA, pp. 47-72, 1980.
96. Perry, A.E., Lin, T.T., Chong, M.S., and Teh, E.W., "The Fabric of Turbulence," AIAA Paper No. 80-1358, presented at the 13th AIAA Fluid and Plasma Dynamics Conference, Snowmass, Colorado, June 14-16, 1980.
97. Kegelman, J.T. and Mueller, T.J., "Experimental Studies of Spontaneous and Forced Transition on an Axisymmetric Body," AIAA Paper No. 84-0008, presented at the AIAA 22nd Aerospace Sciences Meeting, Reno, Nevada, January 9-12, 1984.
98. Saric, W.S., Kozlov, V.V., and Levchenko, V. Ya, "Forced and Unforced Subharmonic Resonance in Boundary-Layer Transition," AIAA Paper No. 84-0007, presented at the AIAA 22nd Aerospace Sciences Meeting, Reno, Nevada, January 9-12, 1984.
99. Reynolds, W.C. and Cebeci, T., "Calculation of Turbulent Flows," Chapter 5 in Turbulence, edited by F. Bradshaw, Springer-Verlag, Berlin, pp. 193-229, 1978.
100. Fernholz, H.H., "External Flows," Chapter 2 in Turbulence, edited by P. Bradshaw, Springer-Verlag, Berlin, pp. 45-107, 1978.
101. Bradshaw, P., Cebeci, T., and Whitelaw, J.H., "Engineering Calculation Methods for Turbulent Flow," Academic Press, 1981.
102. Berry, D.T., "A Visual Investigation of Laminar Separation and Turbulent Rejoining of the Boundary Layer as Affected by Angle of Attack," M.S. Dissertation, University of Notre Dame, 1955.
103. Abbott, I.H. and von Doenhoff, A.E., Airfoil Sections, New York, Dover, 1959.
104. Riegels, F.W., Airfoil Sections, London: Butterworth, 1961.
105. Jacobs, E.N., and Sherman, A., "Airfoil Section Characteristics as Affected by Variations of the Reynolds Number," NACA TR 586, 1937.
106. Wortmann, F.X., "Experimental Investigations on New Laminar Profiles for Gliders and Helicopters," Ministry of Aviation Translation TIL/T.4906, March 1980 (Avail. ASTIA, Arlington, VA)(z. Flugwiss, Vol. 5, No. 8, 1957, pp. 228-48).
107. Wortmann, F.X., "A Critical Review of the Physical Aspects of Airfoil Design at Low Mach Number," Motorless Flight Research -1972, J.L. Nash-Weber, ed. NASA CR 2315, November 1973.
108. Eppler, R., "Direkte Berechnung von Tragflugelprofilen aus der Druckverteilung," Ingenieur-Archiv, Vol. 25, No. 1, pp. 32-57, 1957. English translation available as NASA TT F-15, 417.
109. Eppler, R., "Praktische Berechnung laminarer und turbulenter Absaug- Grenzschichten," Ingenieur-Archiv, Vol. 32, No. 4, pp. 221-245, 1963. English translation available as NASA TM-75328.
110. Miley, S., "On the Design of Airfoils for Low Reynolds Numbers," AIAA Paper No. 74-1017, September 1974.
111. Henderson, M.L., "Inverse Boundary Layer Technique for Airfoil Design," Proceedings NASA Advanced Technology Airfoil Research (ATAR) Conference, March 1978.
112. Henderson, M.L., "Inverse Boundary Layer Technique for Airfoil Design," Advanced Technology Airfoil Research, Vol. 1, NASA CP-2045, Pt. 1, pp. 383-397, 1978.
113. Liebeck, R.H., "Design of Subsonic Airfoils for High Lift," Journal of Aircraft, Vol. 15, No. 9, pp. 547-61, September 1978.
114. van Ingen, J.L., "Advanced Computer Technology in Aerodynamics: A Program for Airfoil Section Design Utilizing Computer Graphics," Lecture notes for Von Karman Institute of Fluid Dynamics, 1969, AGARD lecture series No. 73, "High Reynolds Number Subsonic Aerodynamics," pp. 8.1-8.33, 1970.
115. van Ingen, J.L., Boermans, L.M.M., and Blom, J.J.H., "Low-Speed Airfoil Section Research at Delft University of Technology," 12th Congress of the International Council of the Aeronautical Sciences, Munich, pp. 401-416, October 1980.
116. Lissaman, P.B.S., "Wings for Human-Powered Flight," AIAA SP802, Proceedings of the Symposium on Evolution of Aircraft Wing Design, pp. 49-56, 1980.
117. Eppler, R., and Somers, D.M., "Low Speed Airfoil Design and Analysis," Advanced Technology Airfoil Research -Volume I, NASA CP-2045, Part 1, pp. 73-99, 1979.
118. Eppler, R., and Somers, D.M., "A Computer Program for the Design and Analysis of Low-Speed Airfoils," NASA TM-80210, 1980.
119. Eppler, R., and Somers, D.M., Supplement to: "A Computer Program for the Design and Analysis of Low-Speed Airfoils," NASA TM-81862, 1980.

120. Volkers, D.F., "Preliminary Results of Wind Tunnel Measurements on Some Airfoil Sections at Reynolds Numbers Between 0.6×10^5 and 5.0×10^5 . Memorandum M-276, Delft University of Technology, Department of Aerospace Engineering, The Netherlands, 1977.
121. Somers, D.M., "Design and Experimental Results for a Natural-Laminar-Flow Airfoil for General Aviation Applications," NASA TP-1861, 1981.
122. Somers, D.M., "Design and Experimental Results for a Flapped Natural-Laminar-Flow Airfoil for General Aviation Applications," NASA TO-1865, 1981.
123. Kothari, A.P., and Anderson, J.D., Jr., "Flows Over Low Reynolds Number Airfoils --Compressible Navier-Stokes Numerical Solutions," AIAA Paper No. 85-0107, January 1985.
124. Baldwin, B.S., and Lomax, H., "Thin Layer Approximation and Algebraic Model for Separated Turbulent Flows," AIAA Paper No. 78-257, January 1978.
125. Thompson, J.F., Thames, F.C., and Mastin, C.W., "Automatic Numerical Generation of Body-Fitted Curvilinear Coordinate Systems for Fields Containing Any Number of Arbitrary Two-Dimensional Bodies," Journal of Computational Physics, Vol. 15, No. 3, 1974.
126. MacCormack, R.W., "A Numerical Method for Solving the Equations of Compressible Viscous Flow," AIAA Paper No. 81-0110, 1981.
127. Mueller, T.J., Jansen, B.J.Jr., "Aerodynamic Measurements at Low Reynolds Numbers," AIAA Paper No. 82-0598, 1982.
128. Pope, A., and Harper, J.J., "Low-Speed Wind Tunnel Testing," John Wiley and Sons, Inc., 1966.
129. Althaus, D., "Drag Measurements on Airfoils," presented at OSTIV Congress, Paderborn, West Germany, 7 pages, 1981.
130. Rogers, E.W.E., "Blockage Effects in Closed or Open Tunnels," AGARDograph 109, pp. 279-340, 1966.
131. Kline, S.J., and McClintock, F.A., "Describing Uncertainties in Single-Sample Experiments," Mechanical Engineering, p. 3, 1953.
132. deVries, J., Hegen, G.H., and Boermans, L.M.M., "Preliminary Results of Wind Tunnel Numbers on Airfoil Section E61," Dept. Aero. Engr., Delft University of Technology, 1980.
133. Althaus, D., "Profilpolaren fur den Modellflug," Nectar-Verlag, Institut fur Aerodynamik und Gasdynamik, University of Stuttgart, 1980.
134. Mueller, T.J., "Flow Visualization by Direct Injection," Chapter 7 of Fluid Mechanics Measurements, Hemisphere Publishing Co., Washington, D.C., pp. 301-370, 1983.
135. Lissaman, P.B.S., Personal Communication, 1979.
136. Miley, S.J., "An Analysis of the Design of Airfoil Sections for Low Reynolds Numbers," Ph.D. Thesis, Mississippi State University, 1972.
137. Kegelman, J.T., "Experimental Studies of Boundary Layer Transition on a Spinning and Non-Spinning Axisymmetric Body, Ph.D. Thesis, University of Notre Dame, 1982.
138. Bruel and Kjaer, Instructions and Applications-Manual for Condenser Microphones Type 4133/4134, Bruel and Kjaer, 1960.
139. Conigliaro, P.E., "An Experimental Investigation of the Low Reynolds Number Performance of the Lissaman 7769 Airfoil," AIAA Paper No. 83-0647, 1983.
140. Pohlen, L.J., "Experimental Studies of the Effect of Boundary Layer Transition on the Performance of the Miley (M06-13-128) Airfoil at Low Reynolds Numbers," M.S. Thesis, University of Notre Dame, January 1983.
141. Tani, T., and Sato, H., "Boundary-Layer Transition by Roughness Element" Journal of the Physical Society of Japan, Vol. 11, No. 12, pp. 1284-1291, December 1956.
142. Hama, F.R., "An Efficient Tripping Device," Readers Forum, Journal of the Aeronautical Sciences, pp. 236-237, March 1957.
143. Smith, A.M.O., and Clutter, D.W., "The Smallest Height of Roughness Capable of Affecting Boundary-Layer Transition," Journal of the Aero-Space Sciences, pp. 229-256, April 1959.
144. Gibbings, J.C., "On Boundary-Layer Transition Wires," ARC Technical Report C.P. No. 462, London, 1959.
145. Tani, I., "Boundary-Layer Transition," Annual Review of Fluids, pp. 169-196, 1969.
146. Klebanoff, P.S., and Tidstrom, K.D., "Mechanism by Which a Two-Dimensional Roughness Element Induces Boundary-Layer Transition," The Physics of Fluids, Vol. 15, Number 7, pp. 1173-1188, July 1972.

147. Payne, F.M., and Nelson, R.C., "An Experimental Investigation of the Influence of Vertical Wind Shear on the Aerodynamic Characteristics of an Airfoil," AIAA Paper No. 82-0214, January 1982.
148. Nelson, R.C., "The Influence of Airfoil Roughness on the Performance of Flight Vehicles at Low Reynolds Numbers," AIAA Paper No. 84-0540, January 1984.
149. Jones, R., and Williams, D.H., "The Effect of Surface Roughness on the Characteristics of the Aerofoils NACA 0012 and RAF 34, ARC R&M No. 1708, February 1936.
150. Erlich, E., and Pinoteau, M., "The Use of Roughness to Trigger Off Transition in a Bubble at the Leading Edge of an Airfoil at High Incidences," paper presented to the Supersonic Wind Tunnel Association, 35th Meeting, March 1971.
151. Bertelrud, A.A., "A Literature Survey of Surface Roughness Effects on the Drag of Subsonic Aircraft," Aeronautical Research Council of Sweden Technical Note All-1224, Stockholm, 1978.
152. Pressnell, M.S., and Bakin, M.S.B., "Aerofoil Turbulator and Invigorators," National Free-Flight Society of America, Annual Symposium Report, 1982.
153. Sivaramakrishnan, M.M., and Pfenninger, W., "Wind Tunnel Tests on a High Performance Low Reynolds Number Airfoil," AIAA Paper No. 84-0628, 1984.
154. Huber II, A.F., "Influence of Surface Roughness on Airfoils at Low Reynolds Number," M.S. Thesis, University of Notre Dame, in progress.
155. Bastedo, W.G., "Three Dimensional Effects on Low Reynolds Number Airfoil and Wing Performance," M.S. Thesis, University of Notre Dame, in progress.
156. Loving, D.L., and Katzoff, S., "The Fluorescent Oil Film Method and Other Techniques for Boundary-Layer Flow Visualization," NASA Memo 3-17-59L, 1959.
157. Winkelmann, A.E., Ngo, H.T., and deSeite, R.C., "Some Observations of Separated Flow on Finite Wings," AIAA Paper No. 82-0346, 1982.
158. Winkelmann, A.E., "On the Occurance of Mushroomed Shaped Stall Cells in Separated Flow," AIAA Paper No. 83-1734, 1983.
159. Montoya, L.C., Bikle, P.F., and Banner, R.D., "Section Drag Coefficients from Pressure Probe Traverses of a Wing Wake at Low Speeds," AIAA Paper No. 78-1479, presented at the AIAA Aircraft Systems and Technology Meeting, Los Angeles, CA, August 21-23, 1978.
160. Bowers, A.H., and Sims, A.G., unpublished data, 1983.
161. Jenkins, M.W.M., "In-Flight Research -at Low Cost," Lockheed Horizons, pp. 32-39, Spring 1981.
162. Hall, D.W., Fortenbach, C.D., Dimiceli, E.V., and Parks, R.W., "A Preliminary Study of Solar Powered Aircraft and Associated Power Trains," NASA CR 3699, December 1983.
163. Hall, D.W., and Hall, S.A., "Structural Sizing of Solar Powered Aircraft," NASA CR 172313, April 1984.
164. Youngblood, J.W., Talay, T.A., and Pegg, R.J., "Design of Long-Endurance Unmanned Airplanes Incorporating Solar and Fuel Cell Propulsion," AIAA Paper No. 84-1430, June 1984.
165. Larrabee, E.E., "Five Years Experience with Minimum Induced Loss Propellers -Part I, Theory and Part II -Application," SAE Paper Numbers 840026 and 840027, February 1984.
166. Sheldahl, R.E., and Klimas, P.C., "Aerodynamic Characteristics of Seven Symmetrical Airfoil Sections Through 180 Degree Angle of Attack for Use in Aerodynamic Analysis of Vertical Axis Wind Turbines," Sandia National Laboratories, SAND80-2114, UC-60, March 1981.
167. Strickland, J.H., "The Darrieus Turbine: A Performance Prediction Model Using Multiple Streamtubes," Sandia Laboratory Report SAND75-0431, October 1975.
168. Brendel, M., Preliminary Full Range Data for Wortmann FX 63-137 for use in VAWT Performance Prediction Code, unpublished data, University of Notre Dame, April 1984.

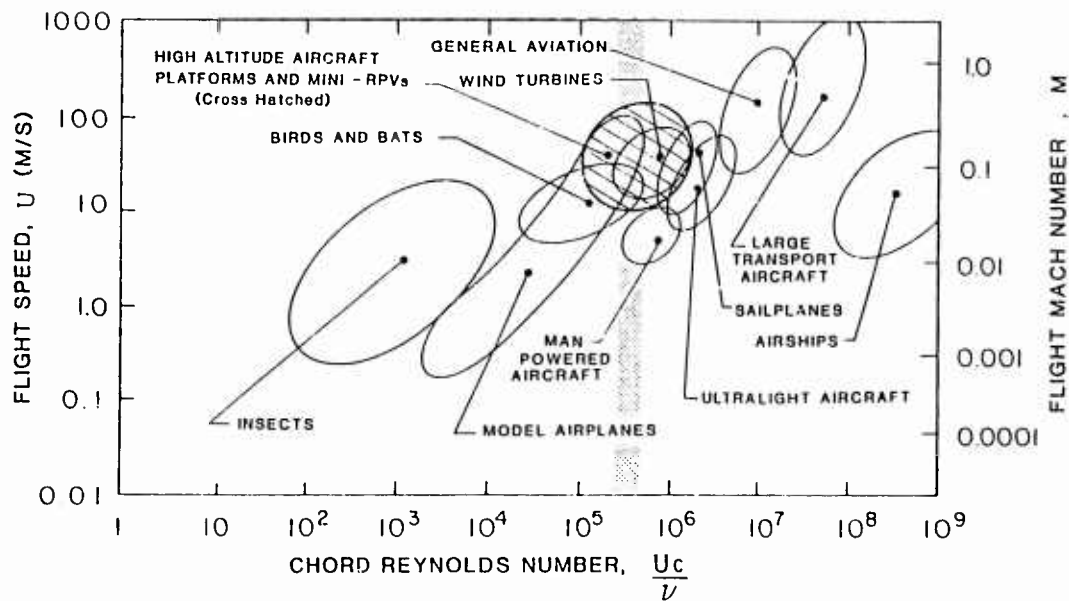


Figure 1. Chord Reynolds Number versus Flight Velocity for a Variety of Natural and Man-Made Flying Objects, Adapted From References 3 and 4. (All values based on standard sea level conditions except the high altitude aircraft platforms where values were based on conditions at about 70,000 feet).

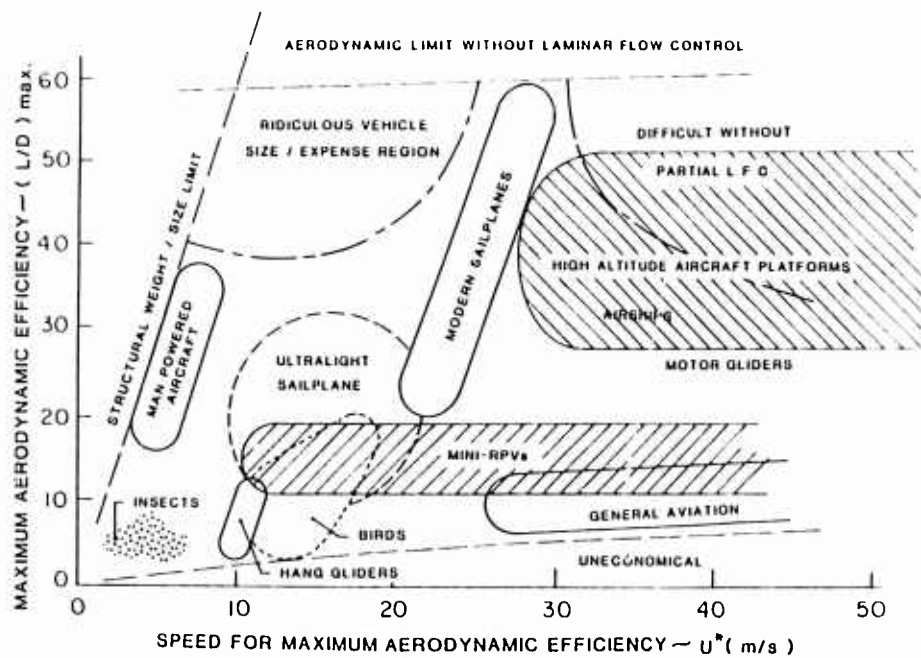


Figure 2. Maximum Aerodynamic Efficiency versus Speed for a Variety of Natural and Man-Made Flying Objects - Adapted from Reference 4. (The Shaded Regions Represent Estimates for HAAPs and Mini-RPVs).

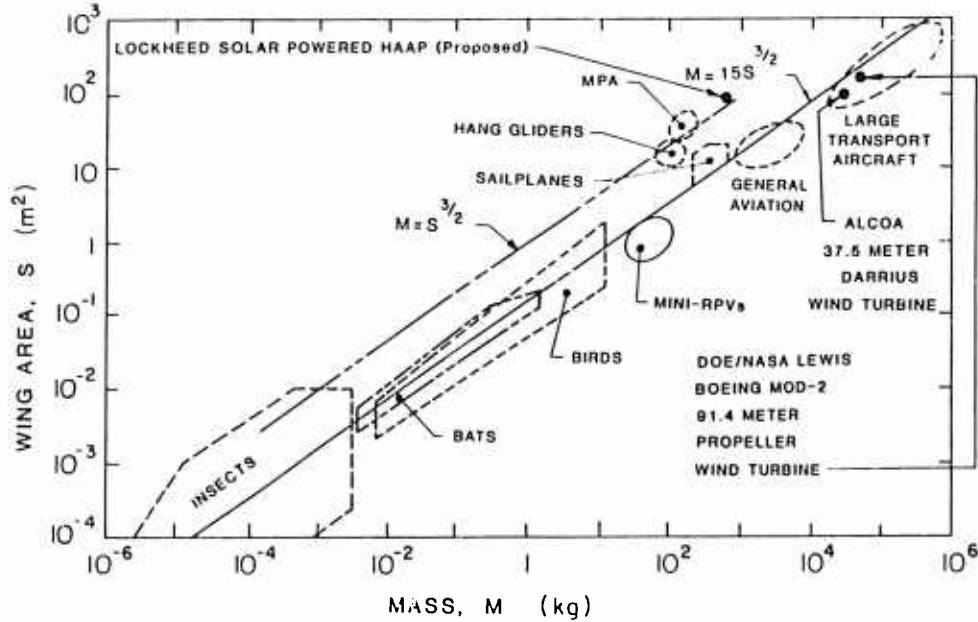


Figure 3. Wing Area Versus Mass for a Variety of Natural and Man-Made Flying Objects (Reference 30).

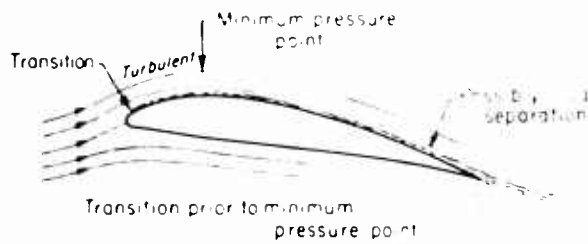


Figure 4. High Reynolds Number Flow Over a Large Aircraft Wing.

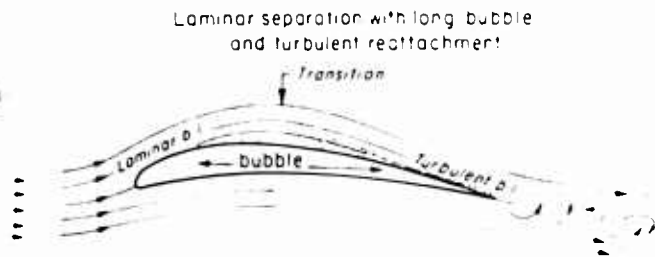


Figure 5. Low Reynolds Number Flow Over a Small RPV Wing at a Small Angle of Attack.

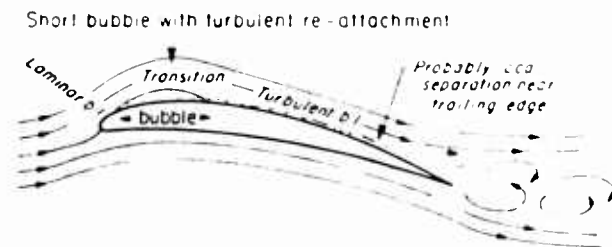


Figure 6. Low Reynolds Number Flow Over a Small RPV Wing at a Large Angle of Attack (Chordwise Length of Separation Bubble Greatly Exaggerated).



Figure 7. Low Reynolds Number Flow Over a Small RPV Wing at Stall.

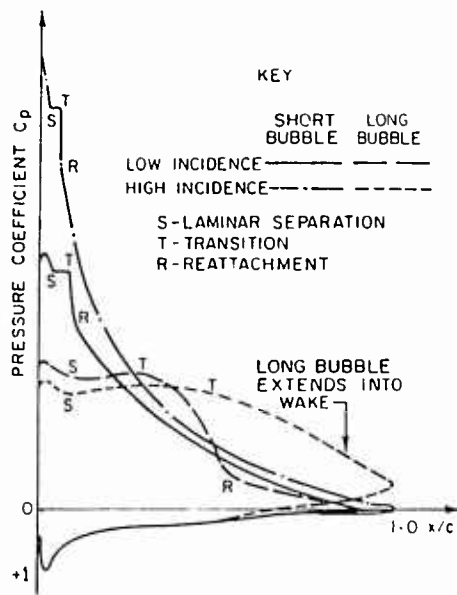


Figure 8. Effect of Long and Short Separation Bubbles on the Pressure Distribution Over an Airfoil at High Reynolds Number (Reference 41).

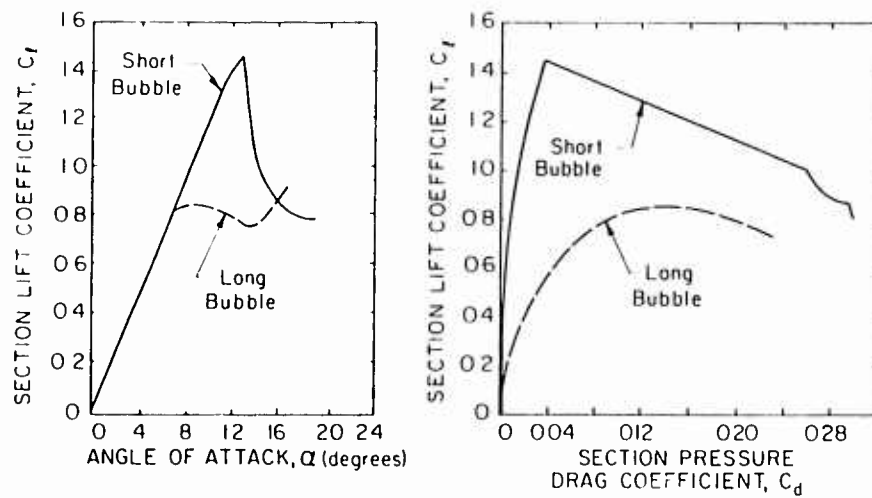


Figure 9. The Effect of Short and Long Bubbles on Airfoil Performance at High Reynolds Number (Reference 42).

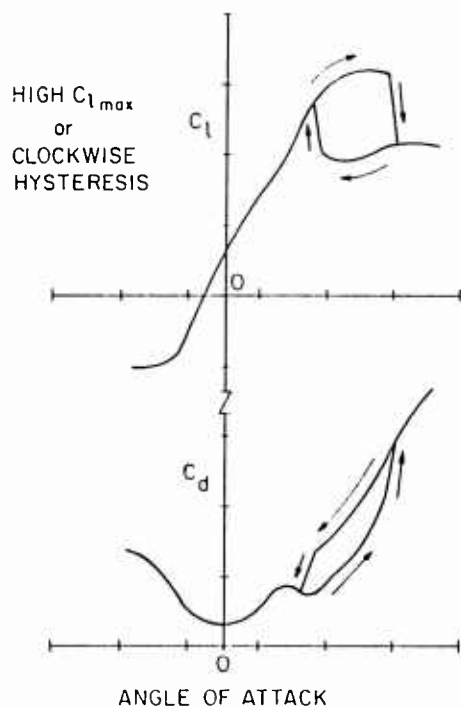


Figure 10. Airfoil Section Lift and Drag Coefficients versus Angle of Attack Showing the "High $C_{l\max}$ " or "Clockwise" Hysteresis.

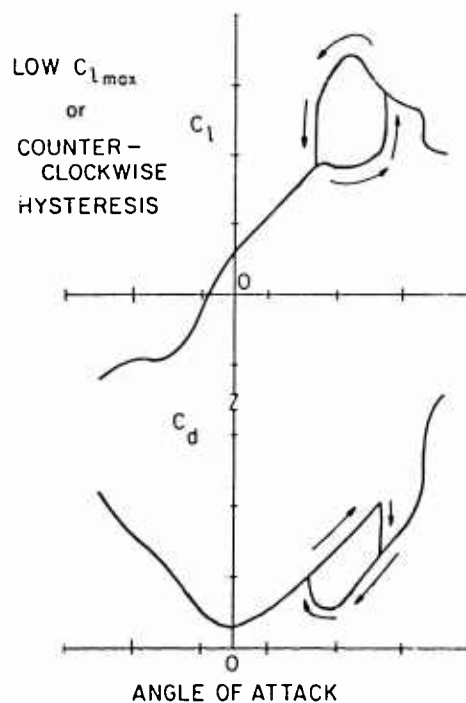


Figure 11. Airfoil Section Lift and Drag Coefficients versus Angle of Attack Showing the "Low $C_{l\max}$ " or "Counterclockwise" Hysteresis.

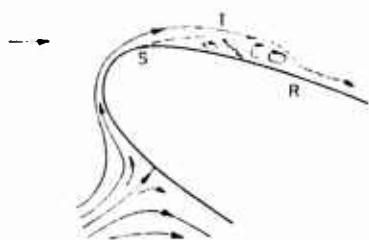


Figure 12. Sketch of Laminar Separation and Turbulent Reattachment Near the Leading Edge of an Airfoil.

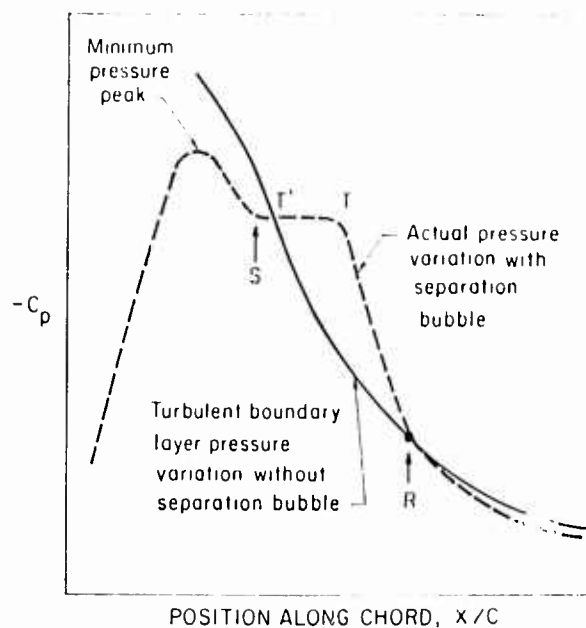


Figure 13. Typical Surface Pressure Distribution With and Without a Separation Bubble.

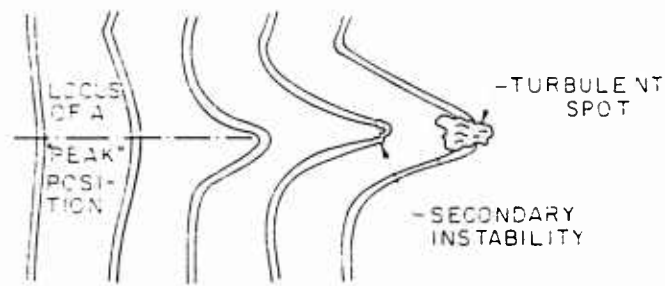
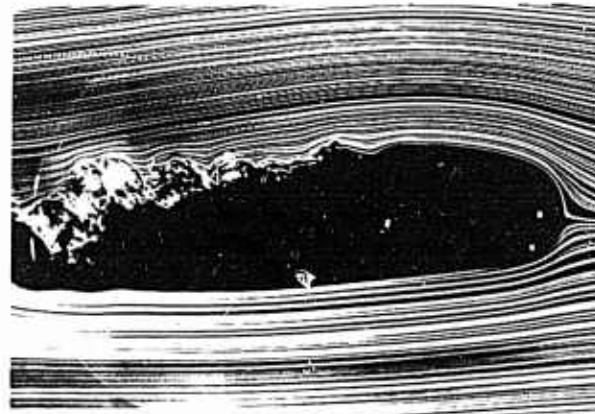
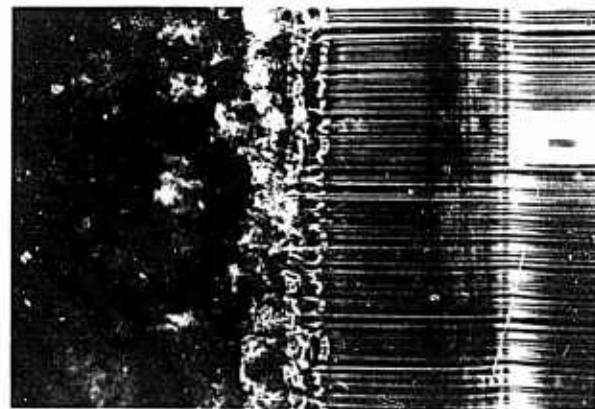


Figure 14. Successive Locations of Wave Fronts in the Later Stages of Transition (Taken from Reference 89).



a) Profile View



b) Plan View

Figure 15. University of Notre Dame Photographs of Smoke Filaments Generated by the Smoke-wire Technique for a Cylindrical Leading Edge-Constant Thickness Model at 6° Angle of Attack and $R_c < 100,000$ (Air flow from right to left)



Figure 16. Flow About an NACA 23012 Airfoil at an Angle of Attack of 14 Degrees and a Reynolds Number of 123,800 (From Reference 102).

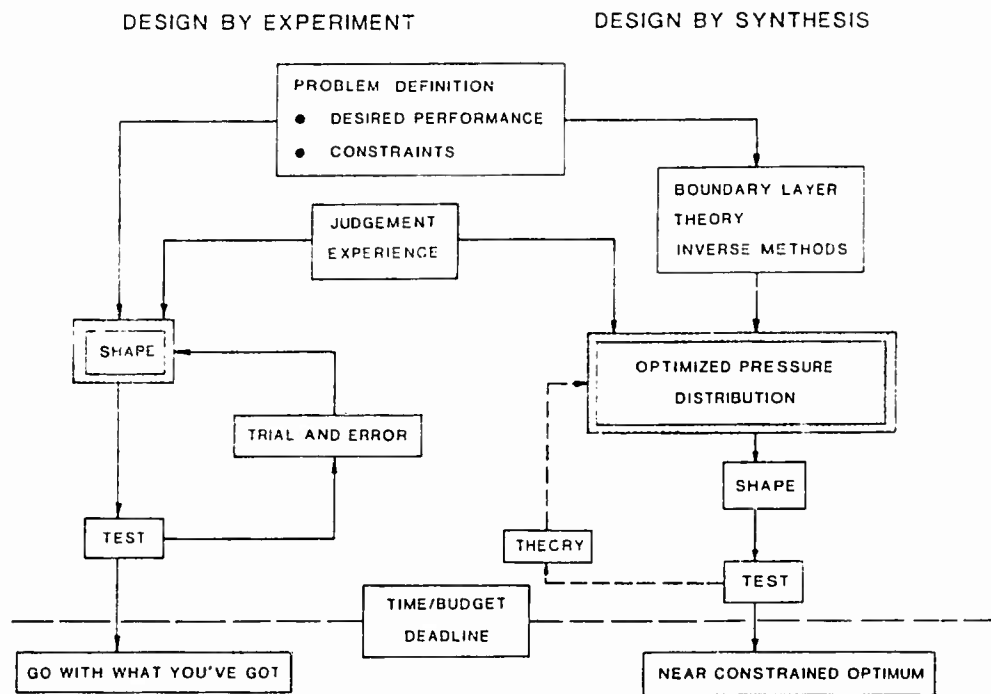
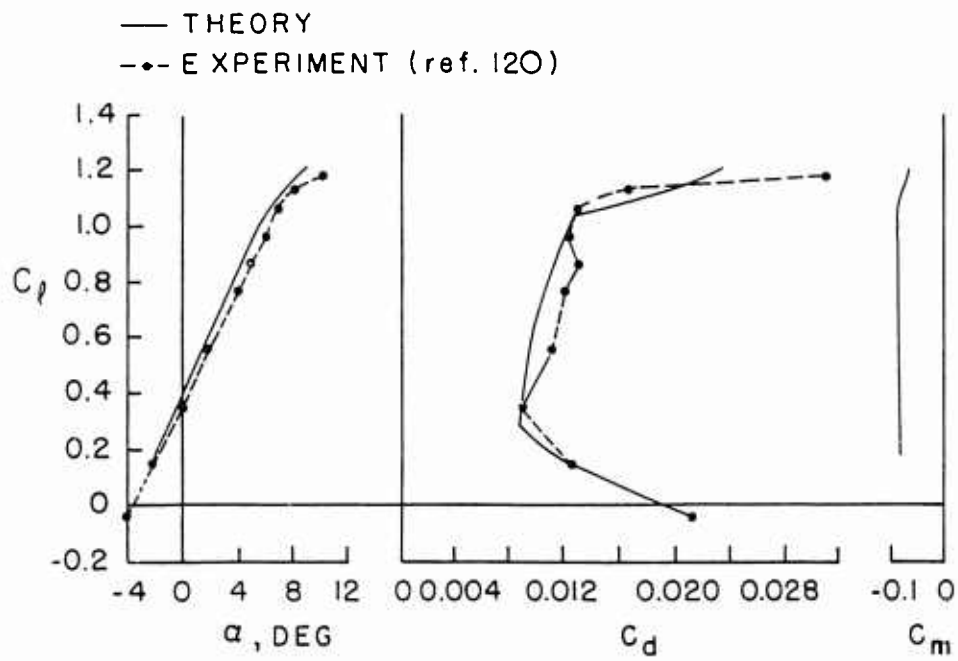
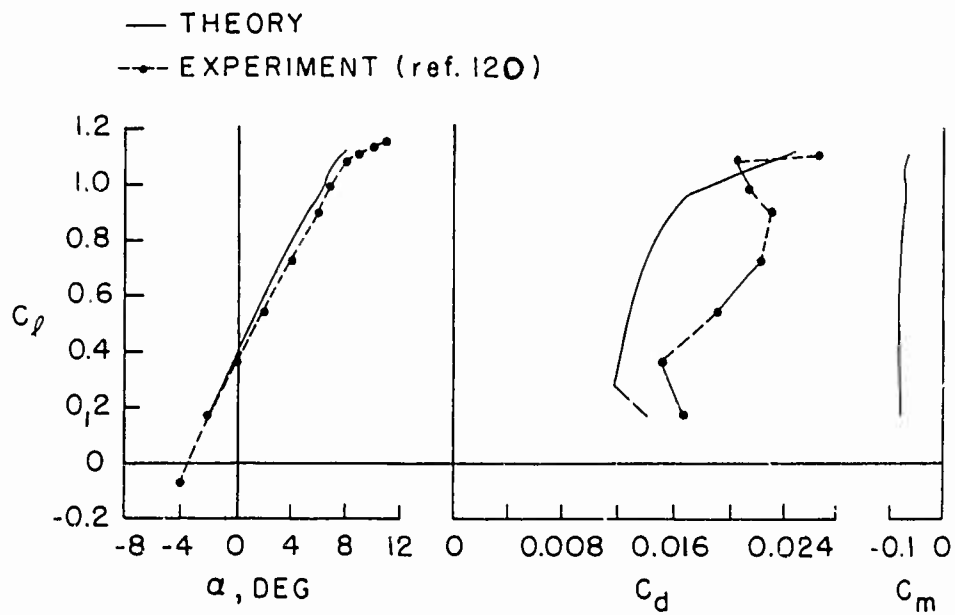


Figure 17. Airfoil Section Design Procedure (Reference 4).



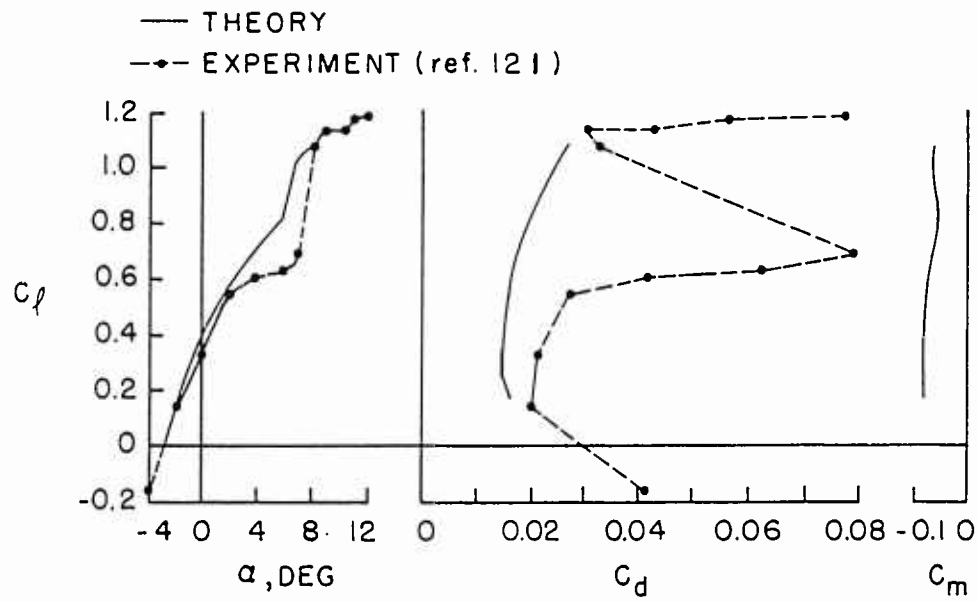
a) $R_C = 200,000$

Figure 18. Comparison of Theoretical and Experimental Section Characteristics of the EPPLER 387 Airfoil (Reference 120).



b) $R_C = 100,000$

Figure 18. Continued



c) $R_c = 60,000$

Figure 18. Continued

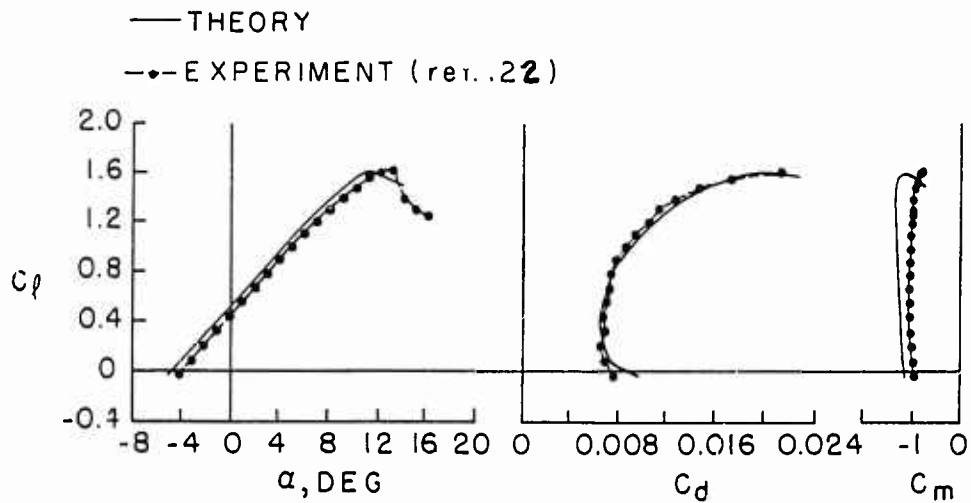


Figure 19. Comparison of Theoretical and Experimental Section Characteristics of NASA NLF(1)-0416 Airfoil for Reynolds Number Equal to 2×10^6 (Reference 121).

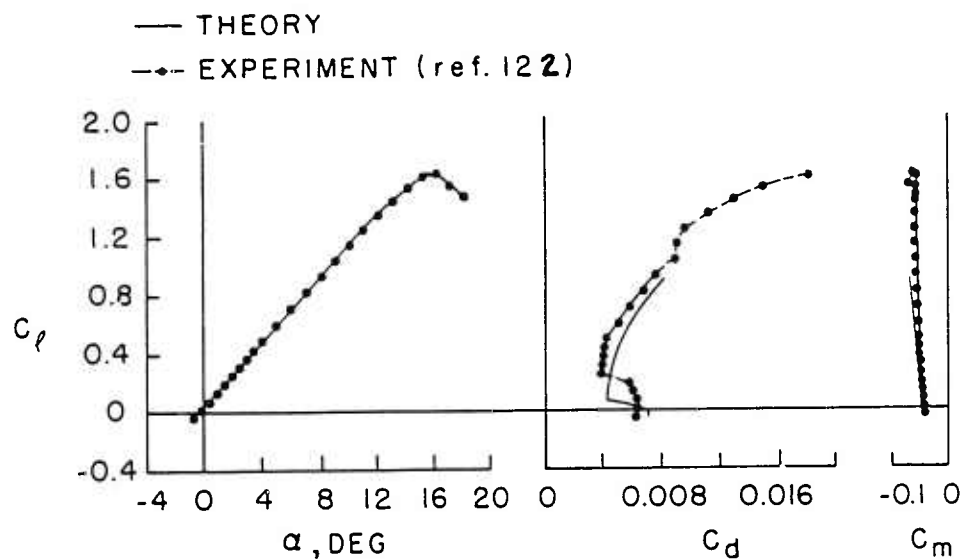


Figure 20. Comparison of Theoretical and Experimental Section Characteristics of NASA NLF(1)-0416 Airfoil for Reynolds Number Equal to 9×10^6 and Simple Flap Deflection of -10° (Reference 122).

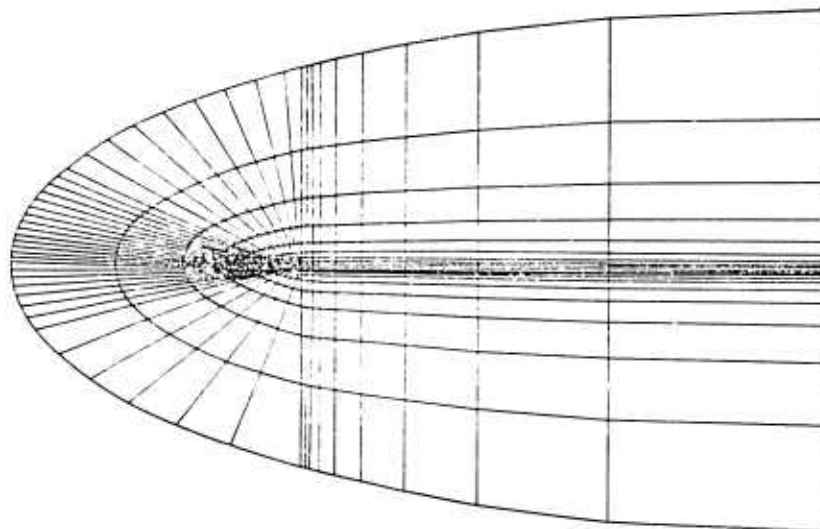


Figure 21. Entire View of the Computational Grid Used for the Miley Airfoil and for $R_c = 100,000$ and $M = 0.5$ (Reference 123).

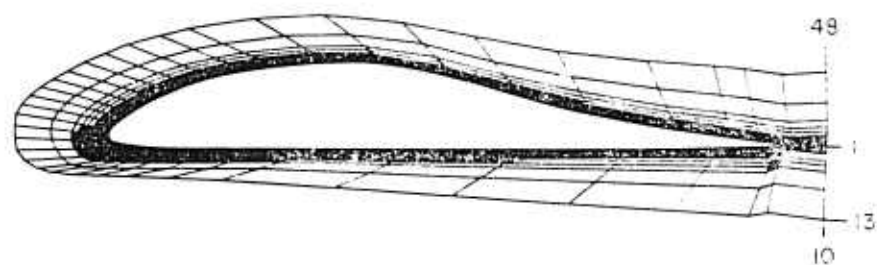


Figure 22. Computational Grid Used Near the Miley Airfoil for $R_c = 100,000$ and $M = 0.5$.

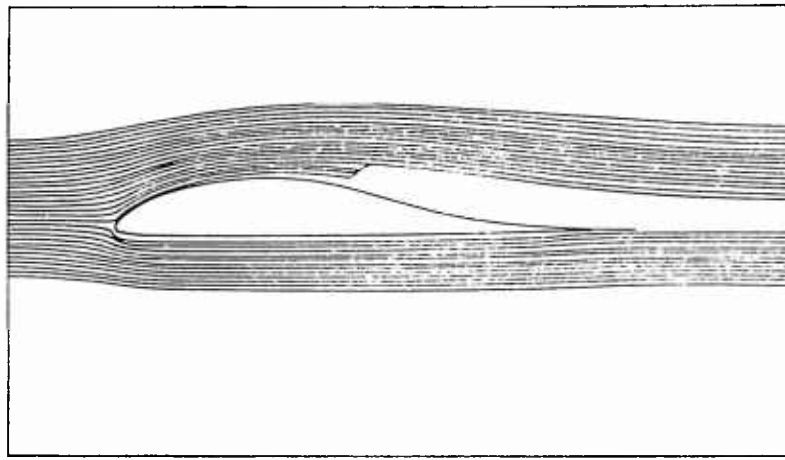


Figure 23. Plot of Computed Streamlines for the Miley Airfoil at $\alpha = 0^\circ$, $Re = 100,000$, and $M = 0.5$ (Reference 123).

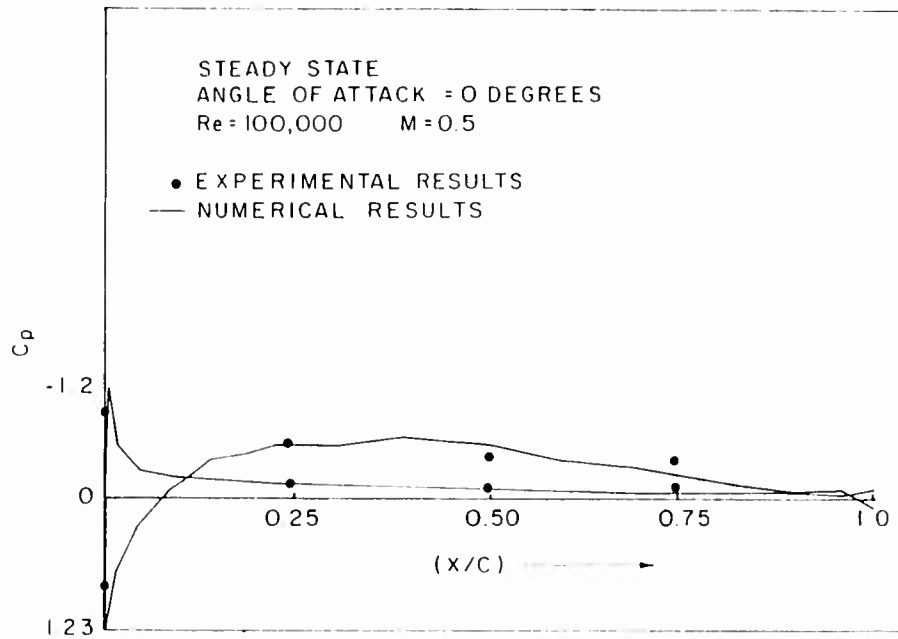


Figure 24. Pressure Coefficient Versus Position Along the Chord of the Miley Airfoil (Reference 123).

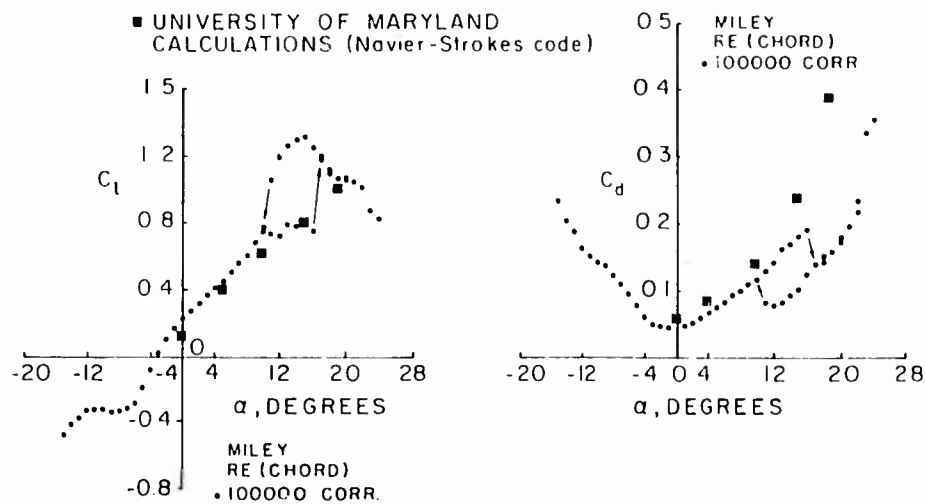


Figure 25. Section Lift and Drag Coefficients Versus Angle of Attack: Corrected for Blockage $Re = 100,000$; One Flow Restrictor (Reference 140).

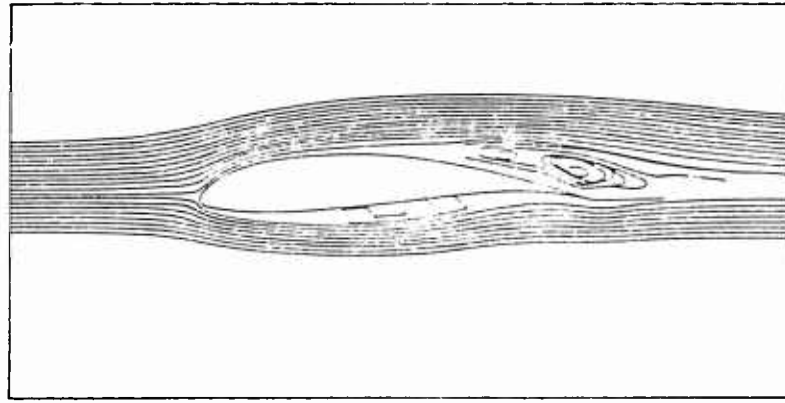


Figure 26. Plot of Computed Streamlines for the Wortmann FX 63-137 Airfoil at $\alpha = 0^\circ$, $R_C = 100,000$, and $M = 0.5$ (Reference 123).

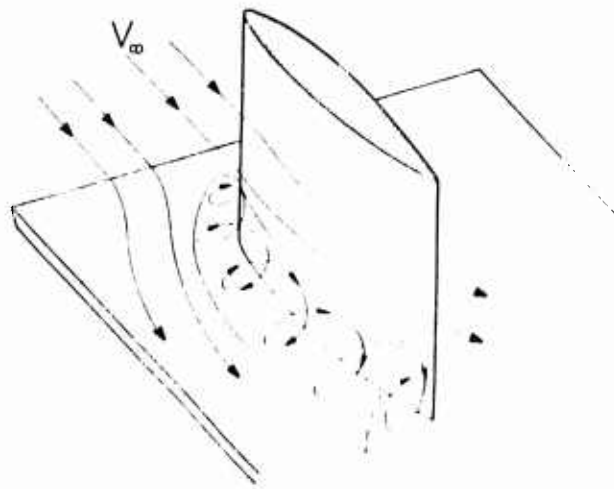


Figure 27. Sketch Indicating the Three-Dimensional Corner Type of Flow Near the Airfoil and the Side Plate.

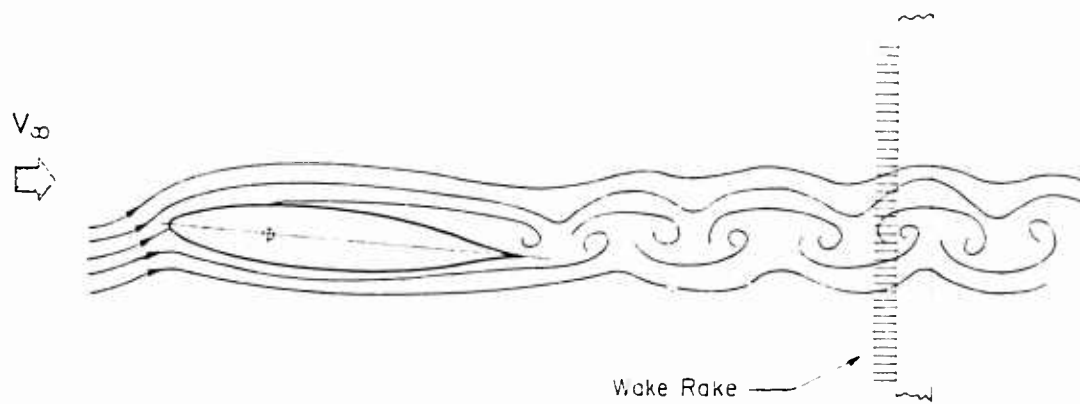


Figure 28. Unsteady Wake Produced Behind a NACA 663-018 Airfoil at 6° Angle of Attack and $R_C = 40,000$ (flow pattern sketched from smoke visualization photograph).

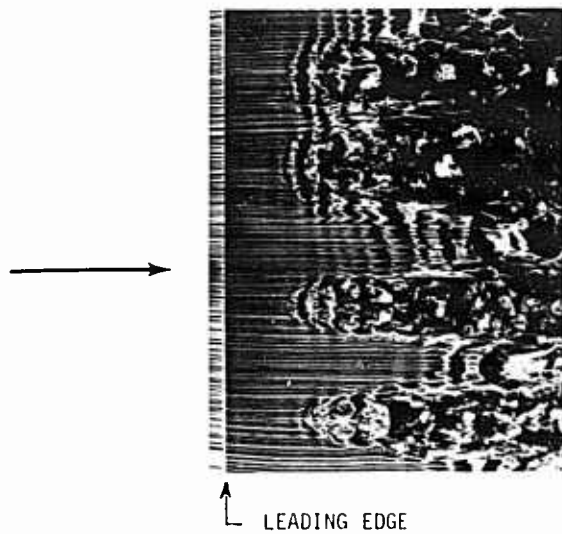


Figure 29. Smoke-Wire Visualization for the NACA 663-018 Airfoil Showing the Spanwise Flow Structure at $R_c = 55,000$ and $\alpha = 8^\circ$ (Reference 92).

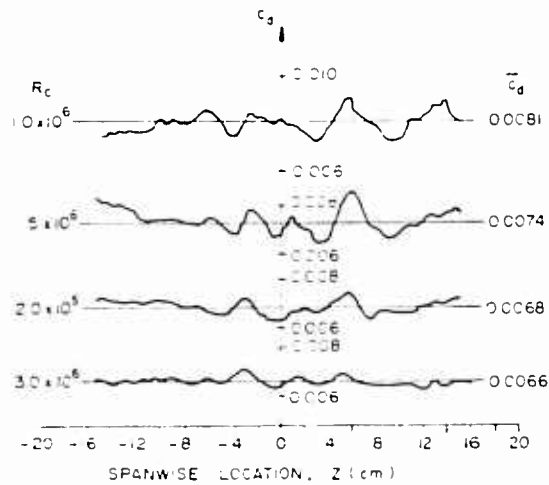


Figure 30. Section Profile-Drag Coefficient in the Spanwise Direction Using an Integrating Rake (adapted from Althaus Reference 129).

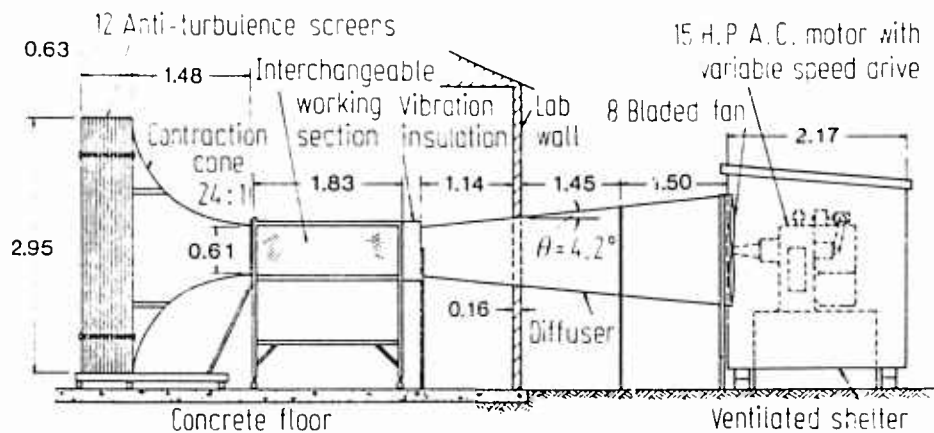


Figure 31. Low Turbulence Subsonic Wind Tunnel.

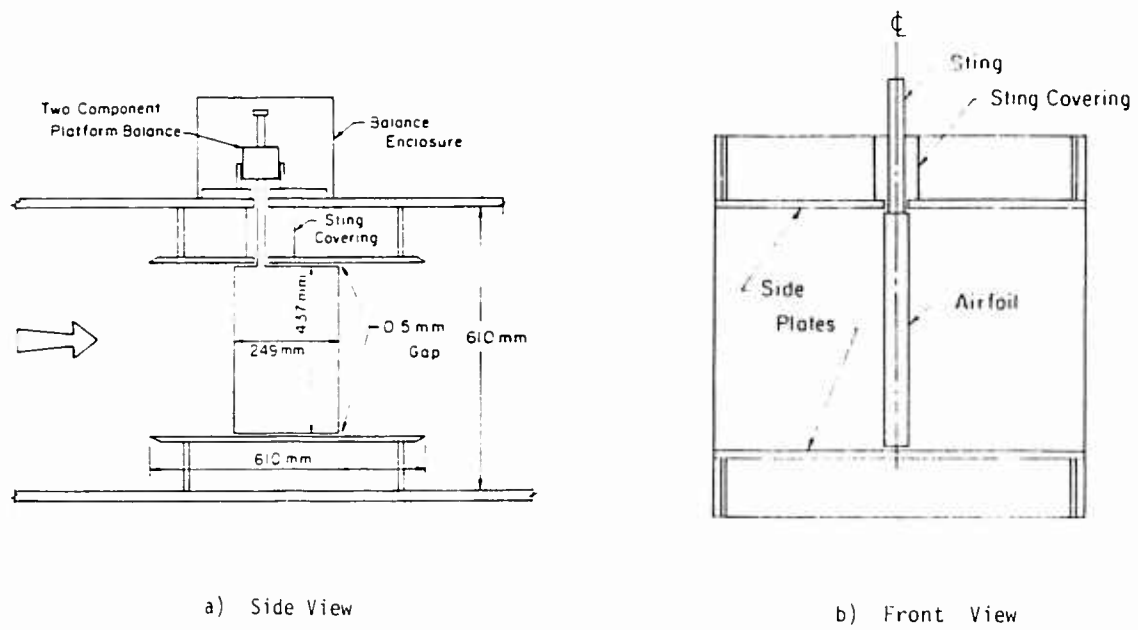


Figure 32. Test Section with One Piece Airfoil Model.

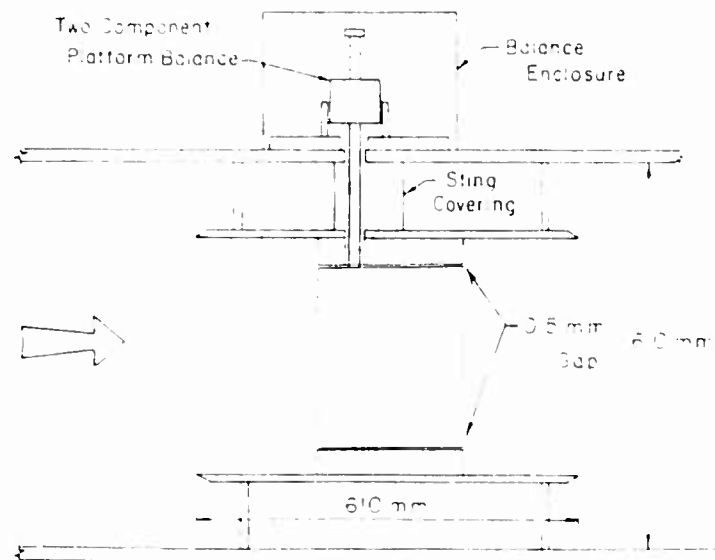
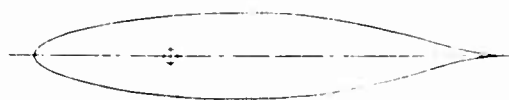


Figure 33. Side View of Test Section with Three Piece Airfoil Model.

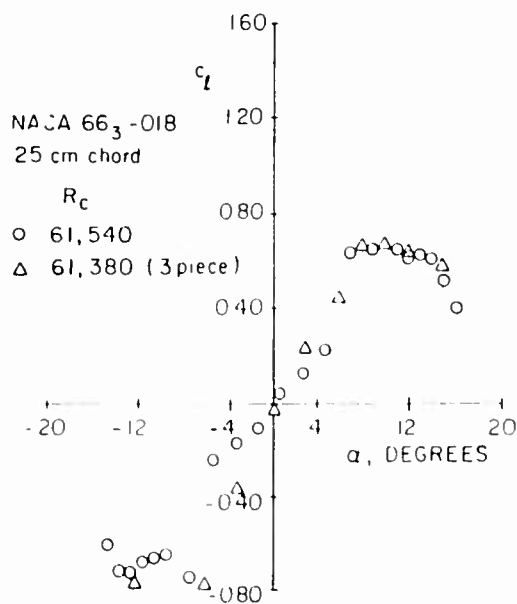


a) NACA 663-018

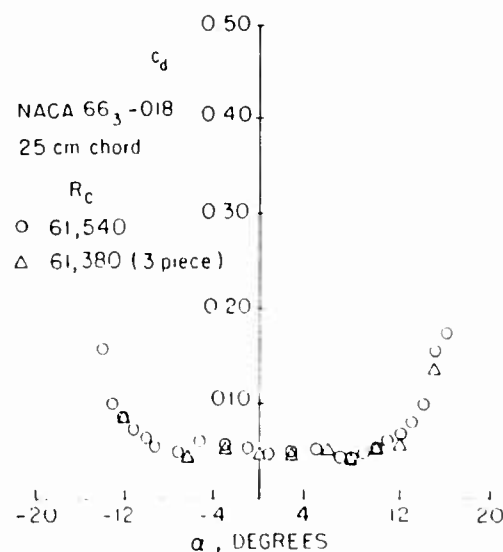


b) EPPLER 61

Figure 34. Airfoil Geometries

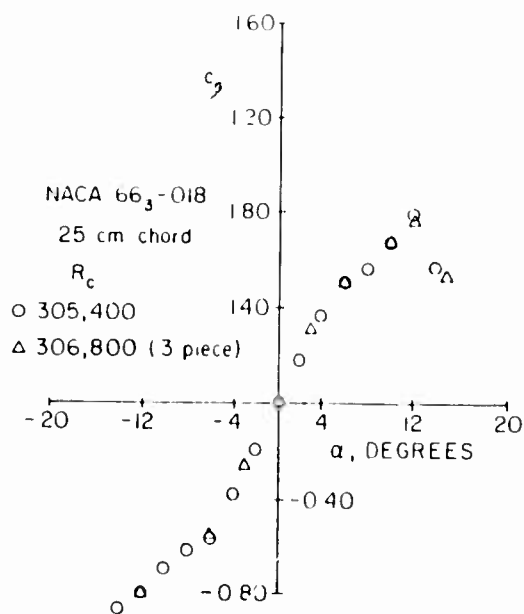


a) Section Lift Coefficient

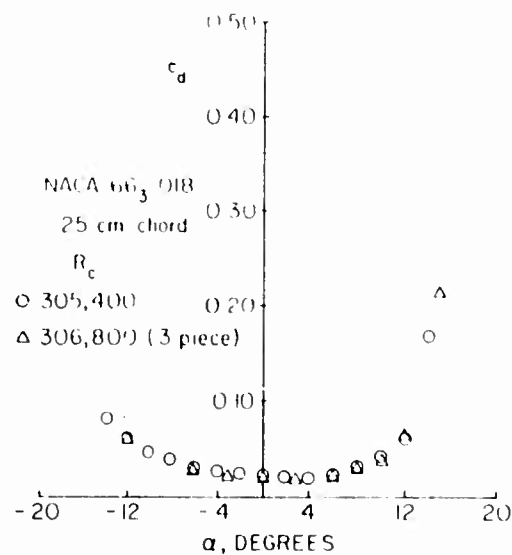


b) Section Profile Drag Coefficient

Figure 35. Comparison of Lift and Drag Data Coefficients for the One Piece and the Three Piece Airfoil Models at $R_c = 61,400$ (Reference 127).



a) Section Lift Coefficient



b) Section Profile Drag Coefficient

Figure 36. Comparison of Lift and Drag Data Coefficients for the One Piece and the Three Piece Airfoil Models at $R_c = 306,000$ (Reference 127).

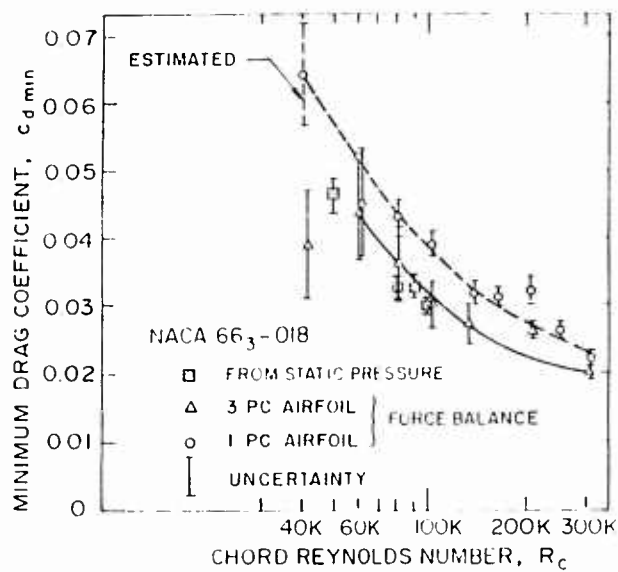


Figure 37. Minimum Section Profile/Drag Coefficient versus Chord Reynolds Number (Reference 140).

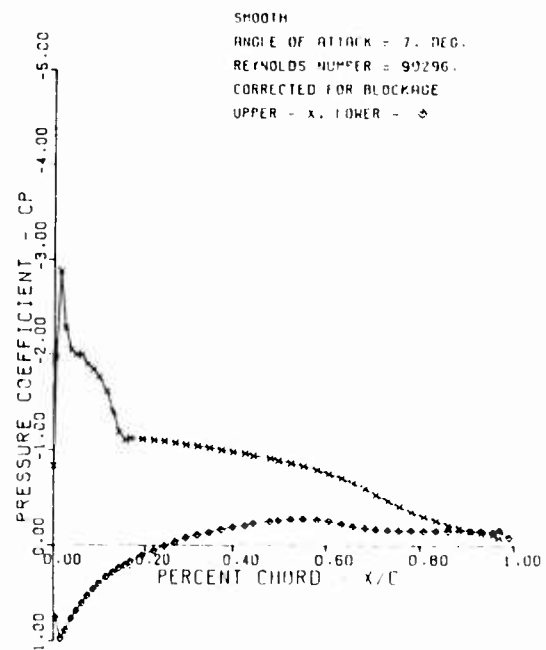


Figure 38. Experimental Static Pressure Distribution for the NACA 663-018 Airfoil at $R_c = 90,286$ and $\alpha = 7^\circ$.

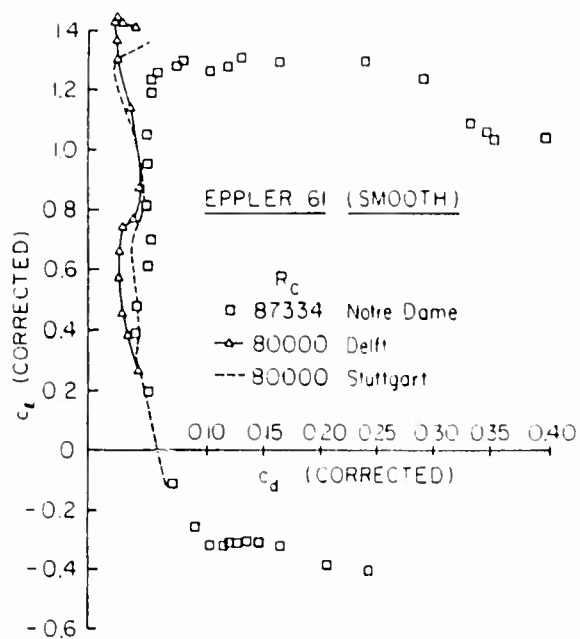


Figure 39. Comparison of Lift Coefficient Data at $R_c = 80,000$ for the Eppler 61 Airfoil (Reference 60).

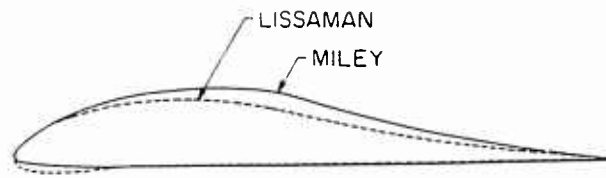


Figure 40. Lissaman 7769 and Miley M06-13-128 Airfoil Geometries.

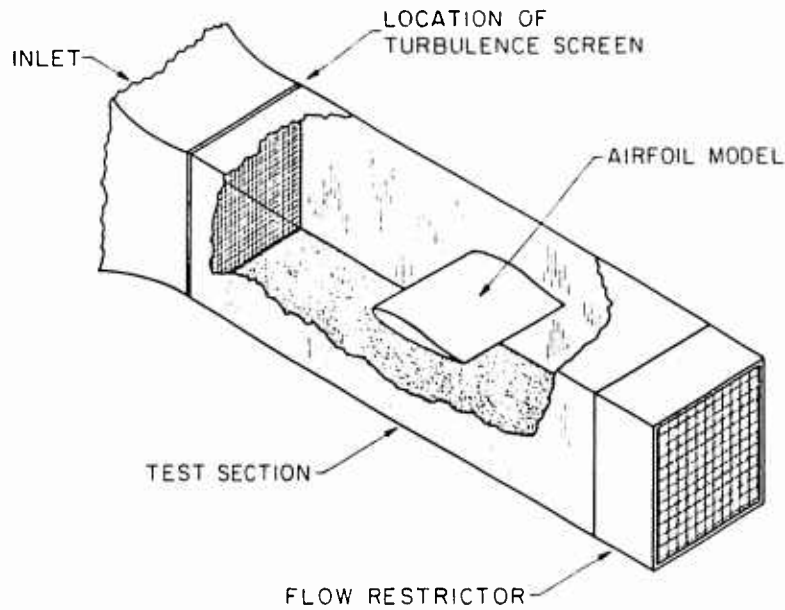


Figure 41. Test Section Showing the Turbulence Screen and Flow Restrictor Locations (airfoil side plates not shown).

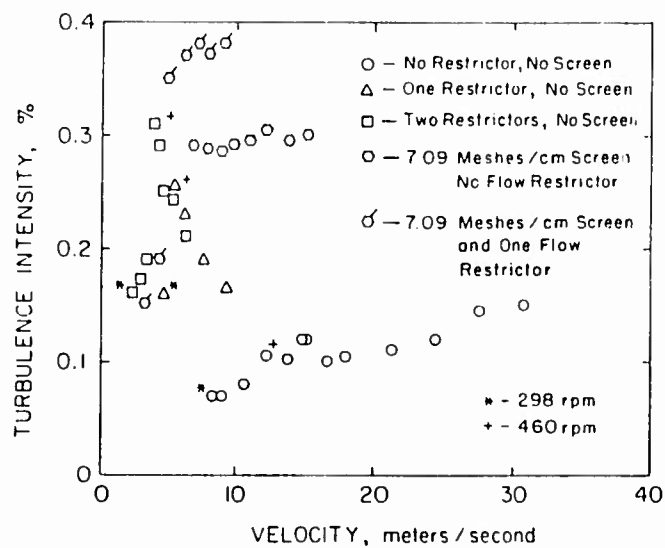


Figure 42. Turbulence Intensity versus Tunnel Velocity With and Without Flow Restrictors and Screen.

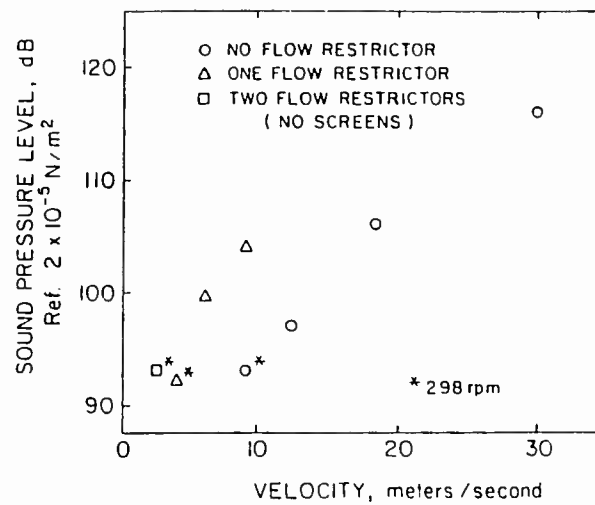


Figure 43. Sound Pressure Level versus Tunnel Velocity With and Without Flow Restrictors.

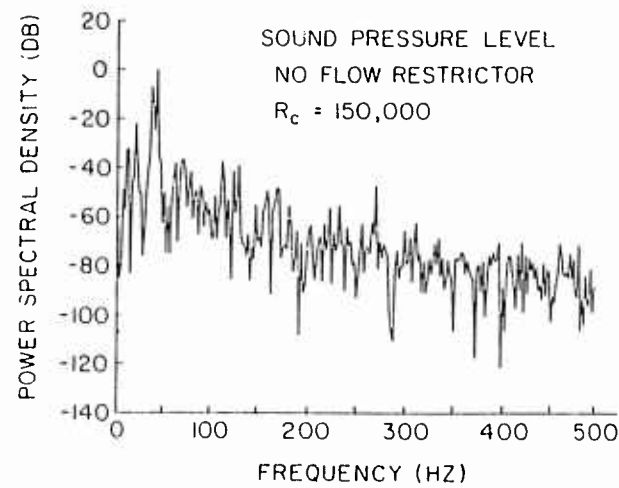


Figure 44. Power Spectral Density versus Frequency at $x = 68 \text{ cm}$, $U = 9 \text{ m/s}$, and No Flow Restrictor From Sound Measurements.

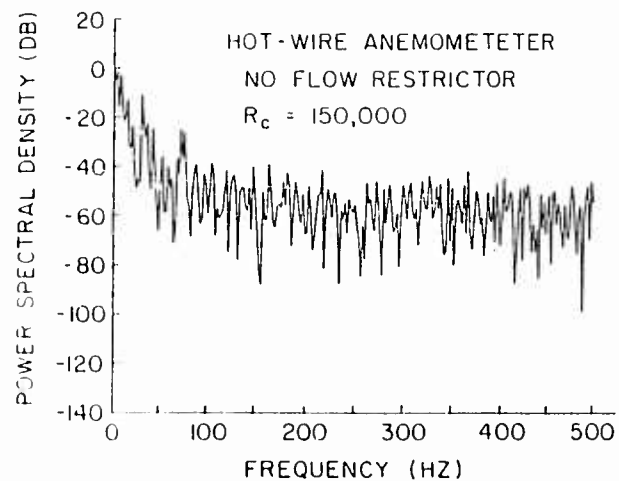


Figure 45. Power Spectral Density versus Frequency at $x = 68 \text{ cm}$, $U = 9 \text{ m/s}$, and No Flow Restrictor From Hot-Wire Anemometer.

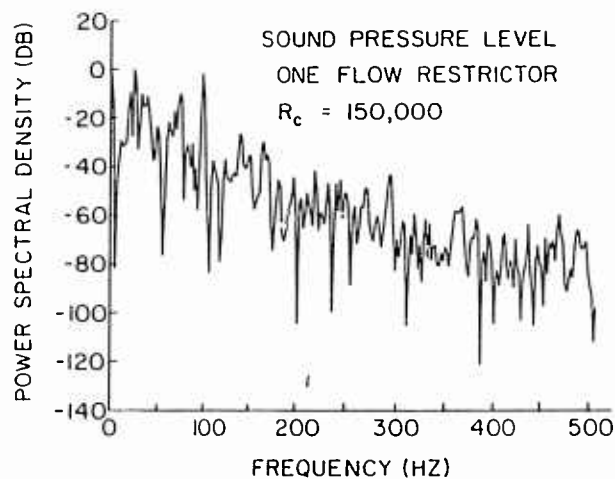


Figure 46. Power Spectral Density versus Frequency at $x = 68$ cm, $U = 9$ m/s and One Flow Restrictor From Sound Measurements.

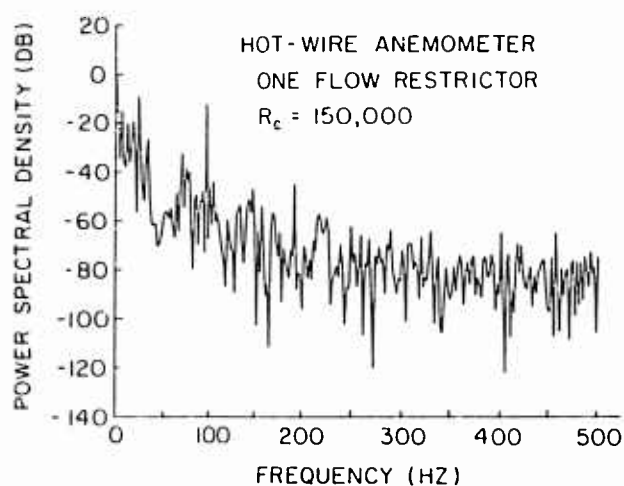


Figure 47. Power Spectral Density versus Frequency at $x = 68$ cm, $U = 9$ m/s and One Flow Restrictor From Hot-Wire Anemometer.

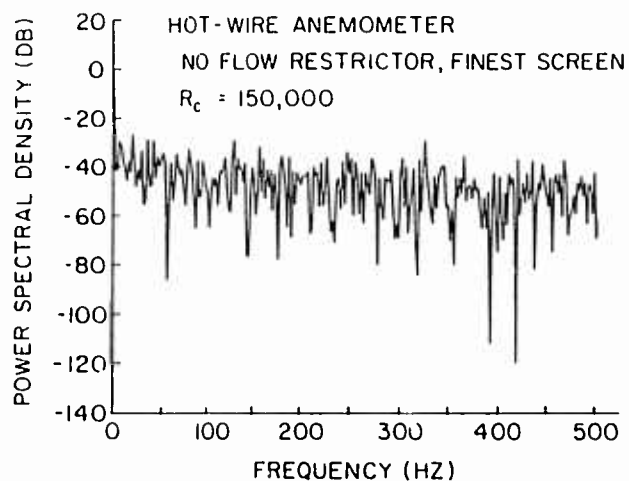


Figure 48. Power Spectral Density versus Frequency at $x = 68$ cm, $U = 9$ m/s, No Flow Restrictor and One 7.09 meshes/cm Screen From Hot-Wire Anemometer.

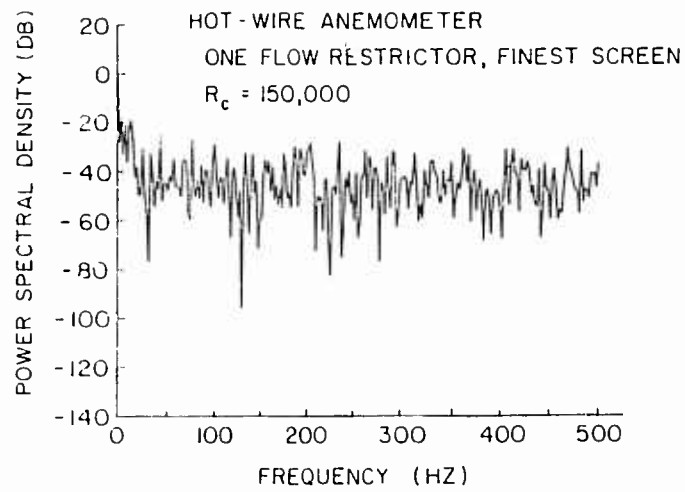


Figure 49. Power Spectral Density versus Frequency at $x = 68$ cm, $U = 9$ m/s, One Flow Restrictor and One 7.09 meshes/cm Screen From Hot-Wire Anemometer.

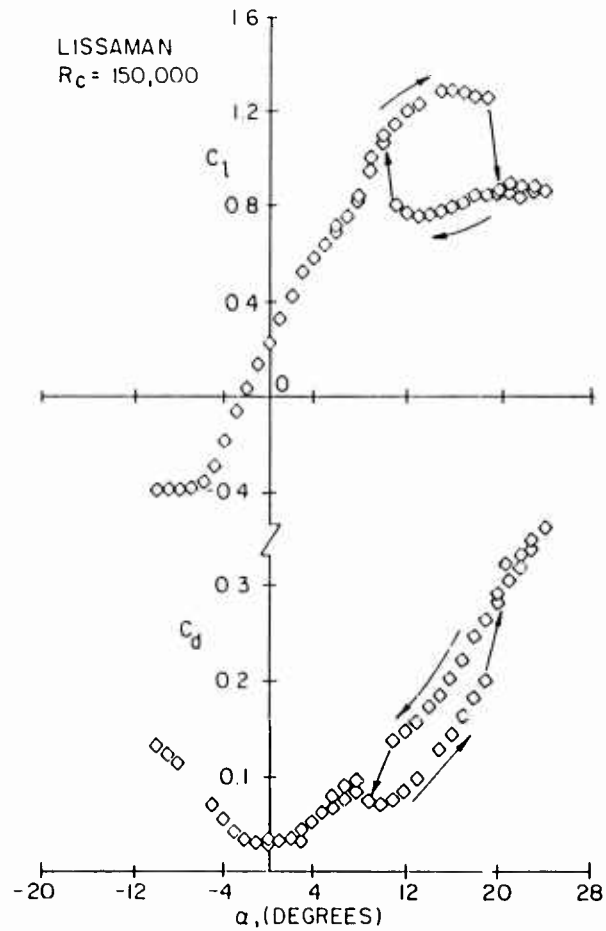
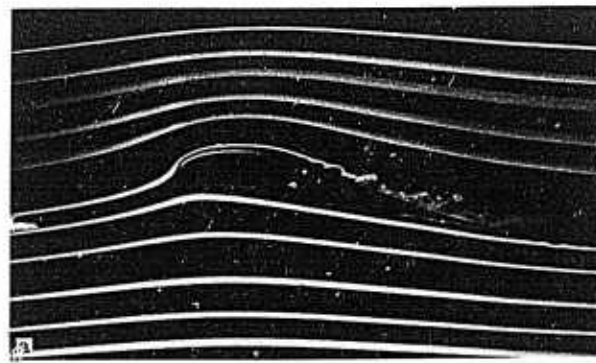


Figure 50. Lift and Drag Coefficients versus Angle of Attack of the Smooth Lissaman Airfoil with No Screen or Flow Restrictor (Hysteresis)



a) Increasing Angle of Attack



b) Decreasing Angle of Attack

Figure 51. Smoke Photographs of the Lissaman Airfoil at $R_C = 50,000$ at 12° Angle of Attack with No Flow Restrictor or Screen

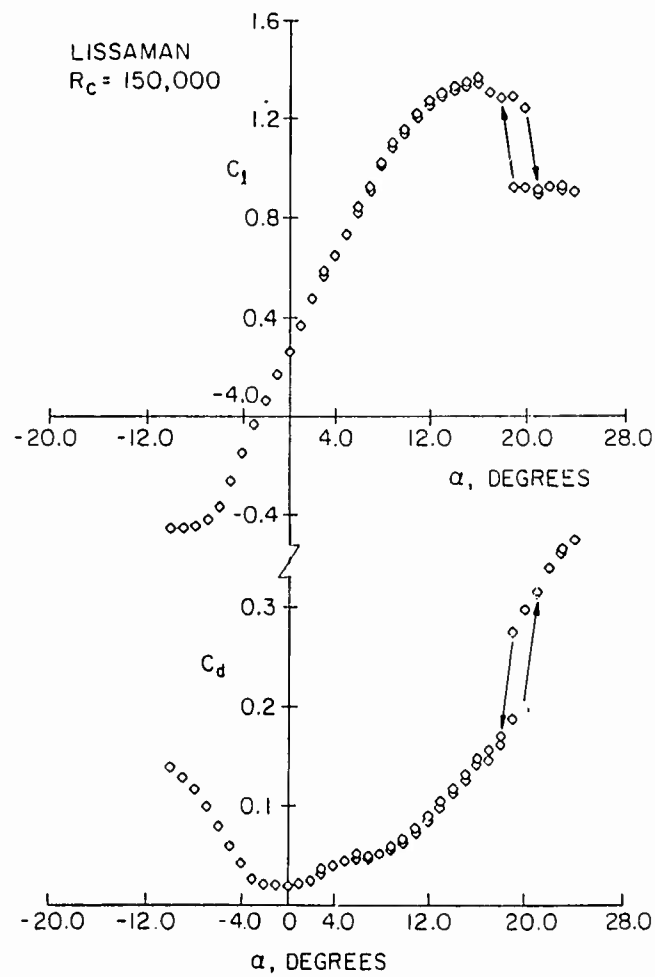


Figure 52. Lift and Drag Coefficients versus Angle of Attack for the Smooth Lissaman Airfoil with No Screen and One Flow Restrictor

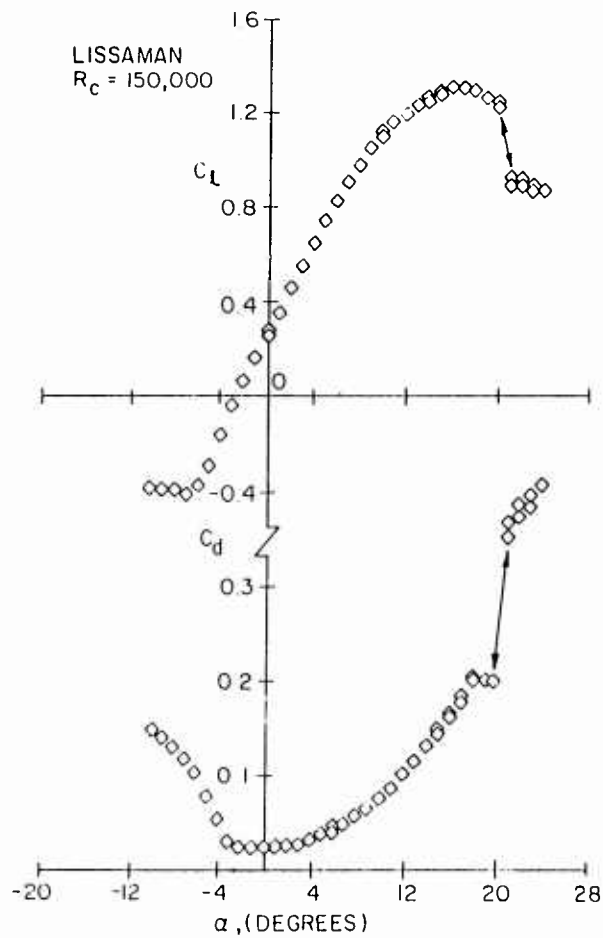


Figure 53. Lift and Drag Coefficients versus Angle of Attack for the Smooth Lissaman Airfoil with One 7.09 meshes/cm Screen and No Flow Restrictor

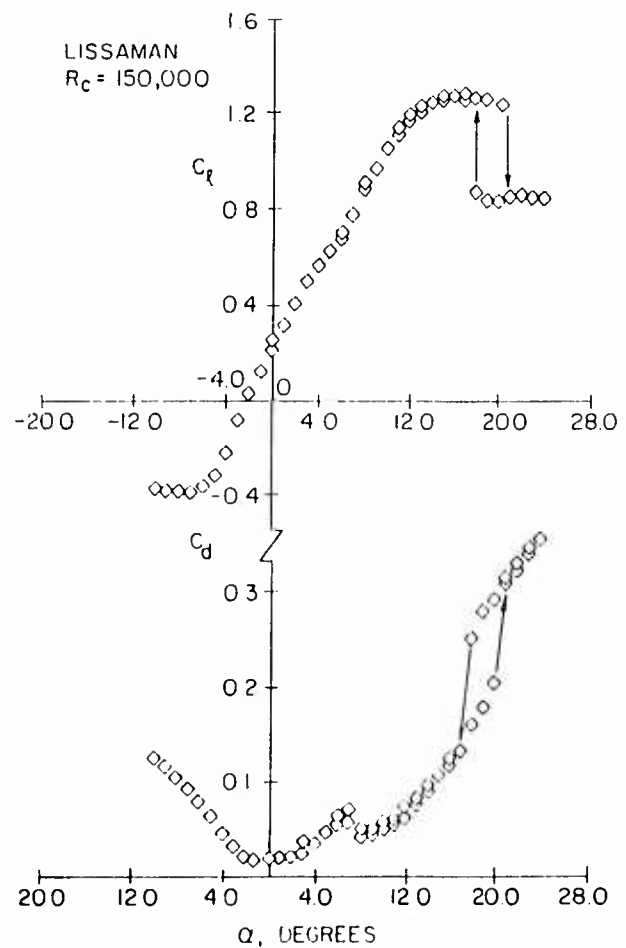


Figure 54. Lift and Drag Coefficients versus Angle of Attack for the Lissaman Airfoil with Tape Trip at 1.1% Chord and No Screen or Flow Restrictor

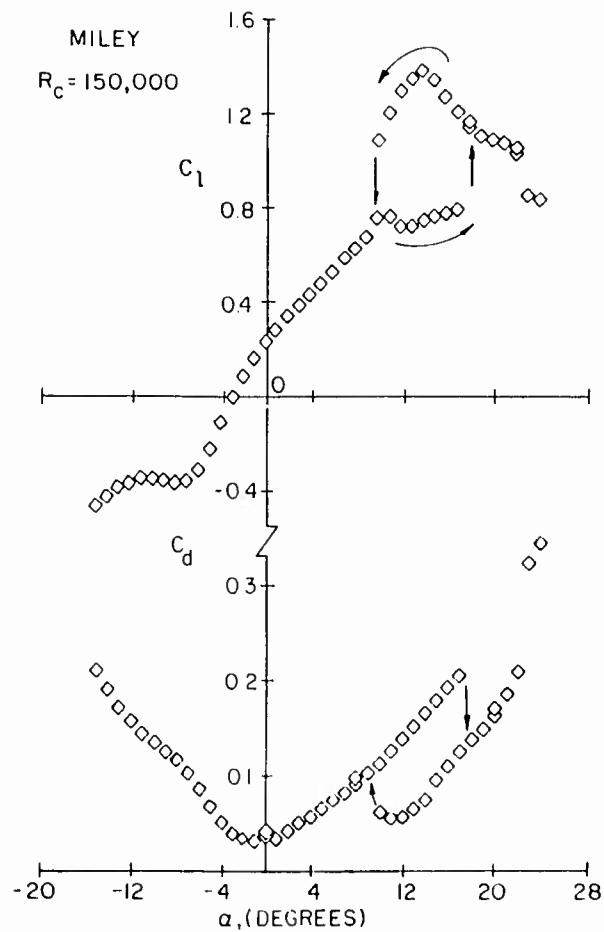


Figure 55. Section Lift and Profile Drag Coefficients versus Angle of Attack at $R_c = 150,000$ for the Smooth Miley Airfoil (Standard Tunnel Configuration).

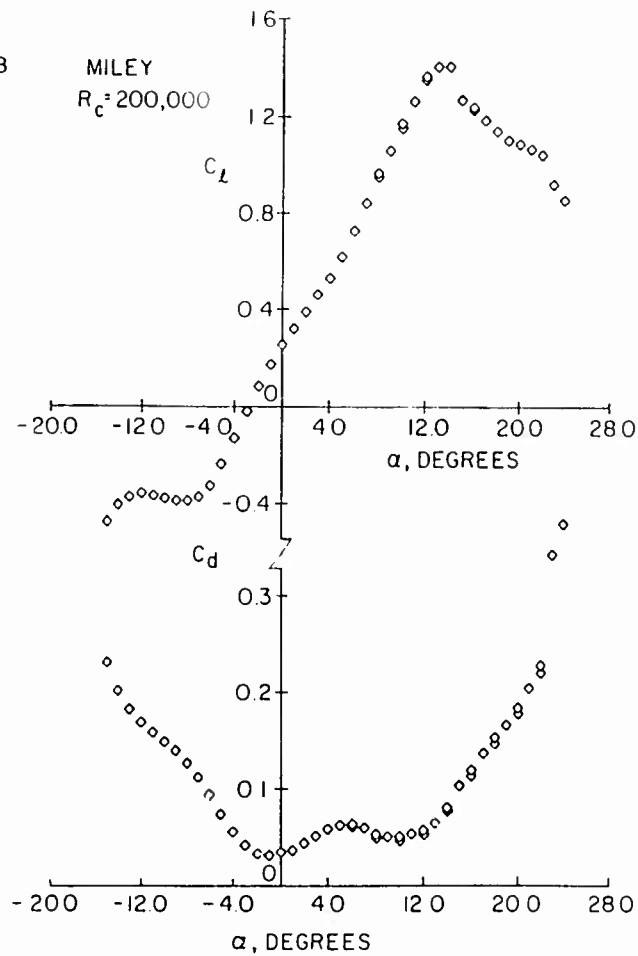
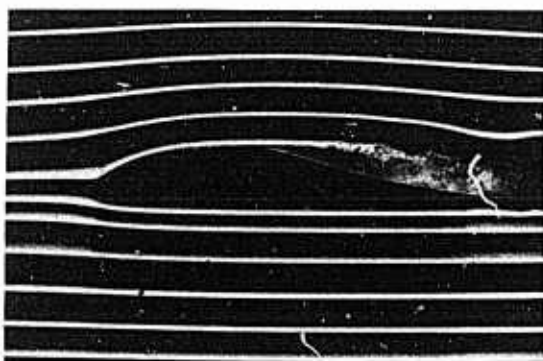
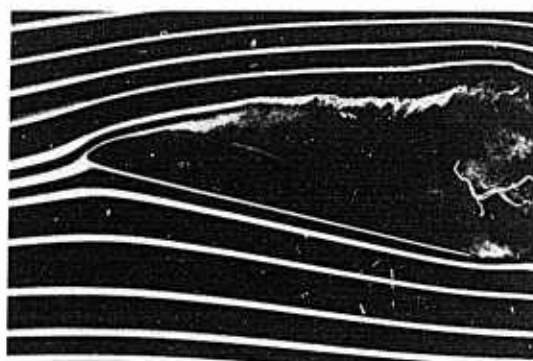


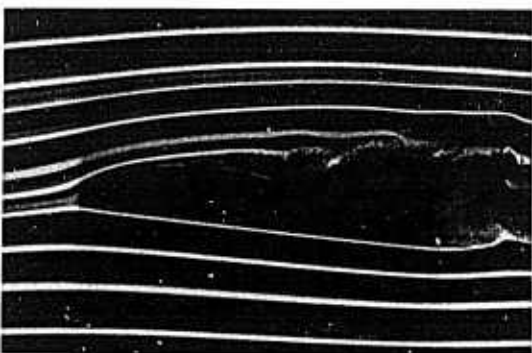
Figure 56. Section Lift and Drag Coefficients versus Angle of Attack for $R_c = 200,000$ for the Smooth Miley Airfoil (Standard Tunnel Configuration).



a) $\alpha = 0^\circ$ increasing



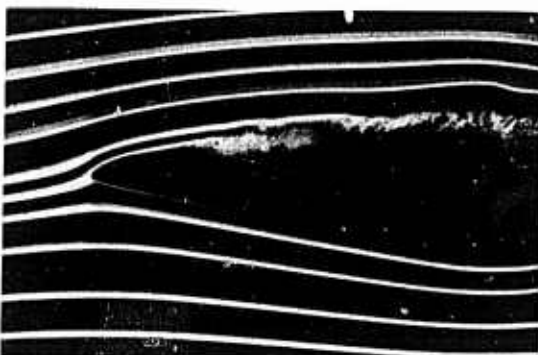
d) $\alpha = 15^\circ$ increasing



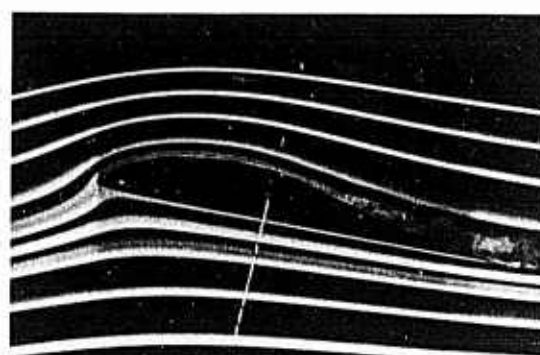
b) $\alpha = 7^\circ$ increasing



e) $\alpha = 19^\circ$ increasing



c) $\alpha = 13^\circ$ increasing



f) $\alpha = 13^\circ$ decreasing

Figure 57. Smoke Visualization Photographs of the Smooth Miley Airfoil at $R_c = 150,000$ (Standard Tunnel Configuration).

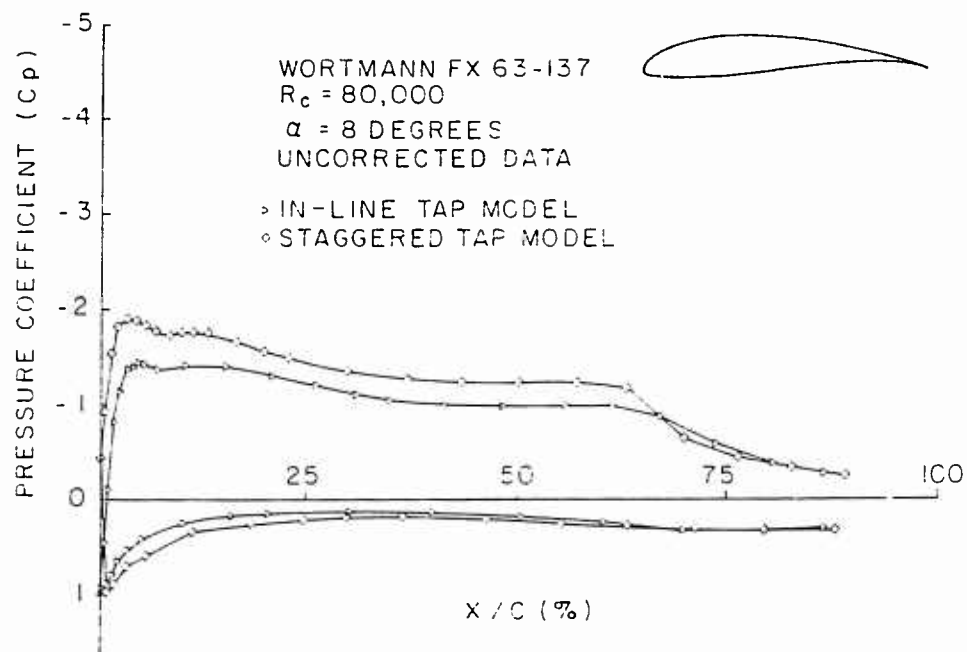


Figure 58. Pressure Coefficient versus Position Along the Chord of the Two-Dimensional Wortmann FX 63-137 Airfoil Models Showing the Influence of Pressure Tap Orientation at $R_c = 80,000$ and $\alpha = 8^\circ$.

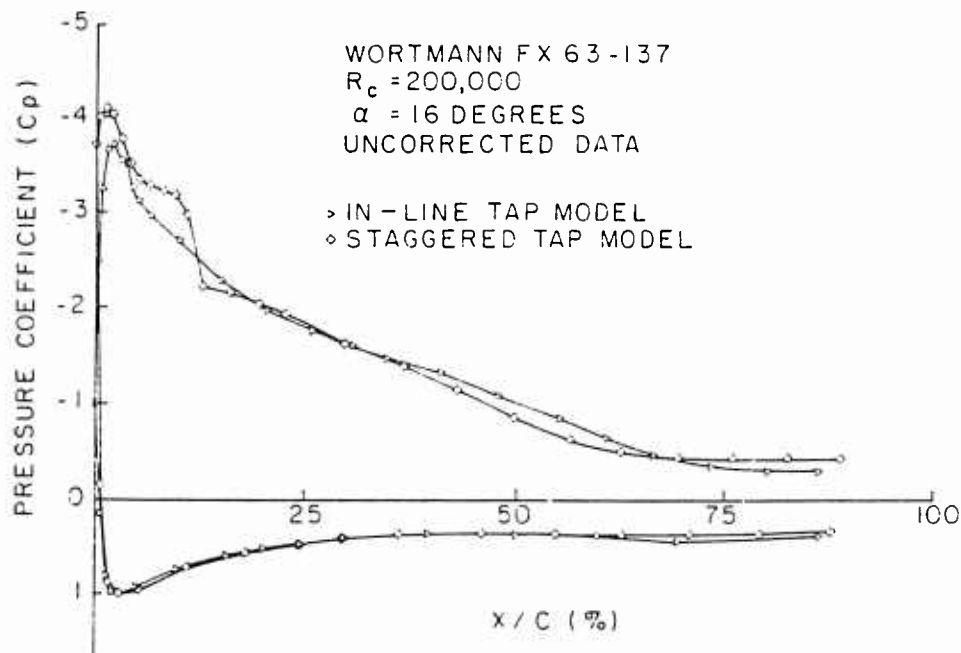


Figure 59. Pressure Coefficient versus Position Along the Chord of the Two-Dimensional Wortmann FX 63-137 Airfoil Models Showing the Influence of Pressure Tap Orientation at $R_c = 200,000$ and $\alpha = 16^\circ$.

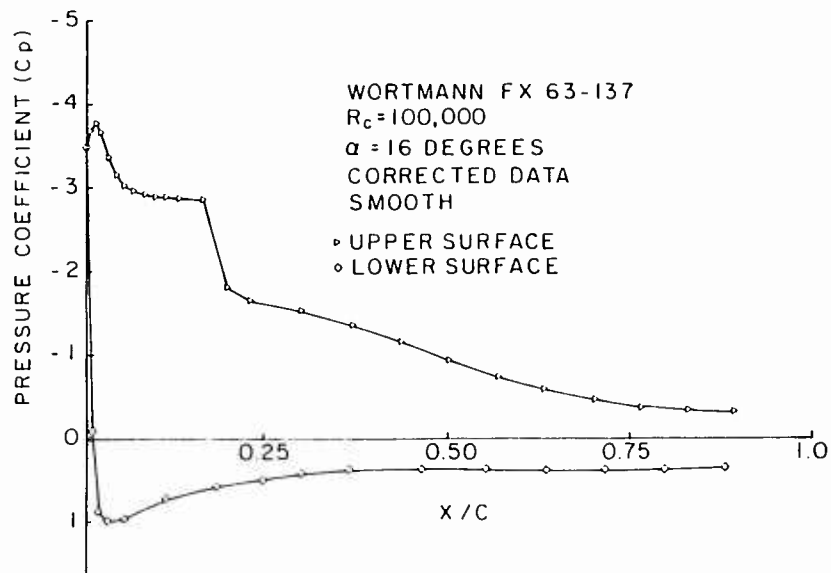


Figure 60. Pressure Coefficient versus Position Along the Chord of the Two-Dimensional Wortmann FX 63-137 Smooth Airfoil Model at $R_c = 100,000$ and $\alpha = 16^\circ$.

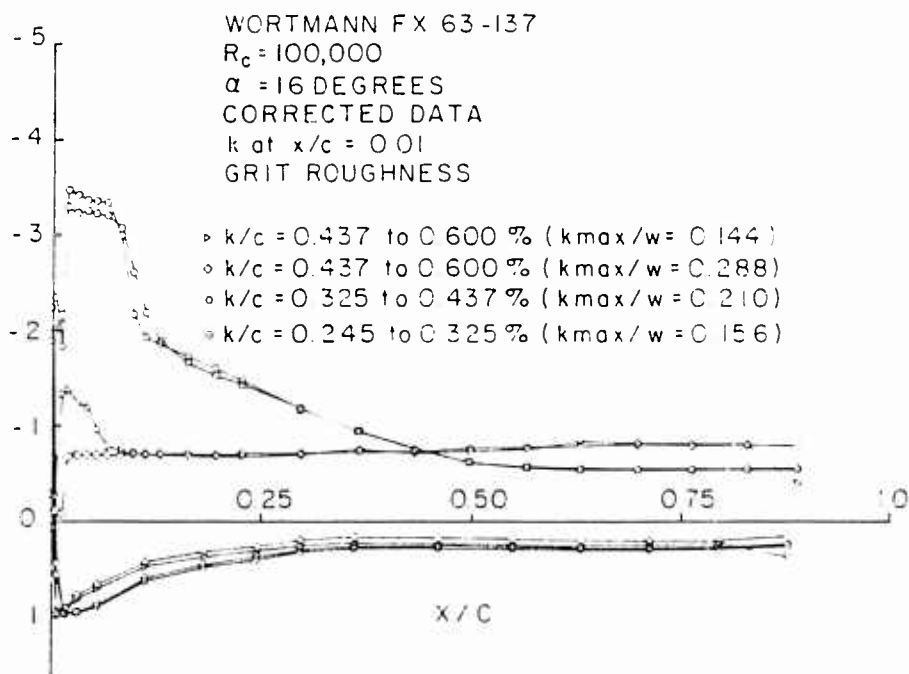


Figure 61. Pressure Coefficient versus Position Along the Chord of the Two-Dimensional Wortmann FX 63-137 Airfoil Showing the Influence of Grit Roughness at $R_c = 100,000$ and $\alpha = 16^\circ$.

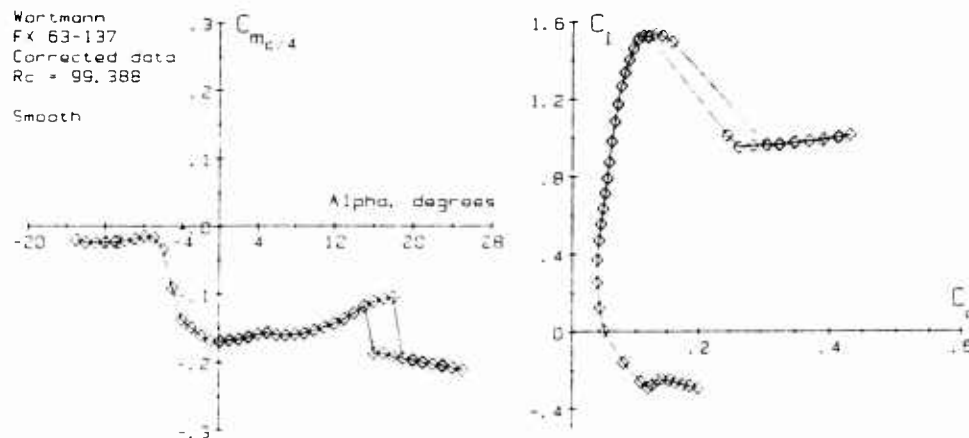


Figure 62. The Quarter-Chord Moment Coefficient versus Angle of Attack and the Lift/Drag Polar for the Smooth Two-Dimensional Wortmann FX 63-137 Airfoil at $R_c = 100,000$.

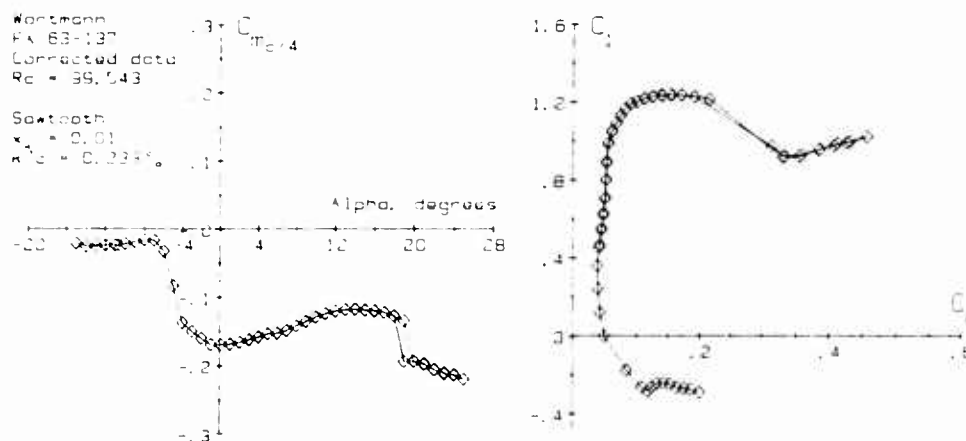
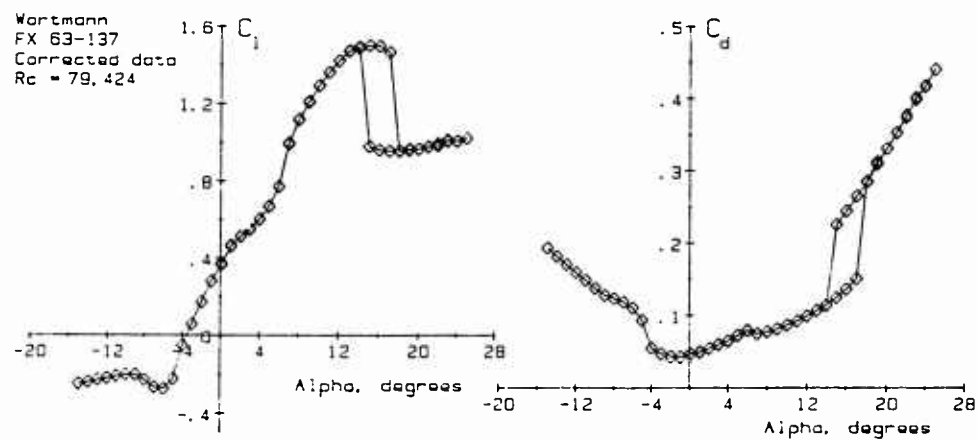
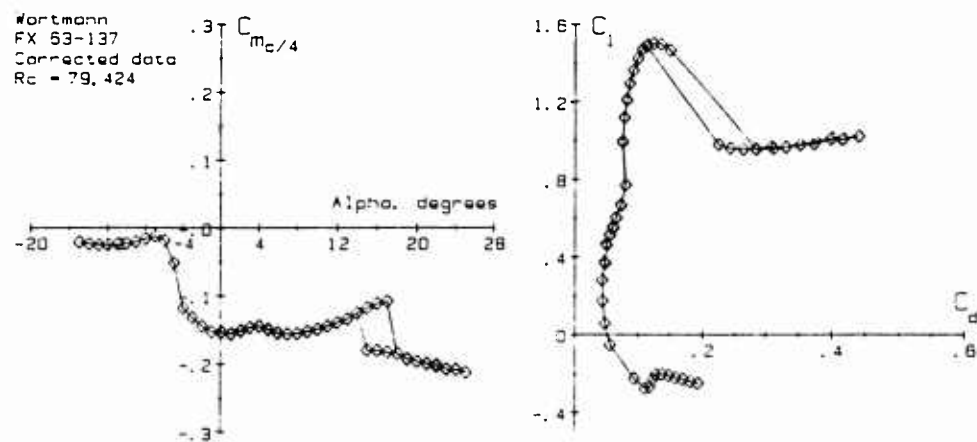


Figure 63. The Quarter-Chord Momentum Coefficient versus Angle of Attack and Lift/Drag Polar for Two-Dimensional Wortmann FX 63-137 Airfoil with Sawtooth Roughness at $R_c = 100,000$.

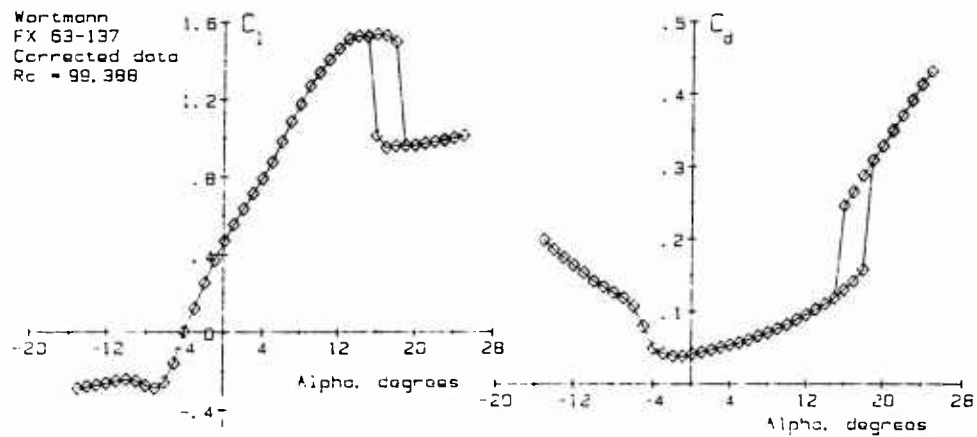


a) Section Lift and Profile Drag Coefficients versus Angle of Attack

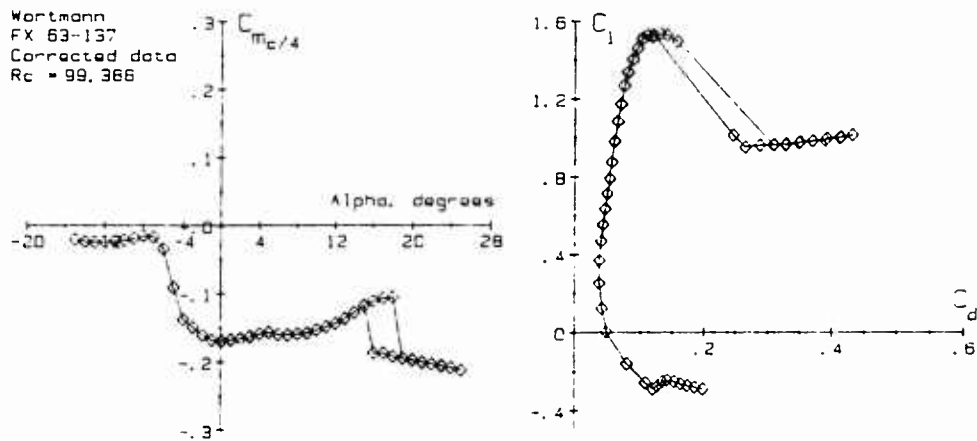


b) Quarter-Chord Moment Coefficient versus Angle of Attack and the Lift/Drag Polar

Figure 64. Two-Dimensional Section Lift, Drag, Quarter-Chord Moment Coefficients versus Angle of Attack and Lift/Drag Polar for the Wortmann FX 63-137 Smooth Airfoil at $R_c = 80,000$.

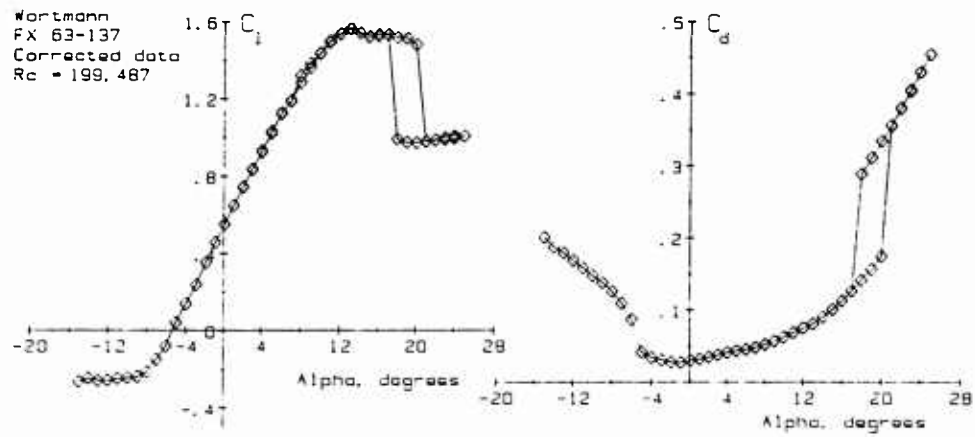


a) Section Lift and Profile Drag Coefficients versus Angle of Attack

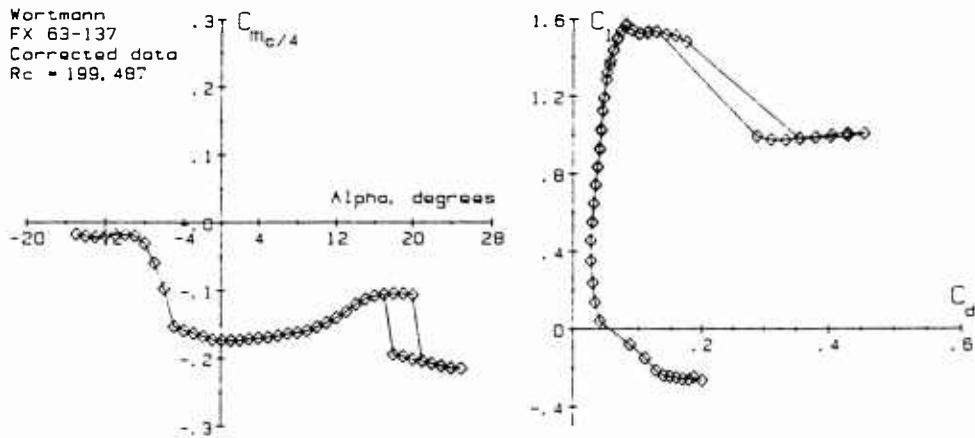


b) Quarter-Chord Moment Coefficient versus Angle of Attack and the Lift/Drag Polar

Figure 65. Two-Dimensional Section Lift, Drag, Quarter-Chord Moment Coefficients versus Angle of Attack and Lift/Drag Polar for the Wortmann FX 63-137 Smooth Airfoil at $R_c = 100,000$.

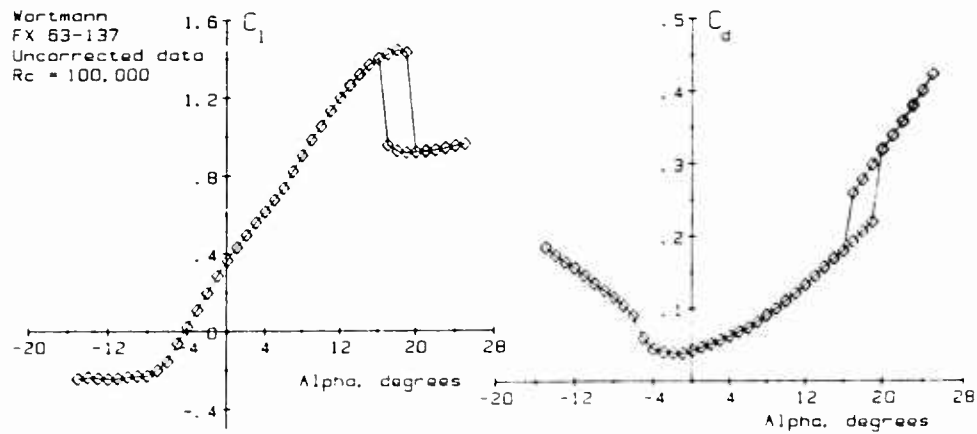


a) Section Lift and Profile Drag Coefficients versus Angle of Attack

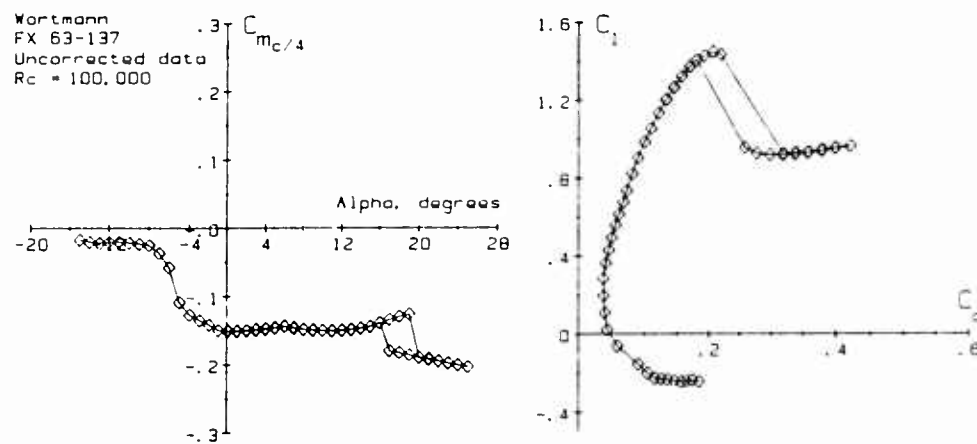


b) Quarter-Chord Moment Coefficient versus Angle of Attack and the Lift/Drag Polar

Figure 66. Two-Dimensional Section Lift, Drag, Quarter-Chord Moment Coefficients versus Angle of Attack and Lift/Drag Polar for the Wortmann FX 63-137 Smooth Airfoil at $R_c = 200,000$.



a) Lift and Profile Drag Coefficients versus Angle of Attack



b) Quarter-Chord Moment Coefficient versus Angle of Attack and the Lift/Drag Polar

Figure 67. Rectangular Finite Wing Lift, Drag, Quarter-Chord Moment Coefficients versus Angle of Attack and Lift/Drag Polar for Semi-Span Aspect Ratio of 2.7 and $R_c = 100,000$.

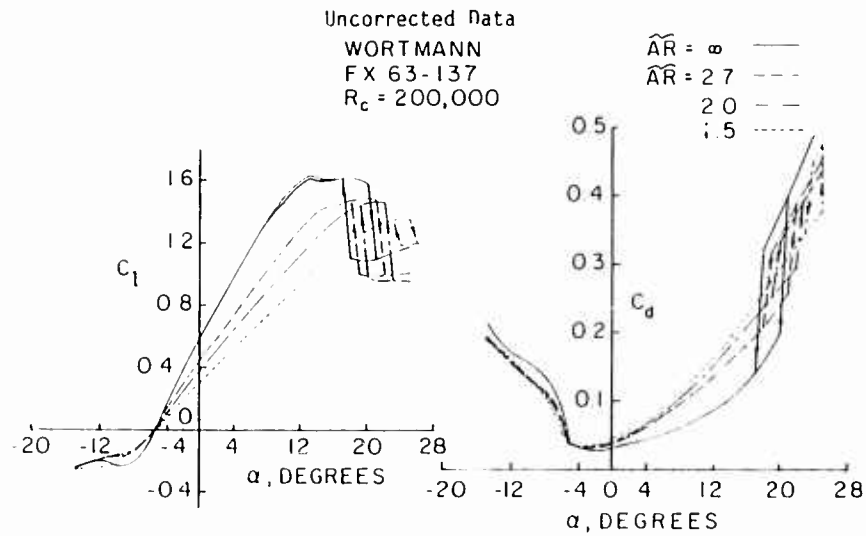


Figure 68. The Effect of Semi-Span Aspect Ratio on the Rectangular Wing Lift and Drag Coefficients versus Angle of Attack for $R_c = 200,000$.

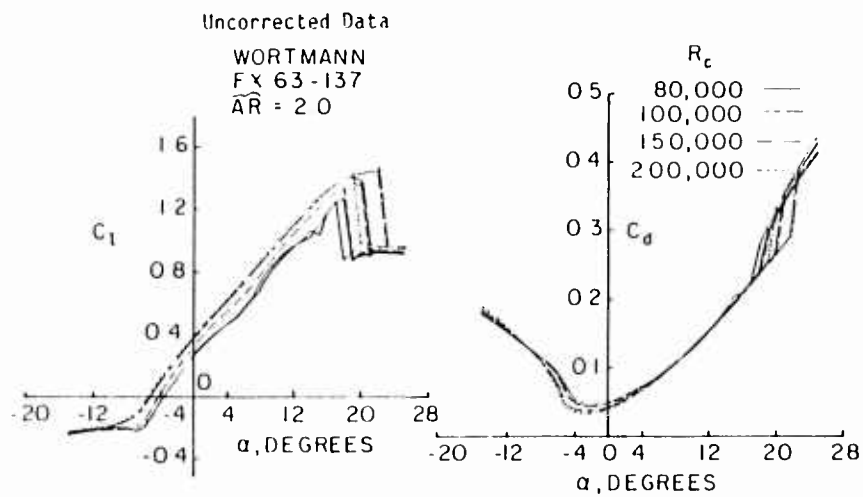


Figure 69. The Effect of Chord Reynolds Number on Lift and Drag Coefficients versus Angle of Attack for a Rectangular Wing with Semi-Span Aspect Ratio of 2.0.

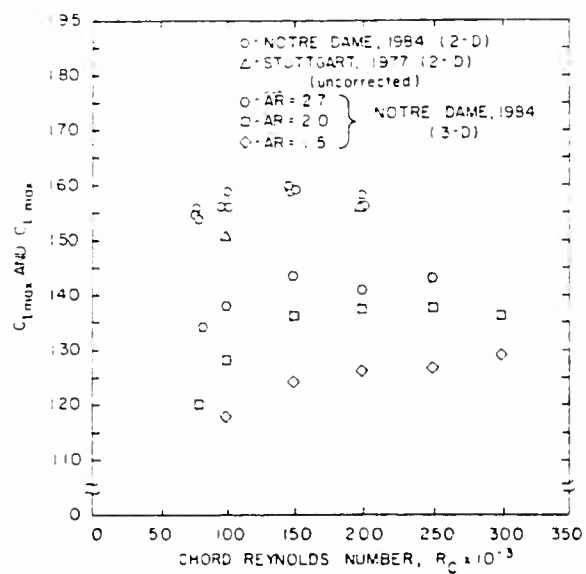


Figure 70. Maximum Lift Coefficient versus Chord Reynolds Number for the FX 63-137 Airfoil and Rectangular Wing.

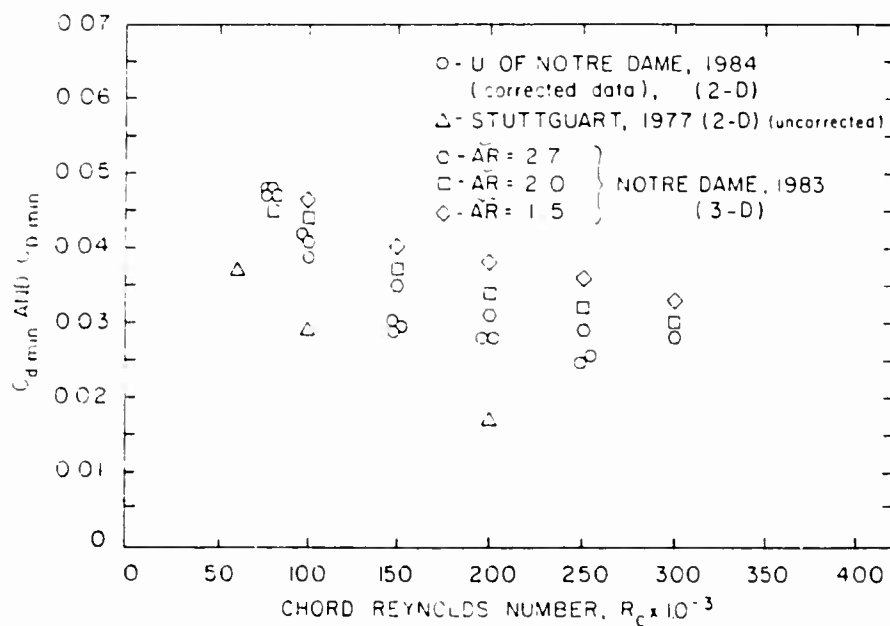


Figure 71. Minimum Drag Coefficient versus Chord Reynolds Number for the FX 63-137 Airfoil and Rectangular Wing.

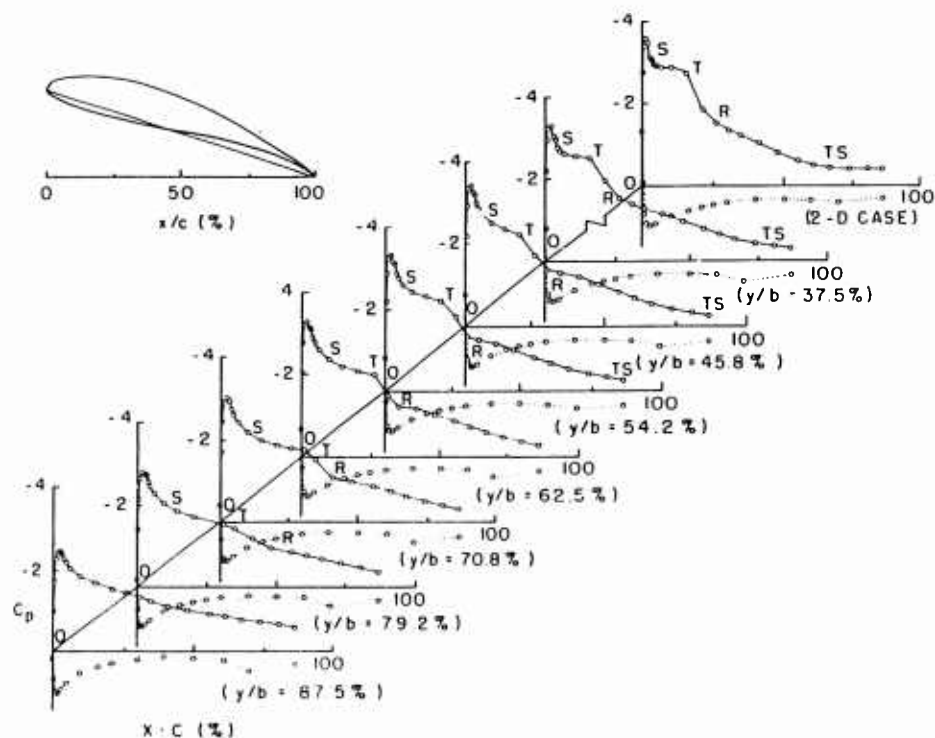


Figure 72. Pressure Distributions at Seven Positions (y) Along Semi-Span (b) and the Two-Dimensional Pressure Distributions for $R_C = 80,000$, $AR = 2.0$ and $\alpha = 18^\circ$.

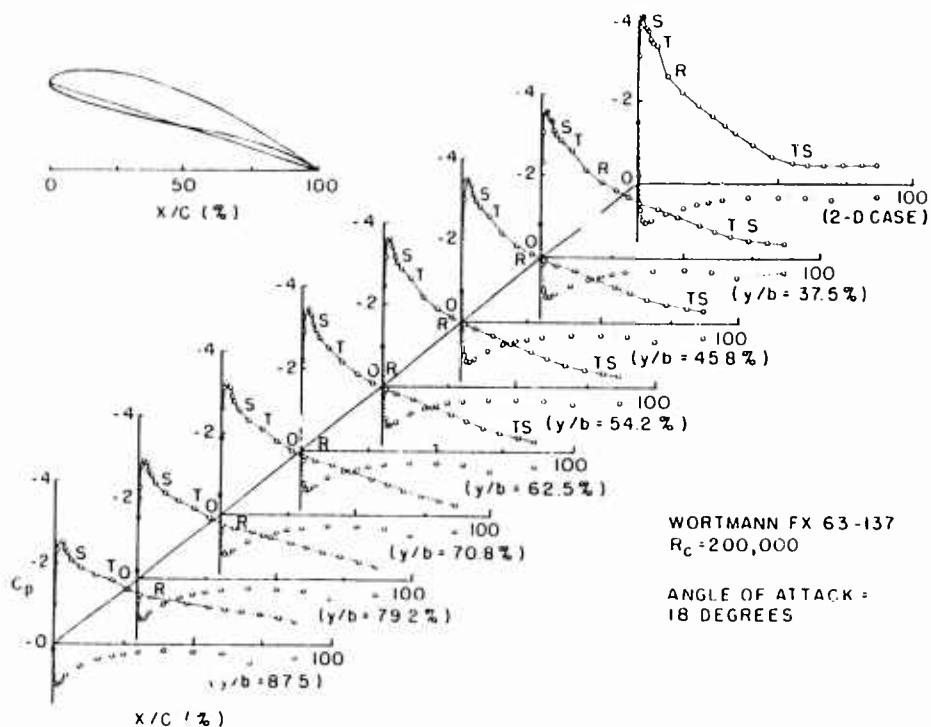


Figure 73. Pressure Distributions at Seven Positions (y) Along Semi-Span (b) and the Two-Dimensional Pressure Distributions for $R_C = 200,000$, $AR = 2.0$ and $\alpha = 18^\circ$.

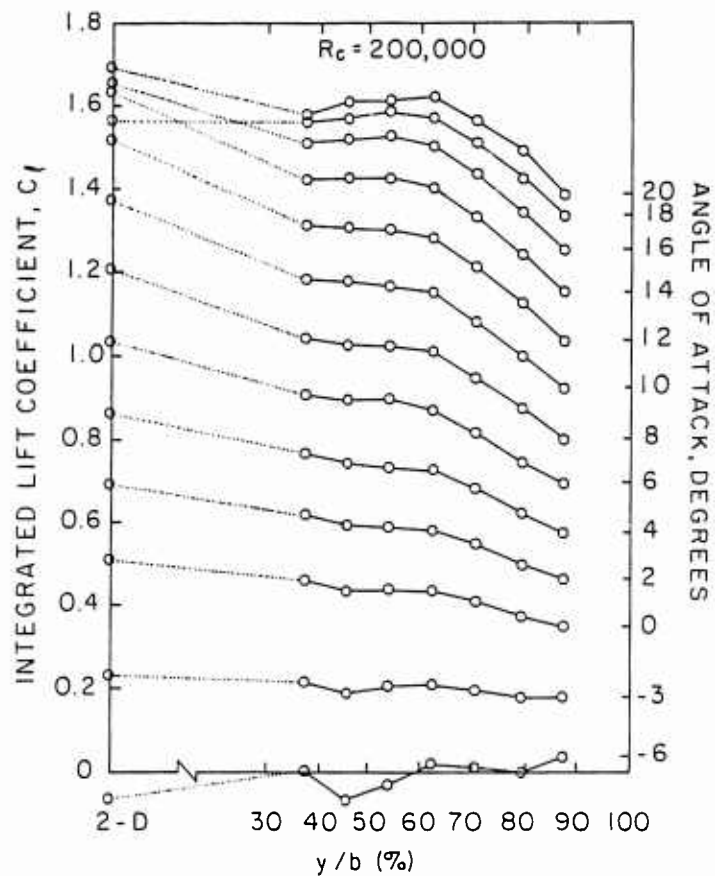


Figure 74. Finite Wing Lift Coefficient versus Non-Dimensional Distance (y) Along Semi-Span (b) in Percent for Various Angles of Attack for $R_c = 200,000$ and $AR = 2.0$.

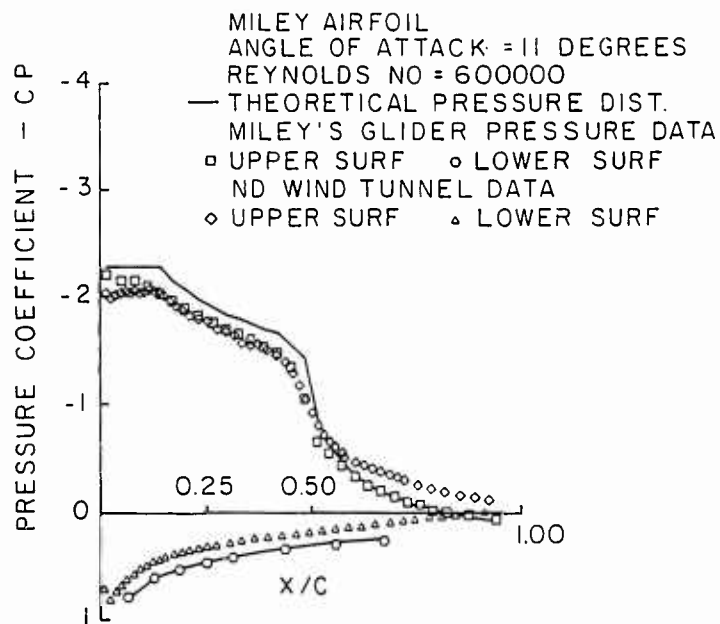


Figure 75. Comparison of Theoretical Design and Experimental Pressure Distribution for the Miley Airfoil at $\alpha = 11^\circ$ and $R_c = 600,000$.

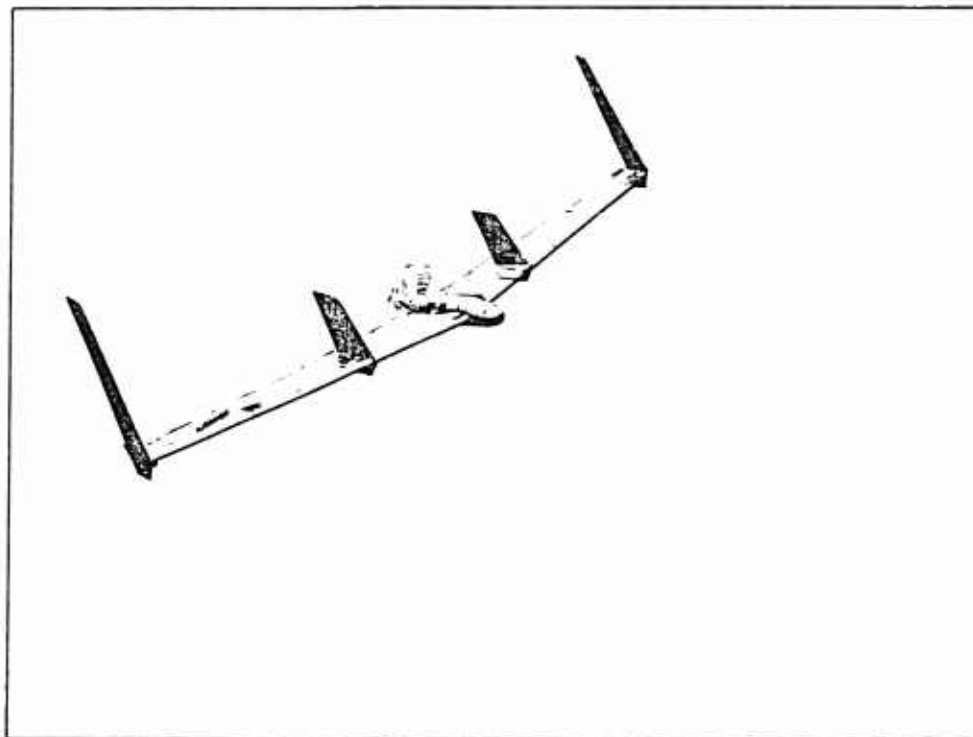


Figure 76. An Example of a Solar High Altitude Powered Platform in the Daytime (Wing tips fold down to increase aspect ratio at night) Designed by the Lockheed Missiles and Space Company (Reference 162).

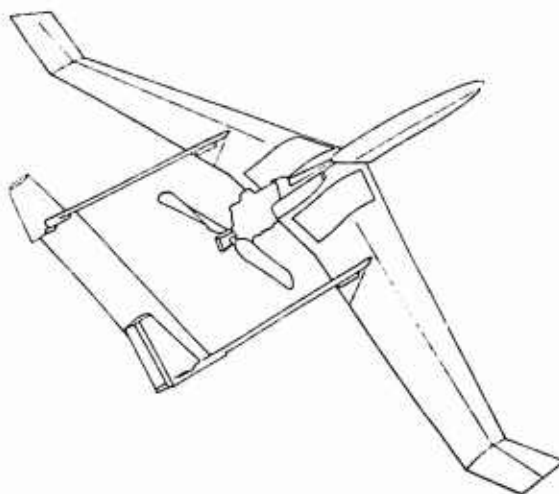
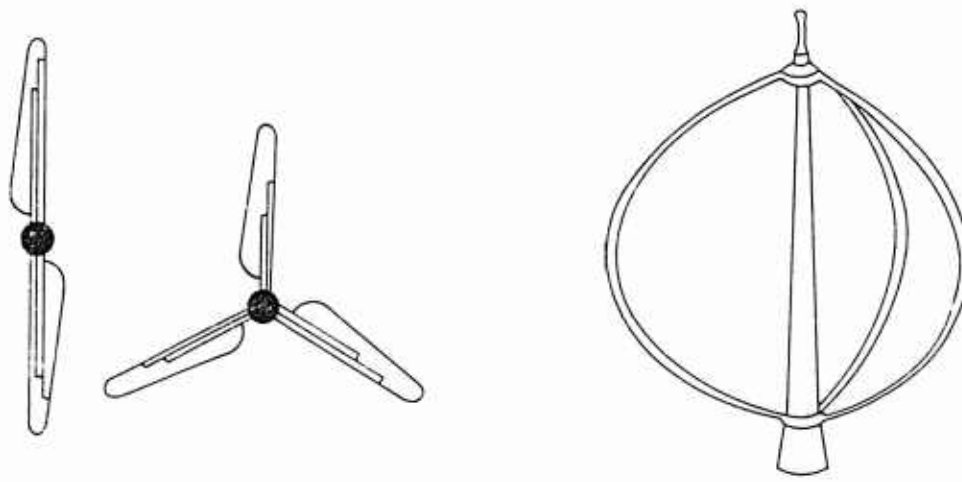


Figure 77. Mini-Sniffer RPV (Reference 5).



a) Horizontal Axis Propeller-Type

b) Vertical Axis Darrieus-Type

Figure 78. Wind Turbine Configurations

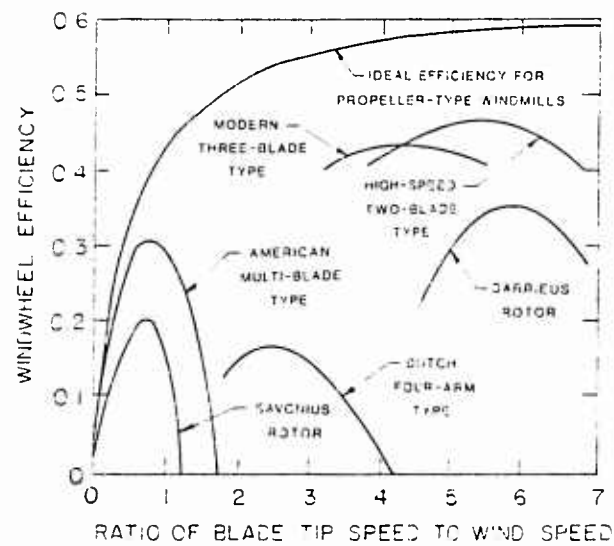


Figure 79. Ratio of Blade Tip Speed to Wind Speed for Various Wind Turbines.

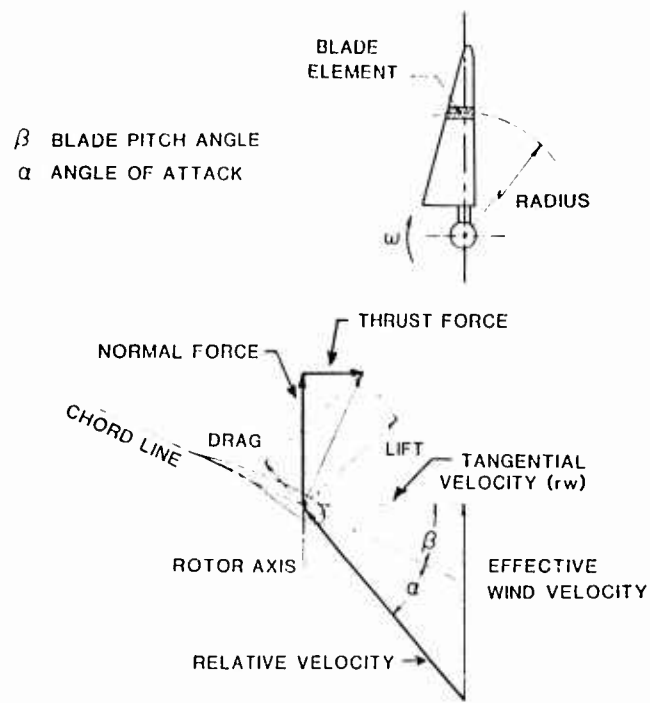


Figure 80. Horizontal Axis Wind Turbine (HAWT) Blade Element Velocities and Forces.

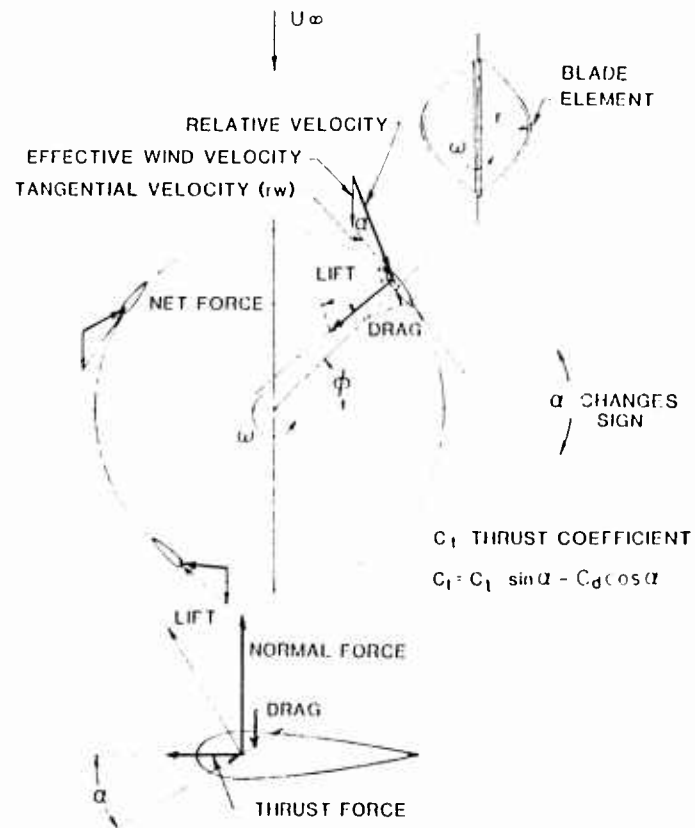


Figure 81. Vertical Axis Wind Turbine (VAWT) Blade Element Velocities and Force.

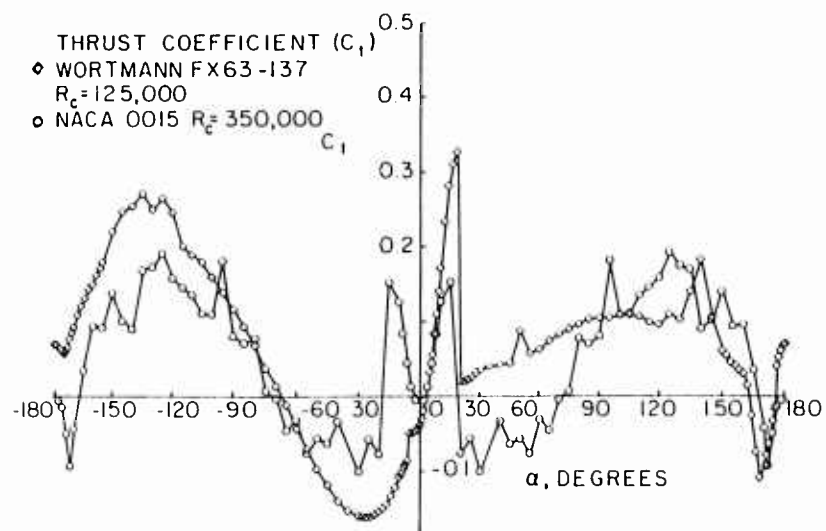


Figure 82. Thrust Coefficient versus Angle of Attack for the Wortmann FX 63-137 Airfoil at $R_c = 125,000$ and the NACA 0015 Airfoil at $R_c = 350,000$.

REPORT DOCUMENTATION PAGE			
1. Recipient's Reference	2. Originator's Reference	3. Further Reference	4. Security Classification of Document
	AGARD-AG-288	ISBN 92-835-1486-6	UNCLASSIFIED
5. Originator	Advisory Group for Aerospace Research and Development North Atlantic Treaty Organization 7 rue Ancelle, 92200 Neuilly sur Seine, France		
6. Title	LOW REYNOLDS NUMBER VEHICLES		
7. Presented at			
8. Author(s)/Editor(s)			9. Date
T.J.Mueller — Edited by E.Reshotko			February 1985
10. Author's/Editor's Address			11. Pages
See Flyleaf			74
12. Distribution Statement	This document is distributed in accordance with AGARD policies and regulations, which are outlined on the Outside Back Covers of all AGARD publications.		
13. Keywords/Descriptors			
<div> Reynolds number Airfoils </div> <div> Aerodynamic configurations Aerodynamics </div>			
14. Abstract			
<p>Recent interest in the subject of low Reynolds number configuration has centered on the design and evaluation of efficient airfoil sections at chord Reynolds numbers from about 100,000 to 1 m. These configurations include remotely-piloted vehicles operating at high altitudes, sailplanes, ultra-light man-carrying/man-powered aircraft, wind turbines and propellers.</p> <p>Serious problems still exist in respect of boundary layer separations and transition below $R_c = 500,000$. Current design and analysis methods need improved criteria for laminar separation. Improved mathematical models for these complex phenomena require more experimental studies. For various reasons definitive experiments are difficult. The results of many experimental studies are presented to illustrate the type of difficulties encountered. The publication concludes with recommendations for future research. It also contains a very full Reference List of documentation on the subject.</p> <p>This AGARDograph has been produced at the request of the Fluid Dynamics Panel of AGARD.</p>			

<p>Serious problems still exist in respect of boundary layer separations and transition below $R_c = 500,000$. Current design and analysis methods need improved criteria for laminar separation, transition and turbulent separation. Improved mathematical models for these complex phenomena require more experimental studies. For various reasons definitive experiments are difficult. The results of many experimental studies are presented to illustrate the type of difficulties encountered. The publication concludes with recommendations for future research. It also contains a very full Reference List of documentation on the subject.</p> <p>This AGARDograph has been produced at the request of the Fluid Dynamics Panel of AGARD.</p> <p>ISBN 92-835-1486-6</p>	<p>Serious problems still exist in respect of boundary layer separations and transition below $R_c = 500,000$. Current design and analysis methods need improved criteria for laminar separation, transition and turbulent separation. Improved mathematical models for these complex phenomena require more experimental studies. For various reasons definitive experiments are difficult. The results of many experimental studies are presented to illustrate the type of difficulties encountered. The publication concludes with recommendations for future research. It also contains a very full Reference List of documentation on the subject.</p> <p>This AGARDograph has been produced at the request of the Fluid Dynamics Panel of AGARD.</p> <p>ISBN 92-835-1486-6</p>
<p>Serious problems still exist in respect of boundary layer separations and transition below $R_c = 500,000$. Current design and analysis methods need improved criteria for laminar separation, transition and turbulent separation. Improved mathematical models for these complex phenomena require more experimental studies. For various reasons definitive experiments are difficult. The results of many experimental studies are presented to illustrate the type of difficulties encountered. The publication concludes with recommendations for future research. It also contains a very full Reference List of documentation on the subject.</p> <p>This AGARDograph has been produced at the request of the Fluid Dynamics Panel of AGARD.</p> <p>ISBN 92-835-1486-6</p>	<p>Serious problems still exist in respect of boundary layer separations and transition below $R_c = 500,000$. Current design and analysis methods need improved criteria for laminar separation, transition and turbulent separation. Improved mathematical models for these complex phenomena require more experimental studies. For various reasons definitive experiments are difficult. The results of many experimental studies are presented to illustrate the type of difficulties encountered. The publication concludes with recommendations for future research. It also contains a very full Reference List of documentation on the subject.</p> <p>This AGARDograph has been produced at the request of the Fluid Dynamics Panel of AGARD.</p> <p>ISBN 92-835-1486-6</p>